

# **Development of a SiPM camera for detection and measurement of fluorescence emission from extensive air-showers generated by ultra high energy cosmic rays**

Zur Erlangung des akademischen Grades eines

**Doktors der Naturwissenschaften**

an der KIT - Fakultät für Physik

genehmigte

**Dissertation**

von

**MSc. William Painter**

aus Spokane, WA, USA

Tag der mündlichen Prüfung: 17 May 2019

Referent: Prof. Dr. Dr. h.c. Johannes Blümer

Korreferent: Prof. Dr. Ivan Peric

Betreuer: Dr. Andreas Haungs

May 21, 2019



This document is licensed under a Creative Commons Attribution 4.0 International License (CC BY 4.0): <https://creativecommons.org/licenses/by/4.0/deed.en>



---

# Abstract

## **Development of SiPM camera for detection and measurement of fluorescence emission from extensive air-showers generated by ultra high energy cosmic rays**

This thesis undertakes the construction and characterization of SiECA, the Silicon photomultiplier Elementary Cell Add-on camera for use in the detection of the fluorescence signature of extensive air showers generated by ultra high energy cosmic rays in Earth's atmosphere. Specifically, the correction of non-uniformity and assessment of full system sensitivity are most directly analyzed. This work is predominantly technical and hardware oriented with the physics motivation of operation of SiPM as part of the orbital cosmic ray observatory in the Extreme Universe Space Observatory (EUSO) or Probe Of Extreme Multi-Messenger Astrophysics (POEMMA) telescopes.

SiECA is a proof of capability for current hardware, sensor, ASIC and support electronics as well as a prototype for future devices. Assessment of currently available device capabilities provides insight into the necessary technological advancements required for successful development of larger scale low light sensitive, high speed detection systems in the future.

Within this thesis the design process, sensor characterization, camera construction, laboratory testing and calibration and deployment opportunities are detailed with review of the successful and problematic events throughout. The development of SiECA from concept to first deployment on-board the EUSO-SPB1 balloon borne telescope was a mere 18 months. Many improvements remain to be made, however, substantial understanding of the SiPM and ASIC characteristics have been gained in this process which I intend to detail in the following pages.



---

# Zusammenfassung

## **Entwicklung einer SiPM-Kamera zur Erkennung und Messung der Fluoreszenz-Emission von durch ultra-hochenergetische kosmische Strahlung ausgelöste ausgedehnte Luftschauer**

Diese Arbeit behandelt die Entwicklung, Charakterisierung und Kalibrierung von SiECA, der "Silicon photomultiplier Elementary Cell Add-on" Fluoreszenzkamera. Diese Kamera wurde entwickelt für einen Einsatz zur Erkennung der Fluoreszenzsignatur von ausgedehnten Luftschauern, welche bei Kollisionen von ultrahochenergetischer kosmischer Strahlung mit der Erdatmosphäre entstehen.

Insbesondere die Korrekturmechanismen um eine uniforme Photodetektorfläche zu erreichen und die Bestimmung der absoluten Photosensitivität wurden detailliert analysiert. Diese Arbeit ist überwiegend experimentell-technisch orientiert mit der astrophysikalischen Motivation, den Betrieb von SiPM (Silicon Photomultiplier) als Teil von geplanten Weltraumteleskopen für kosmische Strahlung, zum Beispiel das Extreme Universe Space Observatory (EUSO) oder das Probe Of Extreme Multi-Messenger Astrophysics (POEMMA), zu untersuchen.

SiECA ist ein Machbarkeitsnachweis für aktuell verfügbare Komponenten, wie Sensoren, ASICs und Unterstützungselektroniken und damit ein Prototyp für zukünftige Fluoreszenzkameras. Die Bewertung der derzeit verfügbaren Komponenten gibt einen Einblick in die notwendigen technologischen Fortschritte, die für die erfolgreiche Entwicklung größerer, auf kleinste Lichtmengen sensitiver Kamerasysteme mit schneller Auslese in der Zukunft erforderlich sind. In dieser Arbeit werden der Entwicklungsprozess, die Sensorcharakterisierung, der Kamerabau, die Laborprüfung sowie die Möglichkeiten der Kalibrierung und die Einsätze der Kamera detailliert beschrieben. Entwicklung einer SiPM-Kamera zur Erkennung und Messung der Fluoreszenz-Emission von durch ultra-hochenergetische kosmische Strahlung ausgelöste ausgedehnte Luftschauer. Die Entwicklung von SiECA vom Konzept bis zum ersten Einsatz an Bord des Ballontelekops EUSO-SPB1 dauerte nur 18 Monate. Viele Verbesserungen sind noch erforderlich, dennoch wurden in dieser Arbeit wesentliche Erkenntnisse über die Eigenschaften aktueller SiPMs und ASICs gewonnen, die in folgender Arbeit beschrieben werden.



---

# Acronyms

This is a list of acronyms used within this work sorted alphabetically according to the short version.

<b>CMB</b>	Cosmic Microwave Background . . . . .	13
<b>EAS</b>	Extensive Air Shower	
<b>GZK</b>	Greisen–Zatsepin–Kuzmin . . . . .	13
<b>UHECR</b>	Ultra-High Energy Cosmic Ray . . . . .	3
<b>PCB</b>	Printed Circuit Board . . . . .	6
<b>ASIC</b>	Application Specific Integrated Circuit . . . . .	14
<b>PMT</b>	Photo-Multiplier Tube . . . . .	4
<b>SiPM</b>	Silicon Photo-Multiplier . . . . .	3
<b>MPPC</b>	Hamamatsu Multi-Pixel Photon Counter . . . . .	5
<b>EC</b>	Elementary Cell: 4 MAPMTs potted together . . . . .	15
<b>PDM</b>	Photo Detection Module: 9 ECs integrated . . . . .	15
<b>CCB</b>	Cluster Control Board, manages 8 PDMs in EUSO architecture . . . . .	15
<b>DAC</b>	Digital to Analog Converter . . . . .	23
<b>ADC</b>	Analog to Digital Converter . . . . .	35
<b>FPGA</b>	Field Programmable Gate Array . . . . .	19
<b>USB</b>	Universal Serial Bus . . . . .	33
<b>LVDS</b>	Low Voltage Differential Signal . . . . .	33
<b>LVPS</b>	Low Voltage Power Supply . . . . .	16
<b>Si-EC</b>	Sensor PCB of SiECA . . . . .	33
<b>DAQ</b>	Data Acquisition main board of SiECA . . . . .	33
<b>Mezz</b>	Mezzanine auxiliary ASIC board of SiECA . . . . .	33
<b>BG3</b>	Schott BG3 UV-band pass optical filter glass . . . . .	21
<b>IC</b>	Integrated Circuit . . . . .	62
<b>SMD</b>	Surface Mount Device, electronic . . . . .	6
<b>CNC</b>	Computer Numerical Control . . . . .	37
<b>GAPD</b>	Geiger mode Avalanche Photo Diode . . . . .	3
<b>FIFO</b>	First In, First Out operation of the USB interface . . . . .	42
<b>D-sub9</b>	D-sub-miniature electrical connectors with 9 pins . . . . .	42

<b>VGA</b>	Video Graphics Array, 15 pin 'D-sub' style used for LVDS inputs . . . . .	42
<b>TTL</b>	Transistor-Transistor Logic . . . . .	42
<b>PPS</b>	Pulse per second, GPS generated synchronization pulse . . . . .	42
<b>EEPROM</b>	Electrically Erasable Programmable Read-Only Memory . . . . .	43
<b>CPU</b>	Central Processing Unit, computer within EUSO-SPB1 Data Processor . . .	15
<b>SPOCK</b>	Single PhOton Calibration stand at KIT . . . . .	23
<b>3P-GPS-053-SL</b>	3 port, 13.46 cm diameter, 6.35 cm entrance, two 2.54 cm outputs . . . . .	23
<b>LED</b>	Light Emitting Diode . . . . .	23
<b>PD</b>	NIST calibrated light intensity measuring Photodiode . . . . .	17
<b>PD-A</b>	Photodiode on SPOCK integrating sphere for light intensity monitoring .	23
<b>PD-B</b>	Photodiode at collimator for measuring Collimator Ratio . . . . .	28
<b>QADC</b>	Charge Analog to Digital Converter, CAEN v965 . . . . .	25
<b>GAPD</b>	Geiger Avalanche Photo Diode . . . . .	3
<b>APD</b>	Avalanche Photo Diode . . . . .	3
<b>PMMA</b>	Poly(methyl methacrylate) or acrylic glass . . . . .	15
<b>DC-DC</b>	Direct Current to Direct Current voltage converter . . . . .	62
<b>DP</b>	Data Processor, Data and telemetry computer on EUSO-SPB1 . . . . .	62
<b>SLT</b>	Second level trigger: pattern recognition trigger in HEAT . . . . .	65
<b>UPS</b>	Uninterruptible Power Supply . . . . .	65
<b>TSV</b>	Through Silicon Via, via through silicon for anode connection . . . . .	6
<b>BGA</b>	Ball-Grid Array, 2D grid of contacts instead of edge only packages . . . . .	68
<b>LVC MOS</b>	Low voltage complementary metal oxide semiconductor digital logic . . .	62
<b>S13361</b>	Hamamatsu S13361-3050AS-08 64 channel MPPC . . . . .	6
<b>S13361-NS</b>	Hamamatsu S13361-3050NS-08 64 channel MPPC . . . . .	68
<b>MAPMT</b>	Hamamatsu Multi-Anode PhotoMultiplier	
<b>R11265</b>	Hamamatsu R11265-113-M64 MOD2 64 channel MAPMT . . . . .	6
<b>ST4-40</b>	Samtec ST4-40-1.00-L-D-P-TR array connector . . . . .	68
<b>SS4-40</b>	Samtec SS4-40-3.00-L-D array receptacle . . . . .	35
<b>ERF8</b>	Samtec ERF8-060-07.0-L-DV-TR . . . . .	35
<b>ERM8</b>	Samtec ERM8-060-05.0-L-DV-TR . . . . .	35
<b>QRM8</b>	Samtec QRM8-078-01-L-RA-GP . . . . .	33
<b>QRF8</b>	Samtec QRF8-078-05.0-L-D-A-GP . . . . .	33
<b>Spartan6</b>	Xilinx Spartan-6 XC6SLX100-2FGG676I . . . . .	19
<b>C11204-02</b>	Hamamatsu SMD high voltage MPPC bias generator . . . . .	19
<b>C12332-01</b>	Hamamatsu MPPC single channel evaluation board	
<b>EPO-301</b>	EPO-TEK 301-2 optical 2 part epoxy resin . . . . .	38
<b>Citiroc</b>	32 channel SiPM ASIC developed by Omega/LAL . . . . .	19
<b>FT232H</b>	FTDI single USB 2.0 chip used in FIFO mode with event buffer . . . . .	42
<b>FO-M93</b>	Shielded optical fiber Thorlabs M93L01, 300 to 1200 nm . . . . .	29
<b>WS-2012</b>	Teledyne Lecroy WaveStation 2012 arbitrary waveform generator . . . . .	29
<b>LDD</b>	CERN-NP N4168 Light Diode Driver . . . . .	29
<b>Spaciroc3</b>	64 channel MAPMT ASIC developed by Omega/LAL . . . . .	15
<b>DRS4</b>	Switched Capacitor Array ASIC, 6 GSPS max, Paul Scherrer Institut . . . .	44
<b>CLF</b>	Central Laser Facility . . . . .	61
<b>FD</b>	Fluorescence Detector, telescope for fluorescent EAS emission . . . . .	11

<b>HEAT</b>	High Elevation Auger Telescopes .....	26
<b>ISS</b>	International Space Station .....	13
<b>SiECA</b>	Silicon Elementary Cell Add-on .....	17
<b>EUSO</b>	Extreme Universe Space Observatory .....	13
<b>EUSO-SPB1</b>	Payload of NASA SPB-2017 mission. Launched 5.4.17 .....	16
<b>EUSO-SPB2</b>	Planned POEMMA prototype for future NASA SPB mission.....	17
<b>EUSO-TA</b>	EUSO prototype telescope at Telescope Array .....	63
<b>EUSO-Balloon</b>	EUSO prototype flown 25.8.2014 from Timmins, Ontario .....	16
<b>POEMMA</b>	Probe Of Extreme Multi-Messenger Astrophysics .....	14
<b>MAGIC</b>	Major Atmospheric Gamma Imaging Cerenkov Telescopes .....	18
<b>HESS</b>	High Energy Stereoscopic System .....	18
<b>VERITAS</b>	Very Energetic Radiation Imaging Telescope Array System .....	18
<b>FoV</b>	Field of View angle or angles defining area observed by telescope .....	15
<b>GPS</b>	Global Positioning System .....	17
<b>UV</b>	Ultra Violet light, wavelength 10 to 400 nm .....	7
<b>ColRat</b>	Collimator Ratio, emitted intensity over incident intensity .....	23
<b>ASL</b>	Above Sea Level	
<b>NASA</b>	National Aeronautics and Space Administration .....	16
<b>PE</b>	Photo-Electron, photon to charge ratio in a photomultiplier .....	4
<b>GTU</b>	Gate Time Unit. EUSO measurement time binning .....	14
<b>PDE</b>	Photon Detection Efficiency, a product of quantum efficiency and fill factor and avalanche probability .....	5



---

# Contents

<b>1</b>	<b>Historic Background</b>	<b>3</b>
1.1	Development of Silicon Detectors . . . . .	3
1.1.1	Silicon Particle Detectors . . . . .	3
1.1.2	Geiger-Avalanche Photodiodes . . . . .	4
1.1.3	Silicon Photomultipliers . . . . .	5
1.1.4	Comparing SiPMs and PMTs . . . . .	6
1.2	Non-Terrestrial Radiation . . . . .	7
1.2.1	Historic Milestones in Cosmic Ray Physics . . . . .	7
1.2.2	Cerenkov Light Emission . . . . .	10
1.2.3	Fluorescence Light Emission . . . . .	11
1.3	What Cosmic Rays have yet to tell us . . . . .	12
1.3.1	Extending detection to Space . . . . .	13
1.4	Motivation for SiECA . . . . .	18
<b>2</b>	<b>Hardware Requirements and SiPM Capabilities</b>	<b>21</b>
2.1	Design Parameters from EUSO Architecture . . . . .	21
2.1.1	Elementary Cell structure . . . . .	21
2.1.2	Measurement Timing and Event Packet Parameters . . . . .	22
2.1.3	Sensitivity Requirements . . . . .	22
2.2	Single Channel Characterization . . . . .	23
2.2.1	SPOCK . . . . .	23
2.2.2	Characteristic Parameters for SiPM . . . . .	25
2.3	Measurement of SiPM arrays in SPOCK . . . . .	26
2.3.1	Single Channel Characterization Theory . . . . .	26
2.3.2	Measurement Method . . . . .	28
2.4	Results of Single Channel Measurement . . . . .	29
<b>3</b>	<b>SiECA Design and Construction</b>	<b>33</b>
3.1	SiECA Mechanical Design . . . . .	33
3.1.1	PCB, Frame, and Shielding . . . . .	34
3.1.2	Sensor-Filter Gluing . . . . .	37
3.1.3	Attachment to Host Camera . . . . .	39
3.2	SiECA Electrical Design . . . . .	40
3.2.1	Si-EC Board . . . . .	40

3.2.2	Data Acquisition and Mezzanine Boards . . . . .	41
3.2.3	External Interfaces . . . . .	42
3.3	SiECA Signal Processing and Data Generation . . . . .	43
3.3.1	Initialization of System . . . . .	43
3.3.2	Sensor and Front Board Signal Handling . . . . .	43
3.3.3	DAQ and Mezz Digitization with Citiroc . . . . .	44
3.3.4	FPGA Gate Timing, Trigger Processing and Packet Generation . . . . .	45
<b>4</b>	<b>Camera Calibration</b> . . . . .	<b>47</b>
4.1	Camera Calibration . . . . .	47
4.1.1	HV and ASIC capabilities . . . . .	47
4.1.2	Gain Flat Fielding Theory . . . . .	48
4.1.3	PDE Flat Fielding Theory . . . . .	49
4.1.4	Flat Fielding Results . . . . .	49
4.2	Sensitivity and Response of SiECA . . . . .	53
4.2.1	Single Channel Illumination . . . . .	53
4.2.2	Illuminated Flat Field test . . . . .	55
<b>5</b>	<b>SiECA Deployments</b> . . . . .	<b>61</b>
5.1	EUSO-SPB1 . . . . .	61
5.1.1	SiECA issues on EUSO-SPB1 . . . . .	62
5.1.2	Low Count Events . . . . .	64
5.1.3	High Count Events . . . . .	64
5.2	Pierre Auger Observatory, HEAT . . . . .	65
<b>6</b>	<b>Conclusions</b> . . . . .	<b>67</b>
6.1	Hardware . . . . .	67
6.1.1	Connector or SMD MPPC . . . . .	67
6.1.2	PCB Warp . . . . .	69
6.1.3	ASIC Considerations . . . . .	70
6.2	Final Remarks . . . . .	70
<b>A</b>	<b>Appendix A: Schematics</b> . . . . .	<b>71</b>
A.1	Mechanical Drawings . . . . .	71
A.2	PCB Layout . . . . .	91
A.3	Citiroc Architecture . . . . .	96
<b>B</b>	<b>Appendix B: Plots</b> . . . . .	<b>97</b>
B.1	Calibration Characteristic Plots . . . . .	97
B.1.1	Gain before Flat Fielding at given Bias Voltage . . . . .	98
B.1.2	PDE before Flat Fielding at given Bias Voltage . . . . .	99
B.1.3	Gain after PDE Flat Fielding at given Bias Voltage . . . . .	100
B.1.4	PDE after Gain Flat Fielding at given Bias Voltage . . . . .	101
B.2	Signal to Noise Ratio measurements . . . . .	102
<b>C</b>	<b>Appendix C: Operation Manual</b> . . . . .	<b>105</b>
C.1	Single Channel Analysis . . . . .	105
C.1.1	qadc_peakfinding_wp.py . . . . .	105
C.1.2	process_SiPM_measurement_wp.py . . . . .	105
C.1.3	FFC2.cpp . . . . .	105
C.2	SiECA Operation Guide . . . . .	106

C.3	SiECA with RaspberryPi in SPOCK . . . . .	106
C.3.1	AxisHelper.py and AxisPrep.py . . . . .	106
C.3.2	SiECA2Dscan.py and SiECA2Dscan2.py . . . . .	107
C.3.3	SiECAparameterscan.sh . . . . .	107
C.4	SiECA Data Analysis . . . . .	107
C.4.1	EventViewerSCA.cpp and EventViewerRoot.cpp . . . . .	107
C.4.2	SiECABinaryReader.cpp . . . . .	108
C.4.3	FlightAnalysis.cpp . . . . .	108
C.4.4	SiECA_SNR2.cpp . . . . .	108
C.4.5	SiECA2D.cpp . . . . .	108
C.5	Remarks on other scripts . . . . .	108
<b>7</b>	<b>Acknowledgments</b>	<b>109</b>



---

# Todo list



---

---

# CHAPTER 1

---

## Historic Background

As this thesis focuses on the development of SiPM<sup>1</sup> based detection of UHECRs<sup>2</sup>, specifically the fluorescence emission, it is necessary to provide a background in both high energy astro-particle physics and solid state electronics. These introductions are not meant to be exhaustive but will provide the necessary foreward for understanding the challenges and capabilities dealt with in the main body of this work.

### 1.1 Development of Silicon Detectors

While several semiconductors were of importance in the long development of solid-state semi-conducting devices now ubiquitous in all electronics, this work is most interested in those constructed of silicon. In the following section we look at the key features of this element that facilitate the electrical characteristics useful in detector construction. Starting with the widely used silicon particle detector and then moving through the single channel avalanche and Geiger-mode avalanche photo-diodes (APD<sup>3</sup> and GAPD<sup>4</sup>) to the high density, parallel arrays of GAPDs commonly called SiPMs, a growing description of the structure and function of these devices will be completed before moving to application in the main chapters of this thesis [1].

#### 1.1.1 Silicon Particle Detectors

In essence, all silicon based particle detectors are biased p-n junctions that collect the generated charge when an electron and hole are generated through interaction of a charged particle or photon in the active sensor volume. In the case of silicon strip detectors, charged particles are of interest for particle accelerator generated collisions. By introducing defects in the silicon crystal structure (Group IV, 4 valence electrons) with dopants from Group III for p type and Group 5 for n type, the presence of excess holes (positive charge) or electrons (negative charge) in the silicon lattice are introduced allowing for the construction of solid state logic and detector devices [1, 2].

---

<sup>1</sup>Silicon Photo-Multiplier

<sup>2</sup>Ultra-High Energy Cosmic Rays

<sup>3</sup>Avalanche Photo Diode

<sup>4</sup>Geiger Avalanche Photo Diode

By reverse biasing this junction, a depletion region is created that prevents current from crossing from anode to cathode. An incident charged particle excites electrons in the depleted region leading to the creation of an electron-hole pair. Given the electric potential between the anode and cathode, the hole and electron are pulled in opposite directions due to their effective opposite charge and the biasing potential. Movement and subsequent collection of the generated ionization current in the form of separated electron-hole pairs can be amplified and measured to provide both the accurate time of interaction and the amplitude of the charge current, equivalent to the ionizing potential of the incident charged particle. In order to limit thermal noise, these detectors are operated under cryogenic conditions effectively freezing out spontaneous thermal electron-hole pair generation [1].

### 1.1.2 Geiger-Avalanche Photodiodes

Geiger-Avalanche photodiodes are structurally similar to silicon particle detectors however they are optimized for detection of photons utilizing the photoelectric effect for electron-hole production. The production of an electron-hole pair leads to a collected charge however the reverse biasing voltage is maintained above breakdown voltage for the p-n junction. With sufficiently high reverse bias voltages, the electron is accelerated rapidly and acts as ionizing radiation producing a secondary electron pair through impact ionization. The resulting avalanche of charge requires quenching before the discharge current exceeds the heat dissipation of the junction leading to thermal damage. In modern devices, this is handled by an

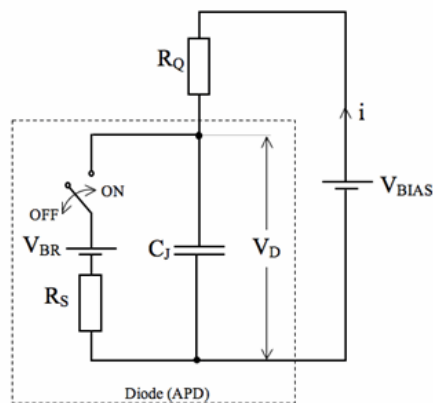


**Figure 1.1:** APD simplified circuit schematic [3]

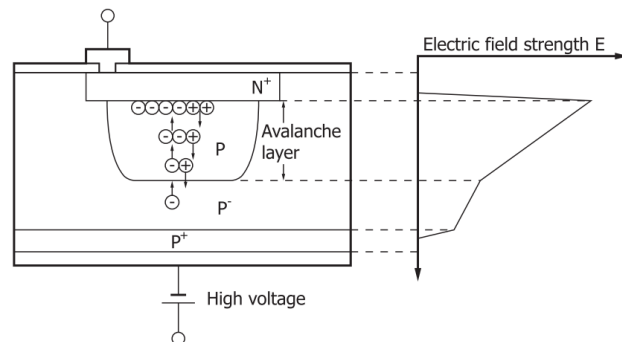


**Figure 1.2:** Silicon doping structure and electric field strength within APD cell [3]

internal biasing capacitor ( $C_J$ ) and resistor ( $R_Q$ ) circuit. When an electron is ionized and a breakdown channel is created through secondary ionization, the charge on  $C_J$  is allowed to pass through the junction. The capacitance is a balance between quick recharge times and signal charge amplitude: lower capacity makes for faster recharging but a smaller amplitude charge signal. By discharging the capacitor, the bias voltage across the junction drops below the breakdown voltage and the avalanche is quenched. Thus, a single photon initiates a cascade of ionization that progresses through the depletion region of the p-n junction until quenched by the discharged bias capacitor. The consistency of the generated charge for an incident photon is inherent, similar to that of a PMT<sup>5</sup>, and we refer to the charge generated for a single photon initiated discharge as a photo-electron (PE<sup>6</sup>).

<sup>5</sup>Photo-Multiplier Tube

<sup>6</sup>Photo-Electron, photon to charge ratio in a photomultiplier

### 1.1.3 Silicon Photomultipliers

Single channel APDs cells can currently be as small as  $10 \mu\text{m}^2 \times 10 \mu\text{m}^2$ . Construction of many of these cells in parallel to form a multi-cell detection surface creates a device that retains the single photon sensitivity but can measure multiple simultaneous photons, one per APD cell. These devices are collectively called SiPM, or MPPC<sup>7</sup> by Hamamatsu. Connection of the APDs in parallel provides uniform bias voltage to each channel and collects the total charge generated from an incident event. As each APD cell contains the bias capacitor, discharging one APD has no impact on other channels so continuous measurement is possible, however, a second photon arriving in an APD during the recharging phase is unlikely to generate a full avalanche as the electric field in the avalanche region is still recharging. In order to maximize sensitivity, APD cells in SiPM are placed as closely as possible. This tight packing, however, leads to signal contamination in the form of optical cross-talk in which excited electrons relax and release a photon that initiates a secondary cascade. If the secondary cascade occurs in the same APD it is called ‘after-pulsing’ as the relaxation often occurs detectably later than the initial excitation. If the photon transverses to a second APD then this is optical cross-talk. Both of these effects are primarily caused by defects in the silicon structure such as a mis-aligned dopant or multiple dopant occupation of a binding site in the crystalline structure [3]. The APD cell size creates a compromise between dynamic range (number

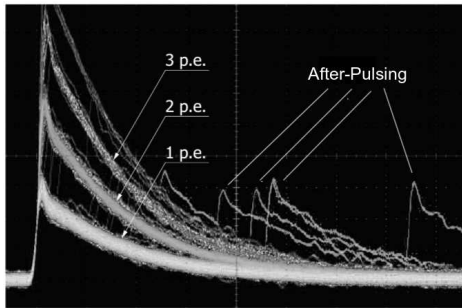


**Figure 1.3:** Older MPPC exhibiting cross talk (left) and after-pulsing noise effects [3]

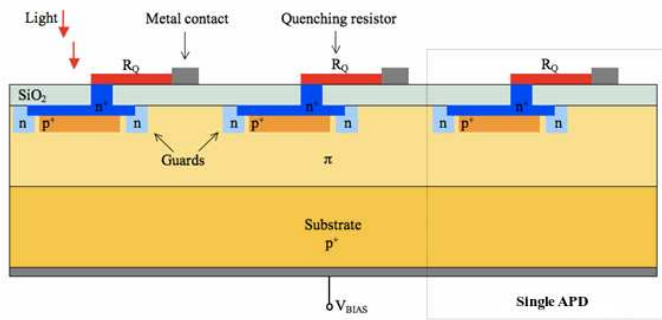


**Figure 1.4:** Hamamatsu MPPC schematic. Guards prevent drift and cross talk electrons and photons from entering avalanche region from the side [3]

of APDs per SiPM channel) and fill factor as the separation between APDs cells does not scale with sensitive area. Within each APD, the probability of an electron being excited into the conduction band for an incident photon of wavelength  $\lambda$  is quantified by the quantum efficiency. The quantum efficiency of the APD cell is partially determined by the depth of the depletion region as longer wavelengths can penetrate the silicon deeper than shorter wavelength photons. In this way, long wavelengths can be filtered by reducing the depth of the depletion region but this also reduces the efficiency for shorter wavelength photons. The geometric factor ( $\eta_{FF}$ ), along with the quantum efficiency ( $\eta_{QE}(V)$ ) and the avalanche probability ( $P_{AV}(\lambda, V)$  which is the likelihood of an electron excited into the conduction band generating an avalanche) are used to calculate the PDE<sup>8</sup>( $\lambda, V$ ) of a SiPM channel.

$$PDE(\lambda, V) = \eta_{FF} \cdot \eta_{QE}(V) \cdot P_{AV}(\lambda, V) [3, 4]. \quad (1.1)$$

In the case of single channel SiPM the connection of the cathode and anode to bias and readout can be done at the edge as seen in Figure 1.5, however, this is not the case for

<sup>7</sup>Hamamatsu Multi-Pixel Photon Counter

<sup>8</sup>Photon Detection Efficiency, a product of quantum efficiency and fill factor and avalanche probability

closely locating MPPC channels in a square array as in Figure 1.6 where the additional edge area would prohibit square sensor array construction and substantially decrease the active area of a combined array. Hamamatsu addresses this issue by utilizing TSV<sup>9</sup> architecture in which the cathode is connected through the central via in each channel. Commercial

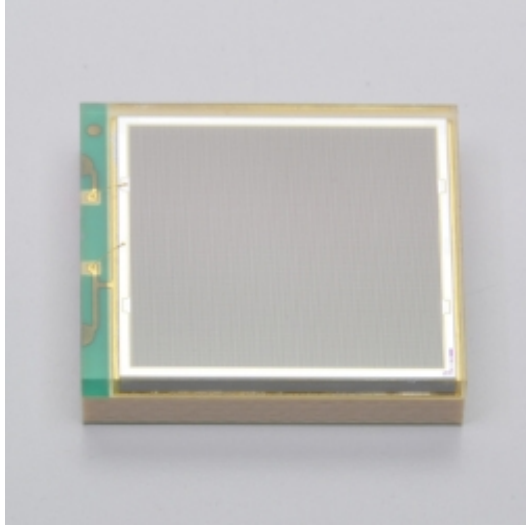


**Figure 1.5:** Hamamatsu 6 mm MPPC with anode and cathode connections on left side [5]

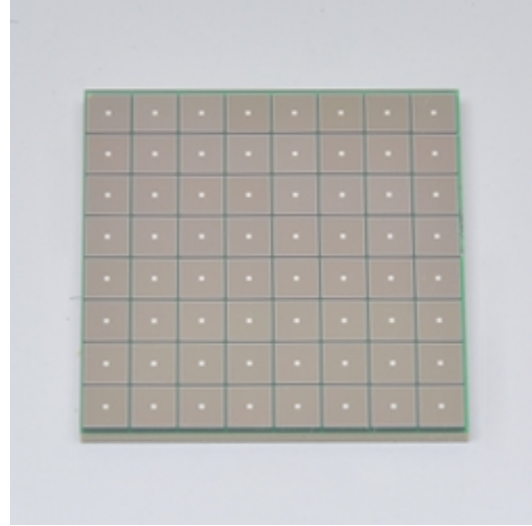


**Figure 1.6:** Hamamatsu 8x8 array constructed of 3 mm TSV MPPCs (note the light metallic via in the center of each channel)[6]

SiPMs silicon are mounted on PCB<sup>10</sup> support boards to provide durability and accessible connections either through SMD<sup>11</sup> solder points or connectors. Routing of the anode and cathode of each channel individually allows for selective biasing and direct control over the operating parameters of each channel. The impact of operating temperature on silicon devices is well explained in solid state theory. As we expect to operate these SiPMs well above the critical phonon freeze out point, and in a linear region, we can use the guidelines from the manufacturer concerning dark count rate and gain temperature dependence as published in [6] and evaluated in [7]. As such, we will not further evaluate the impact of temperature directly in this work but any future application is advised to carefully assess the expected thermal variation during device operation and make corrections as necessary.

#### 1.1.4 Comparing SiPMs and PMTs

From these characteristics, SiPMs are designed to be the solid state replacement for vacuum photomultipliers. This section is a brief comparison between the two on key parameters with a few notes on application specific matters arising from the application of photomultipliers for imaging sensors specifically for application in astro-particle physics. For this comparison we will consider two Hamamatsu sensors, the R11265<sup>12</sup> and the S13361<sup>13</sup> as comparable arrays of similar size and number of channels. This is meant to be mostly general differences but key aspects specific to the application in this thesis will be presented in the lower portion of the table.

<sup>9</sup>Through Silicon Via, via through silicon for anode connection

<sup>10</sup>Printed Circuit Board

<sup>11</sup>Surface Mount Device, electronic

<sup>12</sup>Hamamatsu R11265-113-M64 MOD2 64 channel MAPMT

<sup>13</sup>Hamamatsu S13361-3050AS-08 64 channel MPPC

**Table 1.1:** Key Characteristics of MPPC and MAPMT<sup>14</sup>

	S13361	R11265
Operation Voltage	(51.65±0.11) V [7]	-1000 to -1100 V [8]
Gain	(2.10±0.07)×10 <sup>6</sup> at 55.2 V [7]	1.0×10 <sup>6</sup> [8]
PDE	44.58±1.80 % at 55.2 V [7]	35% [9]
Spectrum	270 to 900 nm Peak 450 nm [6]	300 to 650 nm Peak 340 nm [8]
Fill Factor	74% [6]	72% [8]
Dark Noise	0.5 to 1.5 MHz at 25 °C [6]	≈10 Hz [10]
Temp. Correction	54 mV/°C [6]	Negligible
Dimension (LxWxH)	25.80×25.80×1.35 mm [6]	26.2×26.2×17.4 mm [10]
Unit Cost	1600€/Unit	1600€/Unit

Most notable on the above table are the difference in operation voltage and the stack height advantages of MPPC over MAPMT. However, the thermal noise and dark noise issues must be mitigated to provide a sensor with the same single photon resolution. Thermal noise is clearly handled by operating a cooling system to maintain the silicon junction at a lower temperature. Cold operating temperatures (damage has not been observed in tests performed down to -70 °C) also substantially decreases the dark count rate as fewer thermal excitations lead to avalanches [7, 11]. To further reduce dark counts, decreasing the operating voltage lowers the potential for a thermally excited electron to initiate an avalanche unless sufficiently excited by a high energy photon. This decrease in the accelerating potential also decreases gain and PDE as discussed in detail in the chapter concerning Calibration.

## 1.2 Non-Terrestrial Radiation

While this thesis is primarily concerned with hardware, the motivation for the development of low light, UV<sup>15</sup> sensitive imaging telescopes for cosmic rays is required. As many authors and scholars have written more elegant and exhaustive works on the history of cosmic ray discovery and measurement, I will provide a timeline with the most notable points and references for further reading in place of rephrasing well established material.

### 1.2.1 Historic Milestones in Cosmic Ray Physics

This time line is by no means complete but it contains the most relevant points in the research pertaining to high energy cosmic rays. The early papers originally published in German have been found by consulting the compilation and combined history by Jörg Hörandel [12].

With this historic introduction we are now prepared to describe the current state of cosmic ray research. The continual development of detectors from the highly sensitive but relatively small Alpha Magnetic Spectrometer 01 [32] and 02 [33] to the expansive sparse arrays of scintillators and fluorescence telescopes of the Pierre Auger Observatory [34] and Telescope Array [35] sites have expanded the understanding of cosmic rays from generic 'ionizing radiation' to a composite mixture of fully ionized nuclei varying in mass from single protons up to and possibly beyond iron, high energy gamma rays, high energy neutrinos and possibly exotic particles. Measurement of the energy spectrum of arriving cosmic rays, both directly for energies less than between 10<sup>14</sup> to 10<sup>15</sup> eV and indirectly for those of greater

<sup>15</sup>Ultra Violet light, wavelength 10 to 400 nm

**Table 1.2:** Brief History of Cosmic Rays

1909	• Th. Wulf built and tested his Electrometer measuring ionizing radiation in the air at ground level and atop the Eiffel tower [13–16]
1912	• V.F. Hess shows ionizing radiation increases above 1400 m and is not correlated to solar illumination. Nobel Prize in 1936 for discovery of cosmic rays [17]
1913	• W. Kolhörster confirms Hess’s measurements and extends up to 9 km [18]
1928	• H. Geiger and W. Müller construct practical Geiger-Müller tube allowing for automated, higher elevation and coincident detection of ionizing radiation [19]
1929	• W. Bothe and W. Kolhörster collaborate using two Geiger-Müller tubes to record coincidence events with variable shielding thickness. Bothe receives Nobel Prize in 1954 for application of coincidence in measurement [20]
1930	• H. Bethe theorizes his non-relativistic energy loss equation [21] with subsequent relativistic and other corrections by F. Bloch [22], and others, commonly called the Bethe-Bloch equation
1933	• P. M. S. Blackett and G. P. S. Occhialini show high energy particles can produce showers of particles using a cloud chamber and cameras triggered by coincident Geiger-Müller tube discharges [23]
1934	• H. Bethe and W. Heitler determine the energy distribution for the creation of electron-positron pairs by fast particles. This constitutes most of the electromagnetic component of current air shower models [24]
1936	• G. Pfozter measures the ionizing radiation intensity altitude up to 29 km and determines the maximum occurs at approximately 15 km ASL <sup>16</sup> [25]
1937	• M. Blau and H. Wambacher record heavy shower products through photographic emulsion indicating additional atomic disintegration paths and leading to hadronic interaction models [26]
1938	• W. Kolhörster [27] and P. Auger [28–30] measure coincident events with two and then three Geiger-Müller tubes at extended separations up to 75 m.
1947	• C. M. G. Lattes, G. P. S. Occhialini & C. F. Powell measure accurately the characteristics of charged $\pi$ -mesons which constitute the hadronic component of EASs <sup>17</sup> [31]

primary energy, provides indication of the characteristics and hints to their origins. From the combined efforts of space based direct detection and ground based indirect detection, the flux of cosmic rays at each energy has been accurately measured up to primary energies of  $10^{20}$  eV where statistics are limited by the low incidence, approximately one event per square kilometer per century. The extensive range in energy and flux seen in Figure 1.7 is scaled by energy to highlight structural features. Fitting the entire spectrum with a single power law relation:  $\frac{dN}{dE} \propto E^{-\gamma}$  provides an estimation of the spectral index  $\gamma \approx 2.7$  [37]. Deviation from this simplistic model provides indications of the energy regimes corresponding to changes in origin, composition and acceleration processes. The steepening of the spectrum near  $3 \times 10^{15}$  eV (knee) is suspected to be due to suppression of light primaries while the steepening at near  $4 \times 10^{18}$  eV (ankle) is thought to be evidence of the transition from galactic to extra-galactic sources. The high energy cosmic rays, with energies between the knee and the ankle, have been well measured by KASCADE and KASCADE-Grande with resolution in primary composition through measurement of the charged particle and muon components of the EAS and comparison with simulation [38]. Extension of this measurement to the highest energies is expected with the Pierre Auger Observatory upgrade adding scintillator panels to each of the water Cerenkov detectors in the array and providing sensitivity to the

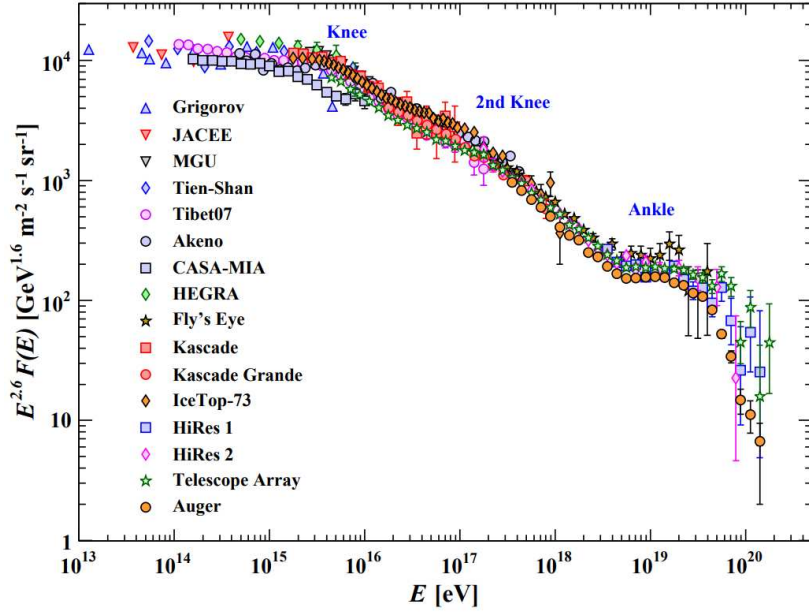


**Figure 1.7:** Total cosmic ray flux scaled by energy to resolve characteristic features. Steepening of the spectrum near  $3 \times 10^{15}$  eV, the knee, and flattening near  $4 \times 10^{18}$  eV, the ankle. Flux suppression above  $5 \times 10^{19}$  eV is apparent but uncertain due to low statistics [36]

muon component of the detected EAS [39]. For an exhaustive list of experiments detecting cosmic rays, please consult [40].

For indirect measurement of cosmic rays by studying the EAS signature, the separation of energy amongst the charged particles, muons and hadronic particles through the processes shown in Figure 1.8 is sufficient to reconstruct the primary composition and energy. Incident cosmic rays begin their EAS near the top of the dense atmosphere, approximately 20 km above the surface of Earth. This primary interaction is nuclear in nature, fragmenting a molecule into kaons, pions, protons and neutrons and fragments. The decay processes of each product, secondary scattering, excitation and relaxation of atmospheric nitrogen, and so forth all contribute to the developing air shower and bombarding the ground around the shower core (impact point of the shower center) [40]. Production of kaons and pions from nuclear fragments lead to muons and neutrinos (considered together to form the muonic component for those that reach the ground) but also electrons, positrons and photons (the electromagnetic component). The population of the electromagnetic component can be roughly estimated based on the Heitler Model in which the number of particles after  $n$  interactions is equal to  $2^n$  [24] up until the divided energy of each particle is below a critical energy  $E_c \approx 0.85$  MeV at which point the ionization losses become more significant than the pair production and bremsstrahlung. Thus, the maximization of the electromagnetic component population occurs for an individual particle energy of approximately  $E_c^{em}$ , after which the population decreases [41]. Muons travel much further without interaction and, despite their short rest lifetime, they are able to traverse many kilometers before decaying due to relativistic time dilation effectively extending their lifetime. Likewise, the produced neutrinos have a minuscule interaction cross section, leading them to retain their energy at least until they enter the Earth. Parameterization of the shower development utilizes  $X_0$ , the first interaction point of the EAS in terms of atmospheric depth  $g/cm^2$ ,  $X$ , the current depth of shower propagation,  $X_{max}$ , the depth of maximum electromagnetic population (corresponding to an average particle energy of  $E_c$ ). At this maximal point the shower contains approximately  $N_{max}$  electromagnetic particles with a total energy  $E_m^{em} ax$  which is proportional to the energy

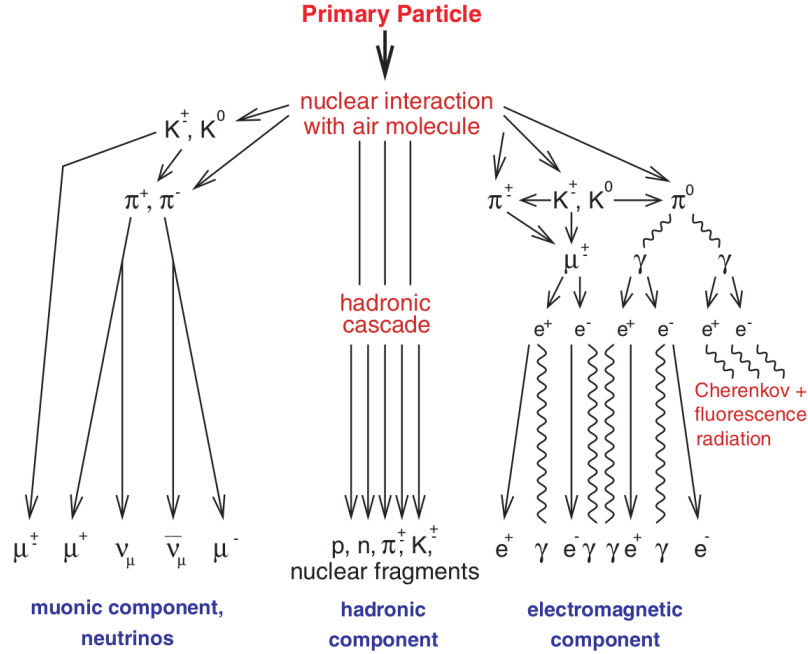
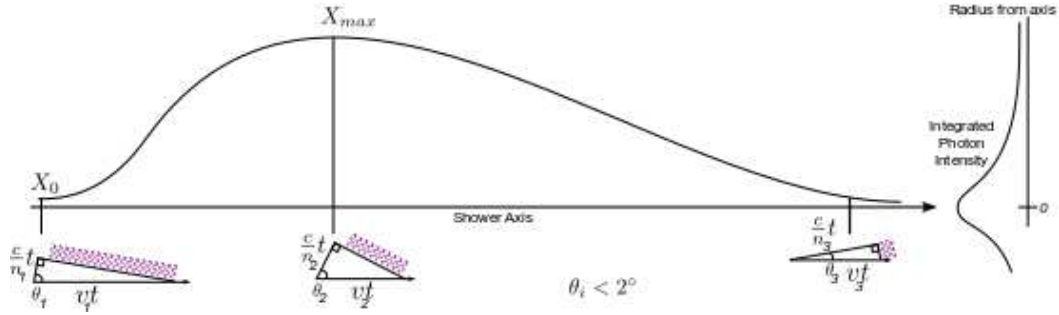


Figure 1.8: Separation of primary EAS development paths [40]

of the primary particle  $E^{primary}$ . For primaries with  $N^{primary} > 1$  nucleon, a superposition of the incident nucleons each with  $E^{primary} / N^{primary}$  allows for the same EAS generation but moves  $X_{max}$  higher in the atmosphere compared to a  $N^{primary} = 1$  event for the same primary energy [37]. The resulting production and extinction effects result in photon emission producing a distinctive shape modeled by the Gaisser-Hillas function to express the longitudinal particle density [42]. Emission of fluorescence light from excited nitrogen in the atmosphere in the violet to ultra-violet range and Cerenkov light also dominantly in the UV range. Measurement of these distinctive emissions with photo-multiplying cameras to determine either the trace, for fluorescence, or elliptical structure for Cerenkov, provides sufficient information to reconstruct the arrival direction and energy of the primary cosmic or gamma ray. Composition information is possible to extract as well if atmospheric conditions are well known and can be further refined with surface measurement of the electronic and muonic components.

## 1.2.2 Cerenkov Light Emission

Given the high energies of the cosmic ray primaries, the secondary charged particles, even after many divisions of the original energy, are imparted velocities in excess of the speed of light in air. While the speed of light in a vacuum is a hard maximum, the small refractive index of Earth's atmosphere ( $n_{air} = 1.00029$  under standard temperature and pressure) provides a narrow margin in which the generated electron-positron pairs can have a boosted velocity  $\beta = \frac{v}{c_{air}}$ , where  $c_{air} = \frac{c=c_{vacuum}}{n_{air}}$ , with  $\beta$  greater than one. This condition leads to the generation of Cerenkov light [43]. Given the low index of refraction of air, which is further decreased with increasing altitude and decreasing density, the maximum angular opening for emission is given by  $\cos(\theta) = \frac{1}{n_{air}\beta}$  where, for example, we assume  $v \rightarrow c_{vacuum}$  yielding  $\cos(\theta) \approx \frac{1}{n_{air} \cdot c_{vacuum} / c_{air}} = \frac{1}{n_{air}^2}$ . This provides a maximal  $\theta$  in air to less than  $1.95^\circ$ . For this well concentrated and directed beaming, angular reconstruction is simplified to measurement of the skew from circular relative to the observing telescope's axis. The radial intensity distribution determines the energy and  $X_{max}$  which constrains the composition. Figure 1.9



**Figure 1.9:** Simplified Cerenkov emission profile following Gaisser-Hillas particle density function with relative radial intensity on right exhibiting integrated Cerenkov signature for on axis EAS measurement

is a simplification neglecting atmospheric density changes along the shower trajectory and attenuation of the photons generated higher in the atmosphere. Additionally, the profile on the right of the figure shows the integrated intensity but the arrival time the Cerenkov photons is reversed from their generated time, leading to a time dependence that further clarifies the Gaisser-Hillas function parameters.

### 1.2.3 Fluorescence Light Emission

Fluorescence light is generated from excited electrons in an atom relaxing to non-excited states and emitting a photon with an energy corresponding to the difference in energy of the excited and non-excited states. As most of the atmosphere is diatomic nitrogen, we consider the nitrogen fluorescence spectrum as the guideline for selecting operating wavelengths for fluorescence detectors (FD<sup>18</sup>). Due to the isotropic emission of fluorescence

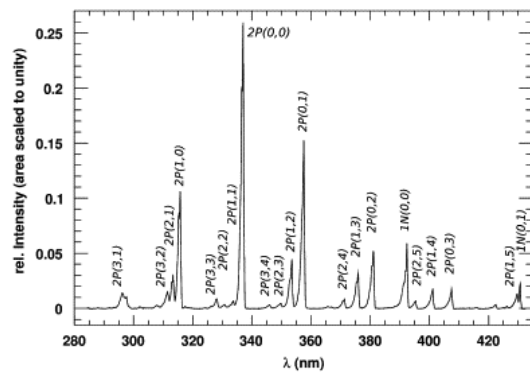


**Figure 1.10:** Nitrogen fluorescence spectrum normalized to unitary emission [44]

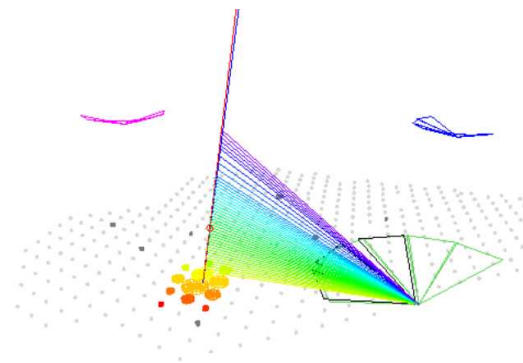


**Figure 1.11:** Pierre Auger Observatory example event with signal in the surface and fluorescence detector [45]

light, detection can be made from any angle relative to the EAS propagation axis but the intensity of the light is substantially reduced compared to that for Cerenkov light. Discernment of the energy is via the calorimetric nature of observing the atmosphere in which the EAS develops. Correcting for attenuation, the fluorescence yield is proportional to the total shower energy. Composition can be determined by the profile before  $X_{max}$  as a primary with  $N^{primary} > 1$  will develop faster, leading to more skewing towards  $X_0$  compared to a shower with  $N^{primary} = 1$ .

Use of both the Cerenkov and Fluorescence signal can be improved by making a hybrid reconstruction considering the charged particle and muon component at ground level

<sup>18</sup>Fluorescence Detector, telescope for fluorescent EAS emission

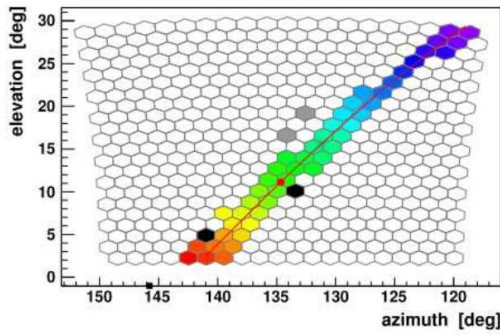


**Figure 1.12:** Event as seen by one Pierre Auger Observatory Fluorescence Telescope Eye [45]

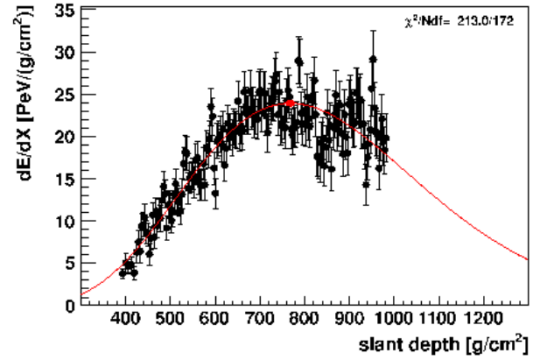


**Figure 1.13:** Fitting of the fluorescence signal with the Gaisser-Hillas function and determined position of  $X_{max}$  (red point) [45]

measured with scintillators (Telescope Array) or water Cerenkov tanks (Pierre Auger Observatory). Separating the muon and charged particle signal remains a challenge. For more information on this matter, please consult [39].

### 1.3 What Cosmic Rays have yet to tell us

Despite the massive detectors dedicated to finding the highest energy cosmic rays, Telescope Array in the northern hemisphere and the Pierre Auger Observatory in the southern hemisphere, statistics at the highest energies remain minimal leaving many questions open. Specifically, what are the acceleration processes capable of producing particles with such high energies? The Hillas plot, Figure 1.14, provides an indication of the magnetic field strength and relative size of several candidate structures that could potentially retain cosmic ray primaries up to nearly the energy that they deliver to EASs on Earth however this does not explain the mechanism of acceleration [46]. So far no definitive sources have been de-

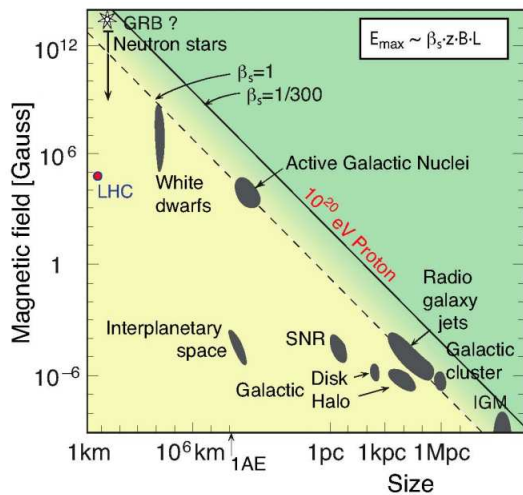


**Figure 1.14:** Plot of possible cosmic ray source sizes and necessary magnetic fields to satisfy the leaky box model for acceleration [46]

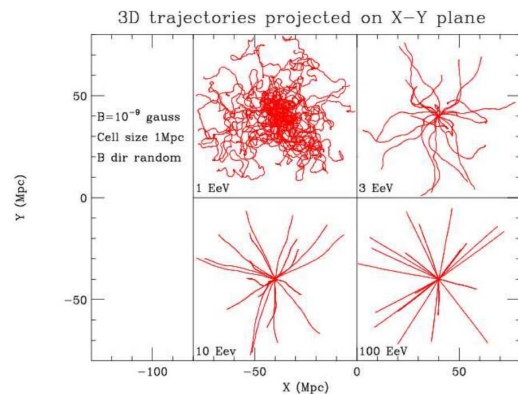
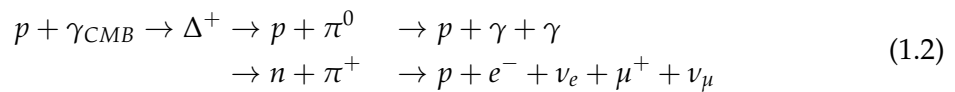


**Figure 1.15:** Simplified simulated random interstellar magnetic field effects for propagating cosmic rays [47]

termined however with increasing statistics, this problem is may be solved with increased observation. As proposed two decades ago, magnetic fields between the accelerator and

the detector will deflect cosmic rays substantially such that only the highest energy protons so far detected will retain a trajectory that indicates their origins. Heavier primaries with  $Z^{primary} > 1$  ( $Z^{primary}$  being the charge of a primary with  $Z$  protons) require proportionally scaled energies to overcome the same magnetic fields. As particles are deflected based on their Larmor radius,  $R_L = \frac{p_{\perp}}{|q|B}$ , for a magnetic field of magnitude  $B$  with a particle of charge  $q$  moving with momentum  $p_{\perp} = \gamma m v$ , where  $\gamma$  the Lorentz factor, perpendicular to the magnetic field, the curvature of the trajectory is given by  $R_L$ . Implementation of this within a random, small field intensity of 1 nG in each 1 Mpc of otherwise empty space and allowing propagation of cosmic rays, as done by James W. Cronin in [47], shows the need for high energy, low charge particles to have a chance to directly identify sources. The search for sources is further complicated by the interaction of UHECRs with CMBs<sup>19</sup> photons through the Greisen–Zatsepin–Kuzmin limit [48, 49] limiting the mean free path of particles with energies above  $5 \times 10^{19}$  eV to less than approximately 50 Mpc through a delta resonance scattering:



The resulting protons after interaction are reduced in energy corresponding to the two  $\gamma$ s or the electron and muon with their corresponding neutrinos. Given the forward boosted nature of the high energy incident photon, the neutrinos are beamed in a direction closely related to the proton's original direction. Due to the high charge to mass ratio of the electron, it is quickly diverted by magnetic fields, similarly for the charged muon. The resulting uncharged neutrinos should continue through space along the boosted trajectory of the incident proton relatively unimpeded other than by a massive object. With current neutrino detectors, measurement of an excess of neutrinos arriving with energies corresponding to the GZK<sup>20</sup> process could provide an indication of at least the first interaction point of a cosmic ray that started with an energy above the GZK cutoff [50, 51].

Given the extremely low flux of high energy cosmic rays arriving at Earth, maximizing the instrumented area efficiently has been the goal since the proposal of the Pierre Auger Observatory and Telescope Array. While these two facilities provide excellent reconstructions with high accuracy and together extend over nearly 3800 km<sup>2</sup>, the collection of events with primary energies above  $1 \times 10^{20}$  eV remains low. One possibility is the expansion of these arrays, however, funding and space for such large projects is already reaching limitations. Alternatively, the Cerenkov and fluorescence light measurement methods can be applied from orbital detectors rather than terrestrial ones, substantially improving the field of view and, thus, the measurement statistics for UHECRs at the highest energies.

### 1.3.1 Extending detection to Space

The Extreme Universe Space Observatory, EUSO<sup>21</sup>, is a telescope designed to look downward through Earth's atmosphere from orbit on-board the ISS<sup>22</sup> in order to detect the fluorescence signatures of EAS [52]. As this device was planned for attachment to the Japanese Experimental Module of the ISS, it is often also called JEM-EUSO but for simplicity we will refer to the telescope irrespective of its designated mounting position. In the development of the EUSO telescope there have been two proof of technology and scientific merit missions, carried by balloons with prototype sensor and readout architecture, EUSO-Balloon and EUSO-SPB1 and a small scale prototype for testing space readiness, Mini-EUSO planned

<sup>19</sup>Cosmic Microwave Backgrounds

<sup>20</sup>Greisen–Zatsepin–Kuzmin

<sup>21</sup>Extreme Universe Space Observatory

<sup>22</sup>International Space Station

for use from inside the ISS through an UV transparent window. For a collection of EUSO related papers, please consult Michael Karus's Thesis [41] citations 40-61. Due to the expected obsolescence date of the ISS plans for a free flying mission, called POEMMA<sup>23</sup>, incorporating detection of Earth skimming neutrinos, stereo measurement by operation of two co-orbital telescopes and a much larger field of observation by operating in a limb pointed orientation [53].

## EUSO Design

The goal of refining the high energy limit of the cosmic ray spectrum requires extensive exposure to generate a statistically significant measurement. The EUSO telescope is designed to be sensitive to EAS with energies down to  $10^{18}$  eV and possibly lower under ideal conditions. Measurement of the flux at these energies should indicate sources through arrival direction reconstruction and assist in resolving the limitations of higher energy cosmic rays, limited acceleration potential or interaction in transit such as through the GZK process. With the complications and duty cycles of fluorescence detecting telescopes, flight profile of the ISS and the current UHECR flux measurements, a scientific goal for EUSO is on the order of  $10^3$  cosmic ray events with energies in excess of  $8 \times 10^{19}$  eV [54].

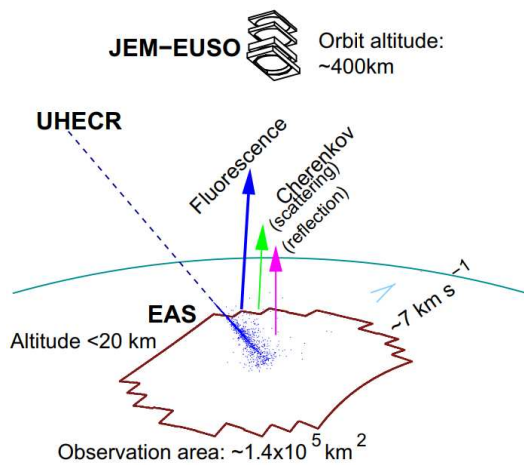


**Figure 1.16:** Nadir operation mode of EUSO [54]

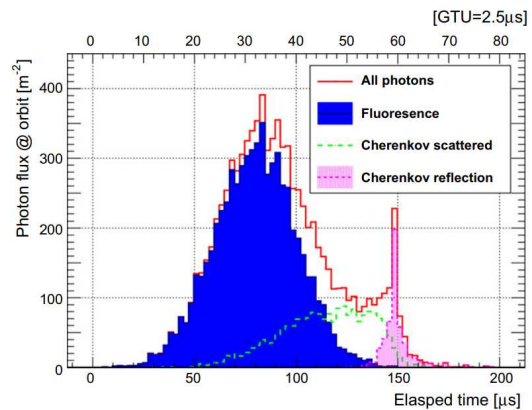


**Figure 1.17:** ESAF simulated light at EUSO aperture for  $60^\circ$  proton with  $10^{20}$  eV [54]

When oriented directly downward, as seen in Figure 1.16, the average pixel width of  $0.074^\circ$  corresponding to a square area on Earth's surface with side length between 0.5 to 0.7 km depending on distance from center. This spacing is primarily driven by available technology both in the sensor and speed of ASIC<sup>24</sup> chips capable of operating on a limited power budget [55]. A horizontal shower moving with speed  $c$  through the field of view at ground level will pass through the smallest channel ( $0.517 \text{ km} \times 0.517 \text{ km}$ ) side to side in  $1.725 \mu\text{s}$  and corner to corner in  $2.439 \mu\text{s}$  so the selected integration time for measurement, called a Gate Time Unit or GTU<sup>25</sup>, of  $2.5 \mu\text{s}$  is acceptable. Simulation of shower development, light propagation and detection have been implemented to refine the detection system and establish limits on the energy and resolution of reconstruction. An example light profile, seen in Figure 1.17, shows the separation of arriving light into fluorescence, scattered and reflected Cerenkov signals [54].

<sup>23</sup>Probe Of Extreme Multi-Messenger Astrophysics

<sup>24</sup>Application Specific Integrated Circuit

<sup>25</sup>Gate Time Unit. EUSO measurement time binning

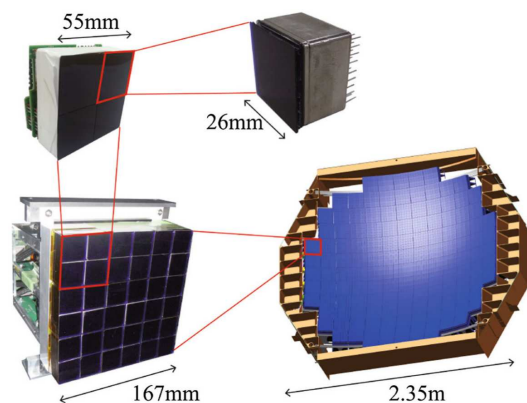


**Figure 1.18:** Breakdown of the EUSO focal surface [55]

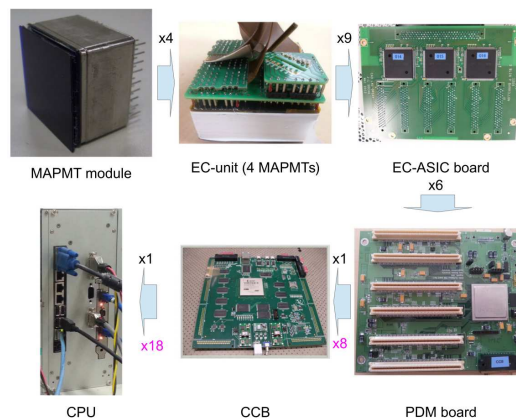


**Figure 1.19:** Readout architecture from sensor to CPU<sup>a</sup> [55]

<sup>a</sup>Central Processing Unit, computer within EUSO-SPB1 Data Processor

The focal surface of EUSO is composed of 137 PDM<sup>26</sup> modules, each containing nine EC<sup>27</sup> units which are constructed of four 64 channel R11265 MAPMTs with similar characteristics. Each PDM contains a high voltage generation board for biasing the MAPMTs with a quick cutoff capability to prevent damage in the case of incident, intense light which could otherwise destroy the camera. Each channel of the MAPMTs is connected to a dedicated Spaciroc<sup>328</sup> ASIC. With 36 MAPMTs per PDM, 36 Spaciroc3s are distributed on six EC-ASIC boards where the charge is integrated in each GTU and communicated to the PDM board. First and second level triggering algorithms are handled on the PDM board with communication via the CCB<sup>29</sup> linking 8 neighboring PDM boards for events that occur across multiple PDMs. Triggers surviving quality cuts initiate a readout process at the CCB level which calls for the relevant 128 GTU block from each PDM board's local memory. The combined data from the involved PDMs is packaged with telemetry and device information and sent to the CPU for further processing, storing or transmission. For details on the operation, trigger logic and communication structure, refer to [55]. For the smaller prototype cameras, the CCB board is redundant as only one PDM is utilized. The specified optics for the EUSO telescope are three Fresnel lenses cut from PMMA<sup>30</sup> to accurately focus light from the  $\pm 30^\circ$  FoV<sup>31</sup> onto the 2.5 m radius curved focal surface [55]. Fresnel lenses and PMMA have been selected due to the large opening angle and weight restrictions required for an orbital device of this design.

### EUSO-Balloon and EUSO-SPB1 Design

Two prototype balloon-borne missions have been carried out as pathfinders for a full scale EUSO mission. In both balloon telescopes, a single PDM constituted the focal surface and a smaller CCB board was used to save power consumption but all other aspects of the full EUSO telescope design were present. The scaled lenses manufactured from 1 m<sup>2</sup> of 10 mm thick PMMA show that the process is achievable but absorption remains high and the point

<sup>26</sup>Photo Detection Module: 9 ECs integrated

<sup>27</sup>Elementary Cell: 4 MAPMTs potted together

<sup>28</sup>64 channel MAPMT ASIC developed by Omega/LAL

<sup>29</sup>Cluster Control Board, manages 8 PDMs in EUSO architecture

<sup>30</sup>Poly(methyl methacrylate) or acrylic glass

<sup>31</sup>Field of View angle or angles defining area observed by telescope

spread remains less than desirable with current methods [56]. For this reason the second of the three lenses, for correction of wavelength dependent defocussing, was omitted from the EUSO-SPB1<sup>32</sup> flight. The omission decreased the energy threshold substantially which, due to the steep energy dependence on cosmic ray flux, meant the expected flight time of 60 to 100 days would be sufficient to achieve the science goal of at least 10 triggering fluorescence cosmic ray events and two triggering backscatter Cerenkov events. In order to maintain oper-



Figure 1.20: EUSO-SPB1 [56]

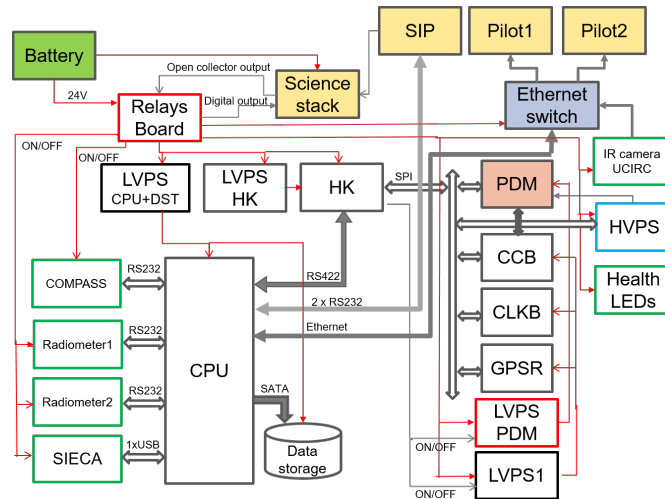


Figure 1.21: EUSO-SPB1 electronic architecture [57]

ation for this extended flight, the design of the gondola (collective term for the telescope and support hardware) used for EUSO-Balloon<sup>33</sup> was substantially changed for the EUSO-SPB1 mission. Movement of the batteries next to the electronics and sensors to keep them at operational temperatures and insulation of the upper portion of the telescope resulted in a top heavy device despite the ballast and solar panels being located at the bottom. Telemetry and communications hardware are located above the telescope electronics box. The white frame facilitates connection of the gondola to the balloon tether, structural support for all the necessary hardware and reduces the mechanical loading on the telescope structure. The internal structure of the telescope remains rather simple. The two lenses are supported by thin frames to prevent bowing under their own weight. Spacing of the lenses and position of the PDM was determined by careful measurement and secured with a sliding structure within the lens box [56]. All the batteries, electronics and the PDM are located in a separable box that attaches to the lens box before being rolled into the white support structure. An additional light baffle is attached below the lens box to reduce stray light entering the telescope from bright, out of FoV sources to reduce the detected background. Please consult NASA<sup>34</sup> for information concerning the telemetry system and science stack mounted at the top of the EUSO-SPB1 gondola. Within the electronics box is almost everything not in yellow in Figure 1.21. This collection of devices are separated physically into the left, center and right compartments shown in Figures 1.22 and 1.23. The right compartment contains the power distribution systems. Individual items requiring voltages different from the nominal 24 V battery have separate LVPS<sup>35</sup> systems for generation and modulation of other voltages. The

<sup>32</sup>Payload of NASA SPB-2017 mission. Launched 5.4.17

<sup>33</sup>EUSO prototype flown 25.8.2014 from Timmins, Ontario

<sup>34</sup>National Aeronautics and Space Administration

<sup>35</sup>Low Voltage Power Supply

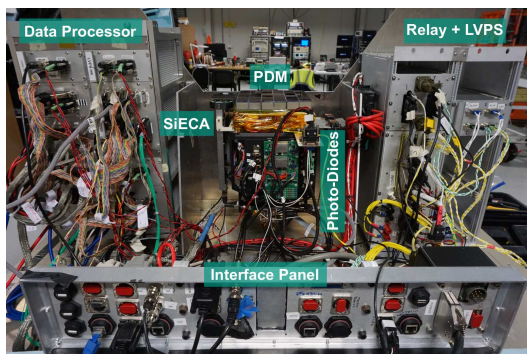


**Figure 1.22:** Layout of EUSO-SPB1 electronics box with large scale components labeled

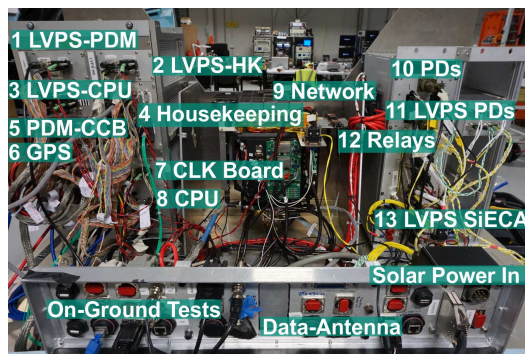


**Figure 1.23:** Labeling of most subsystems indicated in Figure 1.21

central area is purely for the focal surface comprised of the PDM and SiECA<sup>36</sup> and the PDs<sup>37</sup> used as a safety switch to shut down the PDM biasing voltage protecting the MAPMTs in case of bright illumination. The PDs also measure background light levels but during flight these levels are expected to be well below the minimum intensity level to be reliable. Axial positioning of the PDM and SiECA is handled by a dovetailed sliding stage controlled by turning a threaded rod to adjust the axial position of the PDM, SiECA and the PDs. Once positioned at the focal point of the lenses, locking screws are tightened to clamp the sliding block in place. The left compartment contains the processing, data storage, clock and GPS<sup>38</sup> management and a few LVPS units for specific boards. The battery location for this device are obscured behind the aluminum backing plate (behind the PDM and racks). This entire assembly is inverted from the pictured orientation before being fitted into the electronics box.

For a more complete description of the science case, hardware and testing, please see [56, 57]. These missions have clarified the feasibility of building a camera capable of extended deployment and semi autonomous operation. The on-board logic, power systems, data handling and triggering have been verified and further development to improve sensitivity, timing resolution and trigger efficiency can be pursued for future devices. Most immediately is the construction of EUSO-SPB2<sup>39</sup>, which despite the similarity in name is drastically different in design than EUSO-SPB1 and is meant as a prototype for the POEMMA satellite pair.

### POEMMA and EUSO-SPB2

Determining sources of cosmic rays remains a challenge due to the magnetic influence on charged particles, limited ranges due to GZK and other interactions and a lack of the highest energy particles arriving at Earth. With the multi-messenger measurement of the TXS 0506+056 blazar in gamma rays and neutrinos, there is evidence for cosmic ray accelerators producing high energy emissions in multiple species, photons, charged baryons or nuclei, and leptons [58, 59]. While the nuclei provide the most abundant signal, they may not be the most useful in determining the origins of their acceleration processes so it is useful to examine the other species to look for sources. Gamma ray astronomy is well established with

<sup>36</sup>Silicon Elementary Cell Add-on

<sup>37</sup>NIST calibrated light intensity measuring Photodiodes

<sup>38</sup>Global Positioning System

<sup>39</sup>Planned POEMMA prototype for future NASA SPB mission

the work by HESS<sup>40</sup>, MAGIC<sup>41</sup> and VERITAS<sup>42</sup> having found many high energy gamma sources. Neutrino astronomy is a bit more challenging due to the low cross-section for interactions but IceCube is continuing to map the neutrino background and look for sources.

The POEMMA project looks to extend the search for high energy neutrinos generated through the GZK process from space while doubling as a massive extension in the UHECR detection capability currently available. Unlike EUSO, POEMMA intends to make stereo measurements using two free flying telescopes with a range of operating capabilities including a compact mode with maximal overlap for measurement of EAS and a horizontal, nearly parallel mode looking to Earth's limb in search of skimming neutrino events [60]. The idea of the horizontal mode is to detect tau neutrinos of sufficient energy to enter the Earth with a skimming trajectory, interact with matter, produce a tau that leaves the rock and dirt, re-entering the atmosphere and then undergo decay producing charged muons (through charged pion intermediaries) or electrons. Given the energy of the original tau neutrino, the resulting charged muons or electrons will generate Cerenkov light and possibly a detectable EAS however the beamed direction of the Cerenkov light cone will be more readily detected against the limb background light. Most importantly, the tau generated and the subsequent decays should all be in the direction of travel of the original tau neutrino meaning an accurate reconstruction of the event should point back to the acceleration source. The development of POEMMA is undergoing the same methodical approach undertaken for EUSO in developing prototype devices with hardware directly comparable to that of the final telescope. For POEMMA, the next step is a proof of capability to observe events near Earth's limb and discern signal from background. This mission is the motivation for the EUSO-SPB2 telescope also to be carried on a NASA Super Pressure Balloon but completely different in design and function from EUSO-SPB1 despite similar naming. So far, little has been published on the specifications of EUSO-SPB2 but from private communication it is designed to use a restructured PDM that aligns the ECs in a horizontal row rather than a square, elongating the FoV. Two such flat-PDMs will be illuminated by a reflective telescope optical system to remove the absorptive PMMA lenses of EUSO-SPB1 and pointed towards the dark limb during operation via direction controlling hardware between the telescope and balloon. A third PDM is included with a more downward orientation to continue the search for UHECR while the two horizontal 'eyes' look for predominantly neutrino generated skimming events.

## 1.4 Motivation for SiECA

The SiECA camera, the focus of this thesis, was built to test SiPMs as possible replacements for the MAPMTs currently used in the PDM design. As SiPM can now achieve similar sensitivity to their vacuum predecessors and the prices are now comparable, it is reasonable to construct a camera to better understand the practical challenges in addition to the scientific capabilities of these devices. Ideally, SiPM should continue to decrease in price as demand increases as the production of the silicon sensor is automated while MAPMTs are painstakingly assembled by hand. This cost saving, particularly for large orders, makes the construction of a massive telescope with on the order of one million photo-multiplying channels financially feasible in addition to providing scientific advantages. To make a full assessment of currently available technology, hardware components were selected from available devices already on the market. Future developments will improve these devices but a current assessment is needed to determine what areas are of most vital attention. To

---

<sup>40</sup>High Energy Stereoscopic System

<sup>41</sup>Major Atmospheric Gamma Imaging Cerenkov Telescopes

<sup>42</sup>Very Energetic Radiation Imaging Telescope Array System

this end, four S13361 arrays arranged in a square of similar spacing to the EUSO EC, biased by eight C11204-02s<sup>43</sup>, read out by eight Citiroc<sup>44</sup> ASICs controlled by a Spartan6<sup>45</sup> FPGA<sup>46</sup> in an integrated package has been built and tested. The results indicate additional work is needed to refine the ASIC capabilities, improvement in the thermal management and grounding designs is needed to make a stable and reliable camera operable in varied conditions, and the timing will need to be tuned for the desired operation, which differ substantially between the measurement of a Cerenkov or fluorescence signature of an EAS event.

---

<sup>43</sup>Hamamatsu SMD high voltage MPPC bias generators

<sup>44</sup>32 channel SiPM ASIC developed by Omega/LAL

<sup>45</sup>Xilinx Spartan-6 XC6SLX100-2FGG676I

<sup>46</sup>Field Programmable Gate Array



---

---

## CHAPTER 2

---

# Hardware Requirements and SiPM Capabilities

This chapter describes the structures within the EUSO focal surface, the operating parameters and the measurement process that has been established through many individual and collective works. In order to assess the feasibility of using SiPMs in place of MAPMTs, a prototype camera must be built and evaluated. As a first test development, a single EC size camera ( $16 \times 16$  channels with  $3 \times 3 \text{ mm}^2$  area each) SiECA has been constructed and tested. To justify the design of SiECA in the following chapter, the EUSO design and functionality requirements are detailed in this chapter.

### 2.1 Design Parameters from EUSO Architecture

SiECA was designed to function in a similar way to the EUSO EC but constructed of SiPM and with a full event processing electronics chain behind the sensors. As such both the mechanical and electronic aspects are defined by the EUSO structures and they have been maintained where possible.

#### 2.1.1 Elementary Cell structure

As detailed in the Introduction chapter, the EUSO focal surface is comprised of many PDMs. Each PDM is constructed from nine ECs, each containing four 64-channel MAPMTs. The SiECA camera replaces the MAPMTs with four Hamamatsu S13361 MPPCs. These arrays are arranged in a square, just as the MAPMTs are in the original ECs design however, the much lower profile and lack of edge casing with the MPPC allow closer placement of each array to those proximal. Also due to the sensitive area of the MPPC, rectangular filter glass, as opposed to chamfered used with the MAPMTs, can be glued directly to the silicon protective window [61]. To maximize the spatial resolution, MAPMTs are placed as close as feasible within each EC and potted with a resin to prevent electronic discharge between the different high voltage pins. With the attached BG3<sup>1</sup> filters, each MAPMT has an effective focal surface area of  $27 \times 27 \text{ mm}^2$ . A 1 mm separation is left between outermost MAPMT filter edges resulting in a total EC dimension of  $55 \times 55 \text{ mm}^2$ . The PDM design calls for individual EC angling to best approximate the focal surface curvature however this was not implemented

---

<sup>1</sup>Schott BG3 UV-band pass optical filter glass

in the EUSO-SPB1 PDM due to marginal optical improvement for significantly increased mechanical assembly complexity. The supporting circuitry behind the four MAPMTs is conceptually shown in Figure 2.1 and the complete, resin potted version in Figure 2.2 with the high voltage and data kapton ribbons extending.

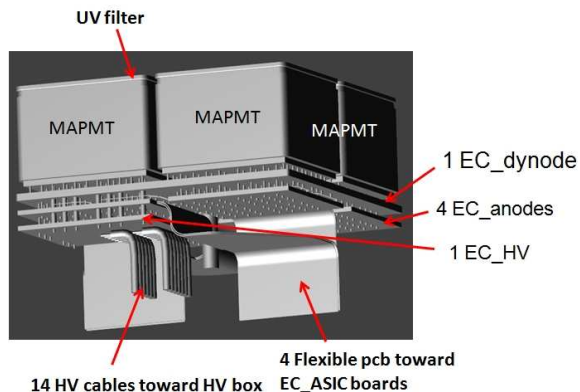


Figure 2.1: Schematic of EC



Figure 2.2: Resin-Potted MAPMT EC

Connection of the EC via the white dynode supply lines to high voltage generators and via kapton printed PCB to the ASIC boards complete the mechanical description of the EC unit. Operation of the nine EC units is handled by the PDM electronics comprising the six ASIC boards which connect to the PDM board [55]. For multi-PDM telescope designs, a CCB board unifies the PDM boards for data handling. The ASIC, PDM, and CCB boards manage the timing, triggering, event processing and data packet generation.

### 2.1.2 Measurement Timing and Event Packet Parameters

The orbital design of EUSO envisions a nominal flight altitude of 400 km attached to the ISS. Considering the  $\pm 30^\circ$  aperture and a focal surface of 137 PDMs, the spacial resolution is 0.074 degree per MAPMT channel [55]. For nadir operation, the pixel size on ground dimensions are 517 m  $\times$  517 m at the axis and 688 m  $\times$  688 m at the edge of the FoV. A reasonable GTU length of 2.5  $\mu$ s corresponds to a horizontal shower (perpendicular to telescope axis) transversing 750 m. A full event in the UHECR range extends for several tens of GTUs with the resulting event packet maintaining the primary event trigger at a specified GTU within the packet containing a total of 128 GTUs [62]. This time binning is a balance between increased integrating time (leading to a higher signal to noise ratio) and finer timing resolution (leading to better trajectory reconstruction). Omega/LAL's Spaciroc ASIC for the MAPMT based PDM was developed for these parameters and has been implemented in the PDM design with modifications as newer revisions have been produced.

### 2.1.3 Sensitivity Requirements

Detection of cosmic ray fluorescence light requires detection of an excess of a few to a few hundred photons above background level, thus, single photon resolution is necessary to achieve the lowest energy threshold [63]. In the Spaciroc chip this is handled in two ways, by counting pulses above a threshold and by measuring the charge peak height (after amplification) in parallel. The amplified and discriminated signal path and two amplified,

shaped and DAC<sup>2</sup> measured peak height paths require approximately 1.4 mW/Channel excluding digital back end. Additionally, a Charge to Time conversion comparing the signal at the anode and dynode can provide information about the background light level and allow for electronic protection of the MAPMTs in the event of bright illumination of the sensors. Measurements of both the peak time and amplitude allow for reconstruction of the EAS with minimal excess data. From these parameters, SiECA was designed to be comparable to a single EC in terms of power consumption, packet dimensions (both GTU length and number of GTUs in each event packet) and incident photon sensitivity.

## 2.2 Single Channel Characterization

Channel calibration is necessary to produce a functional focal surface with useful measurement results. Both hardware calibration and offline measurement correction depend directly on the nature of the devices being used and how they are operated. Particularly in the field of imaging devices, uniform response across the focal surface is required to accurately reconstruct the EAS properties both for arrival direction, energy and composition. For photomultipliers intended for operation in the photon counting regime, this means determination of the gain, dark count rate, cross talk and PDE of each channel. From these measurements we can construct a uniform focal surface with the response characteristics desired for measuring EAS from cosmic rays. Measurement of SiPMs and PMTs with the SPOCK<sup>3</sup> hardware allows for testing down to the single photon illumination level leading to known sensitivity capabilities at the lowest signal intensities.

### 2.2.1 SPOCK

The SPOCK apparatus was developed by Michael Karus. For a complete understanding of this device, how it was designed, constructed and tested, please consult his thesis [41].

SPOCK comprises a large dark box with the calibrated light source, optical table and electrical throughputs for testing and calibration of all types of photo-sensitive sensors. The calibrated light source consists of a Labsphere 3P-GPS-053-SL<sup>4</sup> where the large entrance port is used for the LED<sup>5</sup> array containing a single LED for pulsed and several parallel LEDs for continuous light emission. The exit port, a 2.54 cm opening, is used with a threaded adapter for attaching collimators to the sphere. These collimators allow for the light intensity within the sphere to be substantially reduced between the monitoring PD-A<sup>6</sup> and the collimator output directed at the photomultiplier being tested. Each collimator consists of two small diameter holes separated by a distance with a light absorbing material inside the cavity between entrance and exit. The geometric ratio between the entrance and exit holes, the absorption quality at the measured wavelength and the alignment all contribute to the effective ColRat<sup>7</sup>. For the light intensity and PD available in SPOCK, a ColRat of  $4.0 \times 10^{-6}$  provides sufficient collimation such that the output can be adjusted from a single photon to many tens of photons per pulse while the PD-A measured intensity is within the accurate range, i.e. 1 photon/pulse at 10 kHz corresponds to PD-A observing  $1.174 \times 10^{-6}$  nW for 423 nm wavelength photons. Measurement of the collimator ratio is necessary as close to

---

<sup>2</sup>Digital to Analog Converter

<sup>3</sup>Single PhOton Calibration stand at KIT

<sup>4</sup>3 port, 13.46 cm diameter, 6.35 cm entrance, two 2.54 cm outputs

<sup>5</sup>Light Emitting Diode

<sup>6</sup>Photodiode on SPOCK integrating sphere for light intensity monitoring

<sup>7</sup>Collimator Ratio, emitted intensity over incident intensity

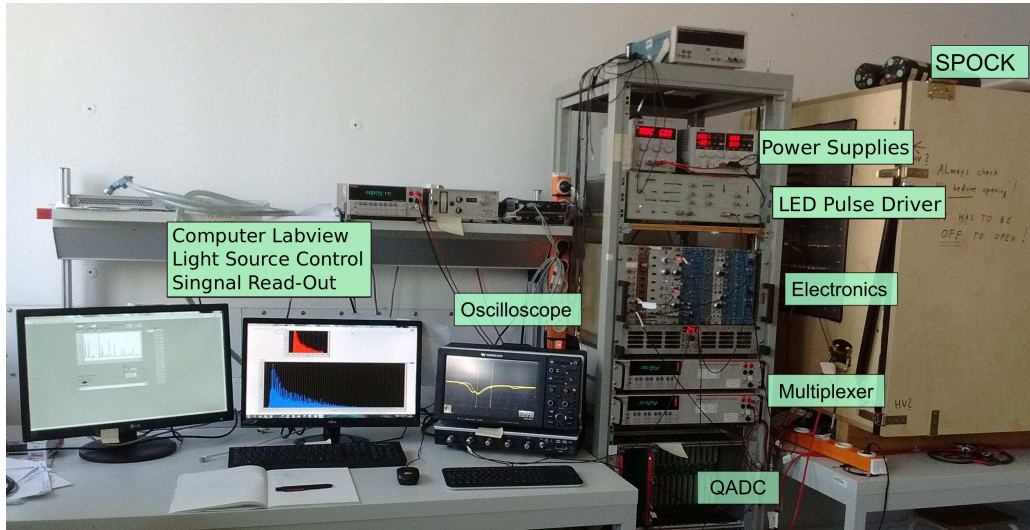


Figure 2.3: SPOCK readout rack, power supplies and PC interface

measurement of each photo-sensor measurement as feasible as temperature variations can impact the response of the PD and SiPM.

In addition to variation, the pulsed light driver has been found to be sufficiently electrically noisy to negatively impact measurement. To minimize this impact, careful isolation of the LED ground path has been performed. The single, centrally mounted LED in the original array design has been replaced with a fiber optic bulkhead allowing for the separation of the sphere from the pulsed LED electrical drive circuit. This fiber optic cable is connected to an aluminum enclosure containing the pulsed LED in such a way that the light emission is directly into the fiber for maximum transmission. A more advanced system utilizing spherical ball lenses has been envisioned but has not yet been implemented. By separating the pulsed LED driving signal ground path from the grounding of the photo-sensor readout connections, the electronic noise from the sensor is substantially reduced for MPPC testing. Parallel testing with MAPMT is expected to show similar benefits but has not yet been done.

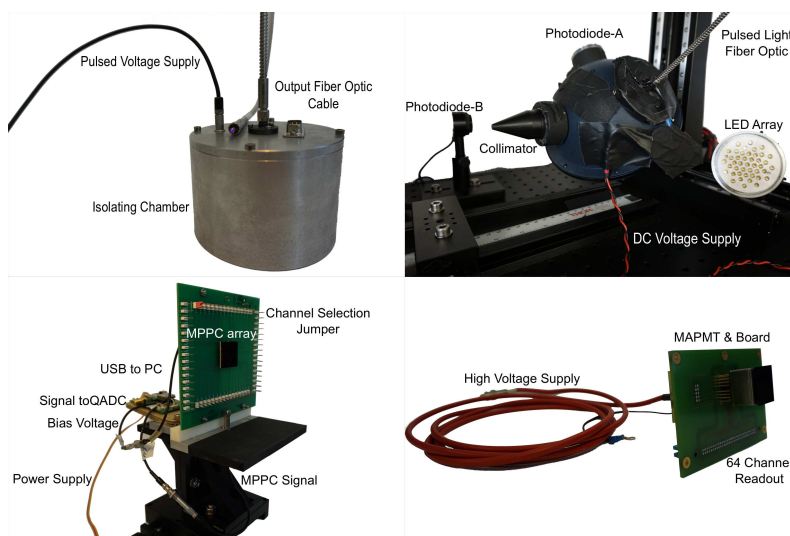


Figure 2.4: Clockwise from Top Left: LED to fiber to integrating sphere light coupling. Integrating sphere with LED array, PD-A and collimator attached. MPPC readout board with S13361 attached and C12332-01<sup>8</sup>. MAPMT readout board with MAPMT attached.

From the calibrated light source, photons are emitted through the collimator to the photo-sensor. The biasing voltage for the photo-sensor can be generated either proximally, as we do with the C12332-01 [64] for MPPC, or externally, as we do for MAPMT with a rack or desktop generator. The signal from the sensor is passed via coax LEMO to the QADC<sup>9</sup>. When calibrating MAPMTs, this connection is direct between the collection anode and QADC channel. When working with MPPC, we have found that a proximally located amplifier (C12332-01) is required to deliver the signal to the QADC without significant distortion. As the amplifier and the MPPC board are both designed for single channel operation, manual switching between channels is required for MPPC characterization. Upon further evaluation, after implementing the lower noise light diode driver system, it appears that improving the grounding on the MPPC readout board should allow for direct measurement of MPPC without the additional amplifier.

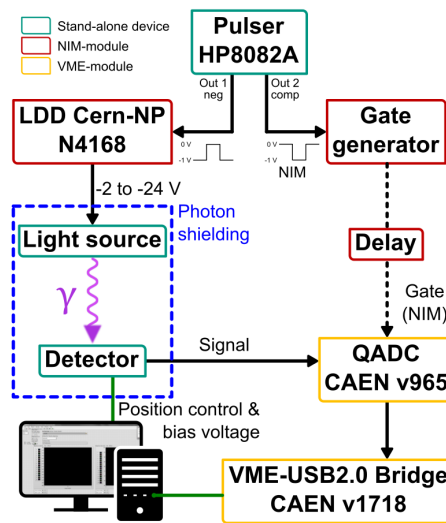


Figure 2.5: Block diagram for operation of SPOCK[41]

## 2.2.2 Characteristic Parameters for SiPM

The measurement of the charge spectrum from illuminated SiPM when properly biased into Geiger avalanche operation results in characteristic ‘finger spectra’ as shown in Figure 2.6. We measure the discrete nature of the incident photon resulting in a electron excitation and acceleration in a single GAPD. Through secondary scattering, a cascade of measurable charge is collected. The resulting charge of a single GAPD photon collection is discrete allowing for macroscopic sensors to be constructed of parallel GAPDs and the resulting finger spectra contains sharp peaks corresponding to the number of GAPDs activated. From measurements of the resulting finger spectra under different conditions, we can fully characterize the SiPM. Gain is determined by the separation of two peaks. Breakdown voltage is to close approximation given by the bias voltage resulting in zero gain by extrapolation of a linear fit of gain as a function of bias voltage. Dark count rate can be measured simply by recording a spectra without illumination. Cross talk between GAPDs can be estimated by the spectra when single photons per pulse are emitted, correcting for the dark count rate, then any counts in the spectra corresponding to more than one PE must be the result of cross-talk. The PDE can be determined by the Poisson nature of the finger spectrum and comparing the number of events in the 0 PE pedestal for illuminated and non-illuminated measurements.

<sup>9</sup>Charge Analog to Digital Converter, CAEN v965

The calibration tests follow the methodology detailed in [7] and [41] applying the results to flat field the combined four S13361s arrays. In addition to the measurements carried out at room temperature, the solid state nature of SiPM makes them inherently temperature dependent. Measurement of this dependence and the impact on the other characteristics must be taken into account for devices designed for use outside the controlled laboratory environment. For the development of SiECA, the most relevant characteristics are the gain, and its dependence on temperature and biasing voltage, the breakdown voltage, and the PDE. While important, the other characteristic quantities are of less significance in the intended cosmic ray search and, due to time constraints on development, have been left as areas of continuing work to be better assessed in the future.

## 2.3 Measurement of SiPM arrays in SPOCK

This section details the application of the measurement and analysis described in [7]. The two SiECA constructions required a total of eight S13361 arrays to be calibrated. This resulted in three calibration evaluations: once for the MPPCs flown and lost on the EUSO-SPB1 mission, once before the test deployment in HEAT<sup>10</sup> and once after returning from Argentina. The first two measurements focused on the characterization of the gain and its dependence on bias voltage. To this end, more measurements were made with finer bias voltage scanning but reduced duration which degraded the accuracy of the PDE measurement. Furthermore, the collimator ratio and photons per pulse were not rigorously monitored and recorded in the first two evaluations further degrading the PDE measurement. While this appears negligent in hindsight, the rushed pace this camera was developed under, and the expectation that flat fielding the camera on sensor gain was sufficient resulted in a few regrettable missteps. During development the concern was singularly on the production of a stable system that would perform at stratospheric altitudes. Considerations taken after this goal was achieved in hindsight, specifically the impact of flat fielding and proper calibration for expected measurement conditions, are presented here in an honest attempt to prevent such issues in the future. The flat fielding impact was better understood for gain at the time of development so logically we expected to correct for PDE variations in analysis. Explanation and assessment of the impacts of flat fielding on PDE rather than gain will be addressed in the following chapter, along with the resulting camera calibrations generated from the individual channel characterization detailed here.

### 2.3.1 Single Channel Characterization Theory

Figure 2.6 was generated with 70k pulses and each peak was fit with the function 2.1 for  $A_{peak}$  the amplitude,  $\sigma$  the standard deviation,  $x$  the QADC channel number and  $x_{peak}$  the peak average QADC channel. Peak fitting is carried out by a python script which assesses the finger spectra histogram, looks for regions which exceed the background by a user determined factor, and selectively process through the spectrum. From the determined  $x_{peak}$  channels,  $x_0$  for the pedestal,  $x_1$  for the first PE peak, up to  $x_n$ , we apply the average separation formula 2.2 for indices  $i, j$  corresponding to the  $i^{th}, j^{th}$  PE peak. The sensor gain in QADC channels,  $G_c$ , can be converted to photo sensor gain through the proportionality in formula 2.3 where  $k$  is the QADC channel to charge from calibration in [41],  $e$  the electron charge and  $A$  the amplification of any intermediary electronics such as the C12332-01 amplifier for MPPC measurement.

---

<sup>10</sup>High Elevation Auger Telescopes

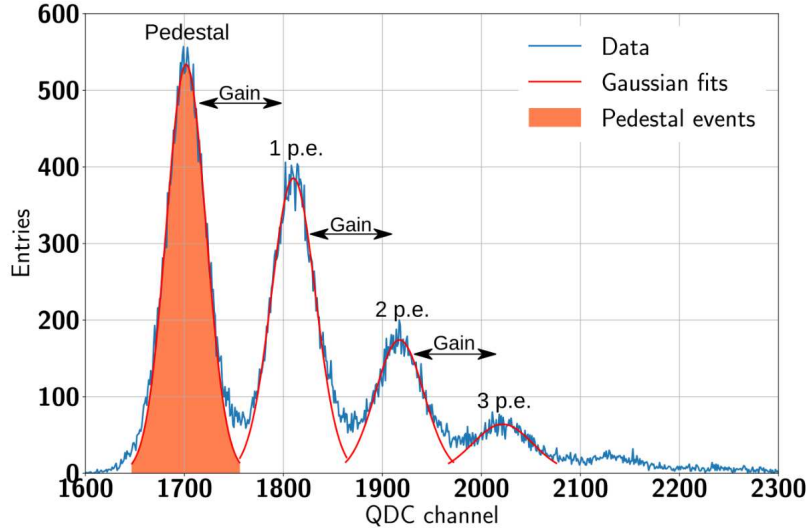


Figure 2.6: Example finger spectra with Gaussian fit PE peaks for S13 series MPPC [7]

$$f(x) = \frac{A_{peak}}{\sqrt{2\pi}\sigma} e^{-2\left(\frac{x-x_{peak}}{2\sigma}\right)^2} \quad (2.1) \quad G_c = \frac{1}{n} \sum_{i,j \ni i < j} \frac{x_j - x_i}{j - i} \quad (2.2) \quad G = \frac{G_c k}{eA} \quad (2.3)$$

From this single illuminated finger spectra, we can determine the gain at the set bias voltage. Individually, this is useful in determining the point uniformity of multi channel sensors, however, measurement at multiple bias voltages provides the necessary information to determine the gain dependence on bias voltage and breakdown voltage. The breakdown voltage,  $V_{br}$ , can be determined approximately by extrapolation to the zero gain intercept of a linear fit to the gain,  $G$ , as a function of  $V_{bias} = V_{br} + V_{over}$ . The determination of the slope  $\Delta G = \frac{dGain}{dV_{over}}$  can be used to flat field the camera by slightly varying the  $V_{bias}$  provided to each channel such that all channels exhibit the same gain. More on this follows in the Calibration chapter.

The measurement of channel gain is sufficient to determine the waveform when a cascade occurs, whether from an incident photon or thermally excited electron, however, the probability of a photon generating a signal is more difficult to assess. The PDE of a device is theoretically the product of the quantum efficiency of the silicon to create an electron-hole pair when struck by a photon, the geometric fill factor or ratio of active sensitive area to total area of detector and the Geiger efficiency corresponding to the likelihood of an electron-hole pair to initiate a charge cascade.

The components of this expression for the PDE are inherently hard to measure directly aside from the geometric fill factor which is set by the GAPD number and arrangement. Thermal excitations, after pulsing, cross talk and internal reflection all skew the direct measurement of the PDE however, by an application of Poisson statistics and comparing the pedestal count rate with the PE peak count rate for illuminated and non-illuminated measurements, we can calculate the PDE reliably [65].

$$PDE = \frac{N_{PE}}{N} \quad (2.4) \quad P_{N_{PE}}(0) = e^{-N_{PE}} = \frac{N_{ped}}{N_{tot}} \implies N_{PE} = \ln\left(\frac{N_{ped}^{dark}}{N_{tot}^{dark}}\right) - \ln\left(\frac{N_{ped}}{N_{tot}}\right) \quad (2.5)$$

Wherein  $P_{N_{PE}}(0)$  is the probability of zero photoelectrons being detected during a measurement, illuminated or dark. This probability is experimentally given by the number of events in the pedestal divided by the total number of events,  $N_{ped}^{dark} / N_{tot}^{dark}$  for non illuminated events

and  $N_{ped}/N_{tot}$  for illuminated events. Taking the difference between the natural logarithms of the probabilities of a measurement being in the pedestal provides the number of photoelectrons generated, on average, for a measurement. The logic behind this method is simple, using the dark measurement we determine the probability of a dark count contributing to the number of PEs generated. Then the measurement with light gives the number of PEs generated by subtraction. The Poisson nature of the PE distribution is key in relating the number of events in the pedestal to the number of PEs generated. Given the expression for  $N_{PE}$ , we need only the number of photons emitted each pulse,  $N$ , to calculate the PDE.

$$N = \frac{I_{PD} \cdot k_{col} \cdot k_{geom}}{E_{\lambda} \cdot f_{pulse}} \implies \frac{I_{PD} \cdot k_{col} \cdot k_{geom} \cdot \lambda}{h \cdot c \cdot f_{pulse}} \quad (2.6)$$

Equation 2.6 gives the average number of photons per pulse. For measurement systems arranged similarly to Figure 2.5 then each pulse will correspond to a measurement. If this is not the case, an additional factor must be introduced for the duty cycle ratio between the pulsed light and QADC operation.  $I_{PD}$  is the light intensity measurement of PD-A which when multiplied by  $k_{col}$ , the collimator ratio, gives the average light intensity emitted to the photo sensor. In measurement setups with the sensor at distances such that the solid angle of the collimator output is larger than the sensitive area,  $k_{geom}$  is required to correct for the portion of photons incident on the sensor. For all characterization measurements presented here the MPPC channels were within 2 mm of the collimator exit, thus,  $k_{geom}$  is taken to be 1. The energy of the photon converts the emitted average energy into the number of photons emitted. Since this is an average, it can be fractional despite the discrete nature of approximately mono-chromatic light [41]. Finally,  $f$  is the pulsar frequency. Care must be taken that this frequency does not exceed the QADC readout speed.

### 2.3.2 Measurement Method

With the described setup of SPOCK, measurement of the MPPC channels is semi-automated. At the start of each measurement PD-A and PD-B<sup>11</sup> are zeroed with the Ophir StarLab program. For stability, the photodiodes were left on and active even when not in use as power cycling the readout electronics leads to instability that manifests as both short term ( $\leq 30$  min) and long term (up to three hours from start) variation. After 12 h active time, both forms of instability are absent. Measurement of the collimator ratio is done with constant illumination from multiple LEDs, as described in [41]. At least 15 min of warm-up time is necessary for the aluminum LED array and LEDs to reach thermal equilibrium. The final calibration measurements of the SiECA S13361 arrays were performed at  $20.0_{-0.7}^{+1.3}$  °C with a pulse frequency of 10 kHz and a gate window of 100 ns. Light intensity was set to generate  $(3.5 \pm 0.3)$  photon pulses based on the measured collimator ratio at the start of measurement. Measurement of the ( $k_{col}$ ) requires alignment of the integrating sphere and collimator such that emitted light is directly incident on PD-B. The Ophir StarLab measurement software is then used to measure the ratio of the intensities between the two sensors,  $k_{col} = PD-B/PD-A$ . Multiple LEDs in continuous mode are necessary to have enough light intensity for PD-B to be within its linear range. The resulting  $k_{col}$  values are approximately  $4.00 \times 10^{-6}$  for the collimator used in calibration measurements and LEDs for both the array and pulsed source are  $(423 \pm 8)$  nm [41]. As described above, the pulsed source was connected using a secondary housing to isolate the LED driver noise from the sensor. The modified LED array was fitted with a

<sup>11</sup>Photodiode at collimator for measuring Collimator Ratio

optical fiber bulkhead compatible with the fiber, FO-M93<sup>12</sup>, allowing the pulsed LED and enclosing aluminum housing to be placed well away from the MPPC board and sensor.

After measuring the collimator ratio, disconnecting the multi-LED array and attaching the modified array with the fiber coupling, the integrating sphere is moved by manual input to the developed LabView program controlling the linear transition stages and aligned with the channel to be measured. A  $(1.0 \pm 0.2)$  mm gap is left between the surface of the collimator and the MPPC protective window to minimize the risk of scratching the sensor surface. This distance also allows some spread of the photon signal so the probability of multiple photons arriving in the same GAPD is reduced. Separation distance between the collimator and the MPPC also reduces the probability of photons arriving in the non-sensitive TSV. A balance must be maintained between measurements between two effects: Collimator too close to the sensor leads to multiple photons in the same GAPD, Collimator too far from the sensor leads to photons hitting neighboring MPPC channels. So long as the distance from the collimator keeps the solid angle spread within the bounds of one channel,  $k_{geom} = 1$ .

Gate timing is provided by the WS-2012<sup>13</sup> with a pull up ( $-1$  V baseline,  $0$  V peak of  $100$  ns width) provided to the LDD<sup>14</sup> with an Arduino driven, LabView controlled interrupt switch for making dark measurements. A synchronized complement pull down signal, meaning the  $100$  ns pulses are generated at the same time and same amplitude but opposite polarity, is sent through a delay module to the QADC to act as the measurement window. The delay on the QADC path is necessary to correctly capture the MAPMT or MPPC signal. Details on the setting of the delay and timing of the LED pulse can be found in [41]. We have replaced the HP8082A pulser due to added stability of the digital generation with the newer WS-2012. While narrower pulses could be generated with the HP8082A, leading to better timing resolution, the frequency drift was significant over extended measurements. I do not have statistical measurement of this, however, in cursory tests drift by upwards of several percent for  $10$  kHz signals was evident over less than three hours. For stability, the pulsed light source should be allowed to warm up and stabilize, similar to the continuous light array, for about  $15$  min and adjusted according to the  $k_{col}$ . Measurement of the current MPPC arrays was performed without illumination and with  $(3.5 \pm 0.3)$  photons/pulse, at  $10$  kHz for  $50,000$  measurements with biasing voltages  $53$  to  $56$  V in  $0.1$  V steps.

## 2.4 Results of Single Channel Measurement

Through measurement of each channel by the method described above and using the single channel read-out board with the C12332-01 operating as a pre-amplifier for the QADC, accurate characterization of the four 64-channel MPPC arrays was carried out. The resulting measurements and calculations of key operational parameters for these sensors show the relative uniformity of the devices both on a channel by channel and when comparing one array to another. From these measurements we can correct the uniformity of the final focal surface through bias voltage modulation or in post-measurement calculations, as will be further explored in the next chapter titled Calibration.

From Figures 2.7, 2.8, 2.9, and 2.10, we can conclude that the deviation between channels for each array is sufficiently small to allow biasing with a single primary voltage and correcting for the small inhomogeneities with the Citiroc input zero-offset DAC. As expected, channels with a higher  $V_{br}$  have lower gain than those with a lower  $V_{br}$  as the biasing potential is given by the over voltage  $V_{ov} = V_{bias} - V_{br}$ . Thus, to create a uniform sensor array, correction for the variation in  $V_{br}$  allows for direct tuning of the gain. This relation between

<sup>12</sup>Shielded optical fiber Thorlabs M93L01, 300 to 1200 nm

<sup>13</sup>Teledyne Lecroy WaveStation 2012 arbitrary waveform generator

<sup>14</sup>CERN-NP N4168 Light Diode Driver

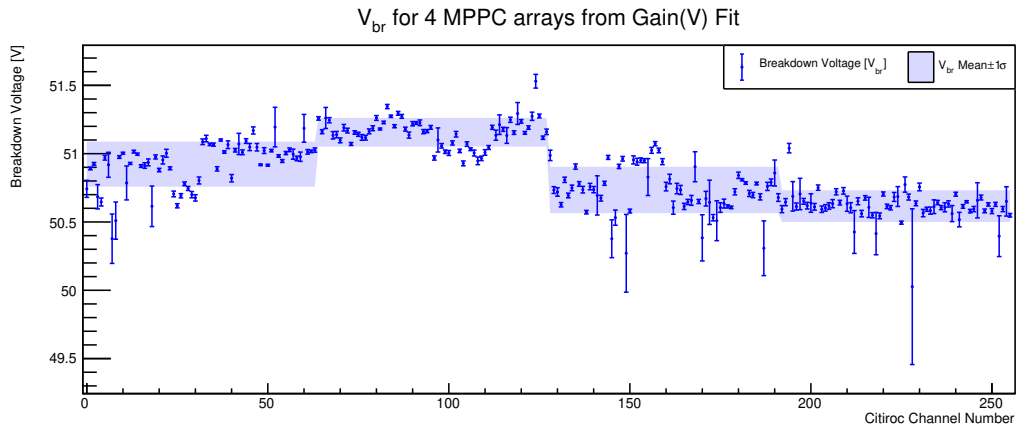


**Figure 2.7:** Breakdown voltage uniformity of S13361s arrays used in the second SiECA construction. Channel number is reflective of the SiECA architecture and can be sub divided into the four arrays in each SiECA construction. Hamamatsu specifies  $V_{br}$  for the S13361 to be  $(53 \pm 5)$  V [6]

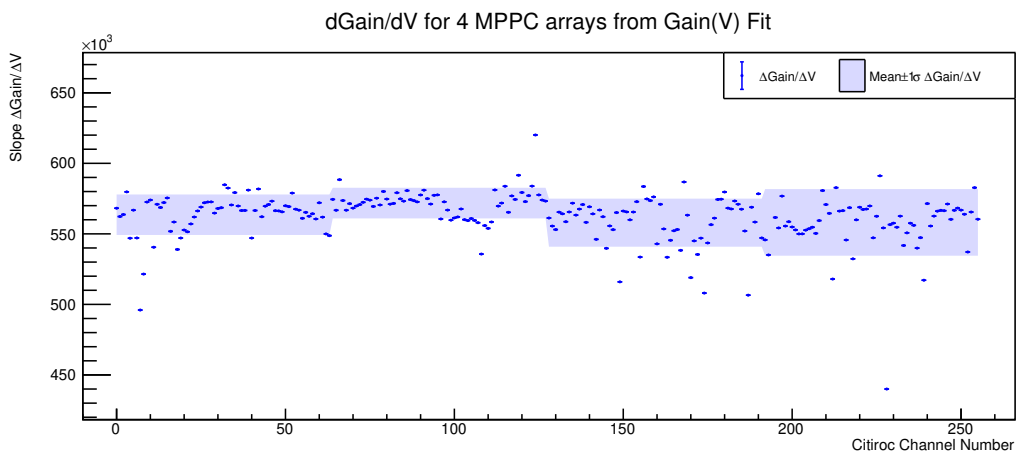


**Figure 2.8:** Slope ( $\Delta G$ ) of linear fit for gain as a function of over voltage of S13361s arrays used in the second SiECA construction

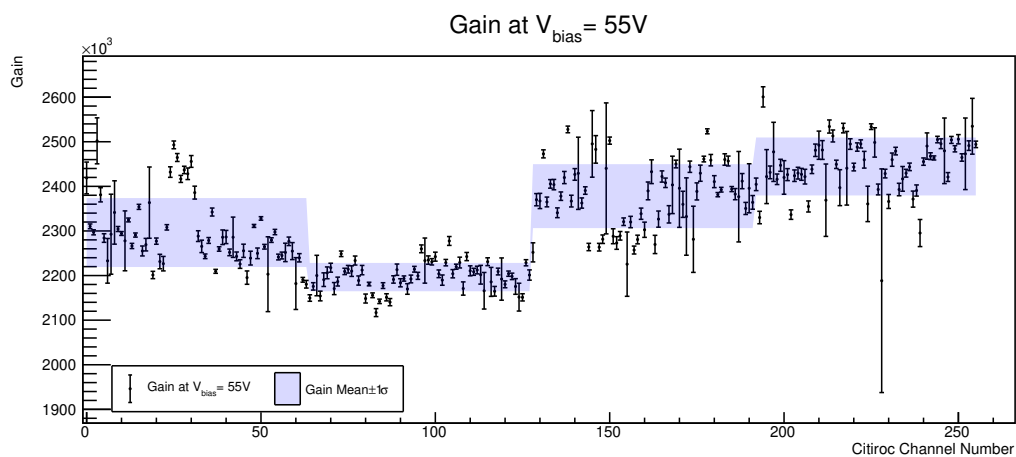


**Figure 2.9:** Gain at nominal  $V_{bias}$  of 55 V S13361s arrays used in the second SiECA construction

gain and over voltage is characterized by the linear fit value  $dGain/dV$  shown in Figure

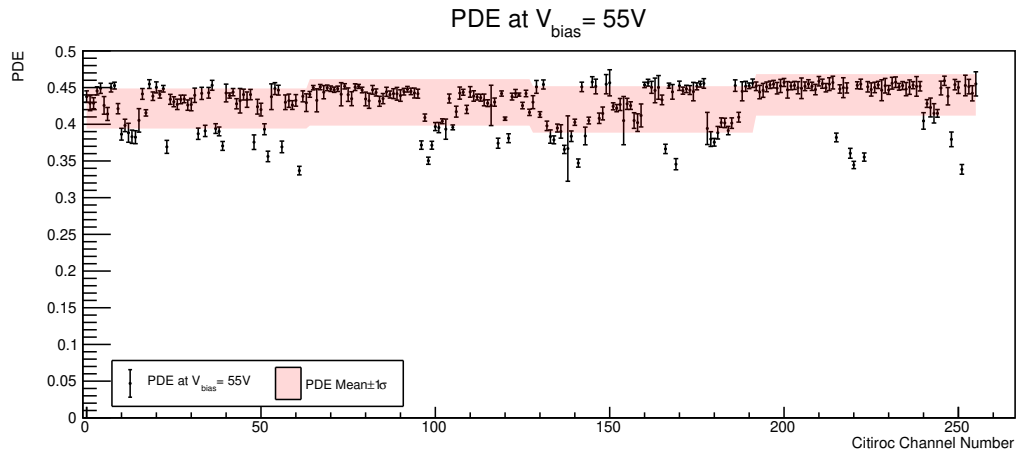


**Figure 2.10:** PDE at nominal  $V_{bias}$  of 55 V S13361s arrays used in the second SiECA construction

2.8. Error is assessed based on the linear fit and variation is clearly driven by variation in channel manufacturing.

Flat fielding in the next chapter will take this method one step further with setting the  $V_{bias}$  in each C11204-02 in SiECA to minimize the Citiroc correction while maintaining uniformity in gain or PDE. Arguments for the choice between gain and PDE flat fielding approaches will also be presented.



---

---

## CHAPTER 3

---

# SiECA Design and Construction

The SiECA camera is an implementation of current technology for the study of hardware issues that are yet unresolved for future developments utilizing SiPM for low light imaging detectors. Despite two less than optimal deployment tests, on-board EUSO-SPB1 and subsequent test attempt at the Pierre Auger Observatory, significant advancement has been made with respect to the hardware implementation. This chapter is devoted to fully detailing the hardware in SiECA and the significant design characteristics that were necessary in the creation of a working detector.

### 3.1 SiECA Mechanical Design

The physical arrangement of the sensors is well established by the EUSO PDM construction. The necessary space allotment for the bias voltage generation, MPPC sensor connection, thermal sensors, ASIC, FPGA, supply voltage regulation, USB<sup>1</sup> and LVDS<sup>2</sup> interface chips have been determined based on the sensor placement and attempting to follow the PDM structure closely. Original designs required several boards in a stacked configuration, similar to the MAPMT design shown in Figure 2.1 or layered, where the readout boards are perpendicular to the focal surface, but including additional boards replacing the ASIC and PDM boards with smaller versions for the single EC. These designs were complicated and required expensive manufacturing methods such as kapton cabling but retained the form factor of the MAPMT EC. Due to the short development period cumulating in the EUSO-SPB1 launch, a simpler design was adopted utilizing an elongated Si-EC<sup>3</sup> board holding the sensors and connected, via QRF8<sup>4</sup>(Si-EC) and QRM8<sup>5</sup>(DAQ<sup>6</sup> & Mezz<sup>7</sup>) connectors, to the readout boards oriented perpendicular behind the Si-EC board. The boards are mechanically supported by rigid frames, originally in aluminum but rebuilt with 3D printed plastic components for electrical isolation and minimal production costs and time. Electronic isolation through the addition of an aluminum enclosure was implemented after the EUSO-SPB1 flight when seemingly correlated electronic noise from SiECA interfered with one MAPMT leading to

---

<sup>1</sup>Universal Serial Bus

<sup>2</sup>Low Voltage Differential Signal

<sup>3</sup>Sensor PCB of SiECA

<sup>4</sup>Samtec QRF8-078-05.0-L-D-A-GP

<sup>5</sup>Samtec QRM8-078-01-L-RA-GP

<sup>6</sup>Data Acquisition main board of SiECA

<sup>7</sup>Mezzanine auxiliary ASIC board of SiECA

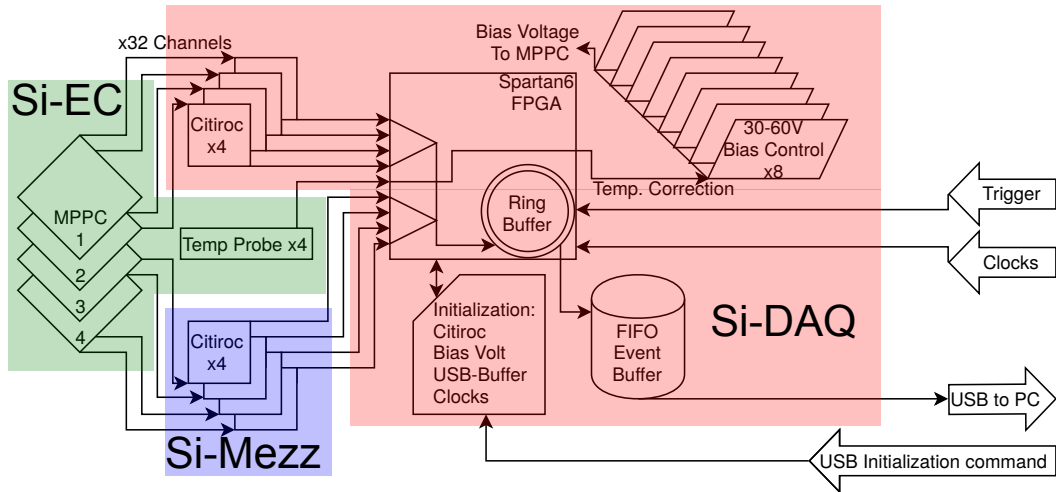


Figure 3.1: Block diagram for SiECA functionality

EC level noise during operation. The following sections detail the layout and mechanical aspects of each board, the framing structure and electronic isolation elements implemented in the final SiECA construction.

### 3.1.1 PCB, Frame, and Shielding

Within this technical description, highlighted aspects will be shown while complete schematics are included in the technical drawings in Appendix A.



Figure 3.2: SiECA Assembled

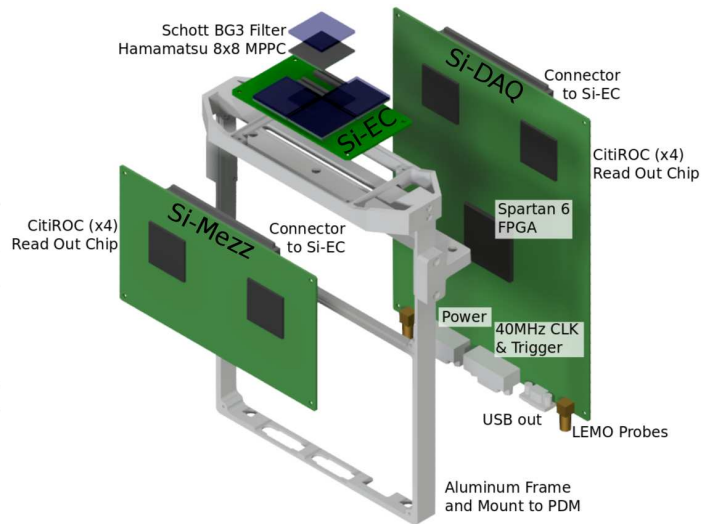
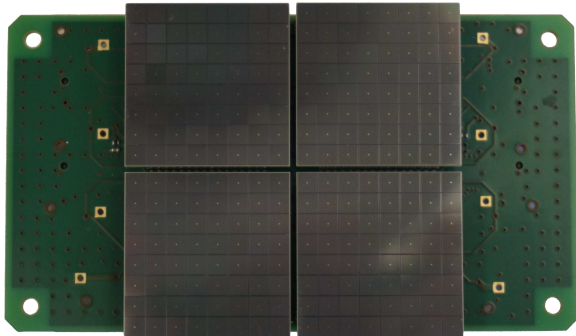


Figure 3.3: SiECA Exploded

#### Si-EC board

The Si-EC board is 90.6 mm  $\times$  50.6 mm  $\times$  1.6 mm and consists of eight conductive layers, four for bias voltages and signals and four for isolating ground planes for reduced crosstalk between signal traces. Four M2.5 mounting holes are located in the corners for securing the Si-EC board to the support structure to prevent mechanical loading of the electrical connectors. This board connects the four S13361 arrays, distributes bias voltages and collects

measurement signals from each MPPC channel. Additionally, four temperature sensors located between the corners of neighboring MPPC arrays monitor and report the operating temperature of the sensors to the FPGA. While not implemented in the EUSO-SPB1 or Pierre Auger Observatory HEAT deployments, these temperature sensors could be used to regulate the bias voltage generators to maintain constant internal gain of the sensors.



**Figure 3.4:** Final Si-EC board with four S13361 arrays. Temperature sensors are obscured by arrays but are also on this side

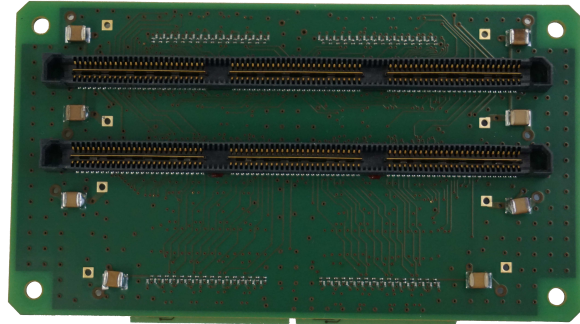


**Figure 3.5:** Back of Si-EC board with connectors to DAQ and Mezz boards and biasing capacitors and resistors

The Si-EC board connects perpendicularly to the readout boards so as to minimize the occupied area parallel to the focal surface and to be similar in structure to the PDM. Placement of the QRF8 connectors on the Si-EC board are spaced dictated by the ERM8<sup>8</sup> and ERF8<sup>9</sup> stack height corresponding to alignment between the SS4-40<sup>10</sup> connectors to allow via-in-pad PCB construction where necessary. Furthermore, the QRF8 connectors are offset from center such that SiECA can be oriented with a larger overlap of the host camera's support structure. This overlap allowed for the SiECA focal surface to be as close as possible to the EUSO-SPB1 PDM edge without obstructing the insulation and heating element around the periphery of the PDM.

### Mezzanine Board

The 91 mm × 150 mm Mezzanine board houses four of the Citiroc ASICs and all the passive components necessary for processing half of the MPPC signals generated on the Si-EC board. The Mezz board connects to the front board via the aforementioned QRM8. The layout of the Mezz is copied from the DAQ board however the MPPC bias and temperature sensor traces have been omitted on the Mezz board. Connection to the DAQ for initialization and measurement signal transmission is made via the ERF8/ERM8 connector pairs located behind and outward from the ASICs. The attached copper plate over the analog signal inputs to the ASIC serve to isolate the signal traces from amplified feedback or noise collected on the external shielding.

### DAQ Board

The DAQ board is the core of SiECA. From the front, at the QRM8 connector, we have 64 MPPC channels being distributed, on either side of the board, to the two 32 channel Citiroc ASICs, the small central chip is the ADC<sup>11</sup> for converting the temperature sensor measure-

<sup>8</sup>Samtec ERM8-060-05.0-L-DV-TR

<sup>9</sup>Samtec ERF8-060-07.0-L-DV-TR

<sup>10</sup>Samtec SS4-40-3.00-L-D array receptacle

<sup>11</sup>Analog to Digital Converter



Figure 3.6: Mezz board top side



Figure 3.7: Mezz board bottom side

ments to digital values for the FPGA. The large, central chip is the Spartan6 FPGA which controls initialization, trigger counting, event packet generation and packet distribution to the USB interface. More on the FPGA operation will be discussed in the Signal Processing section.

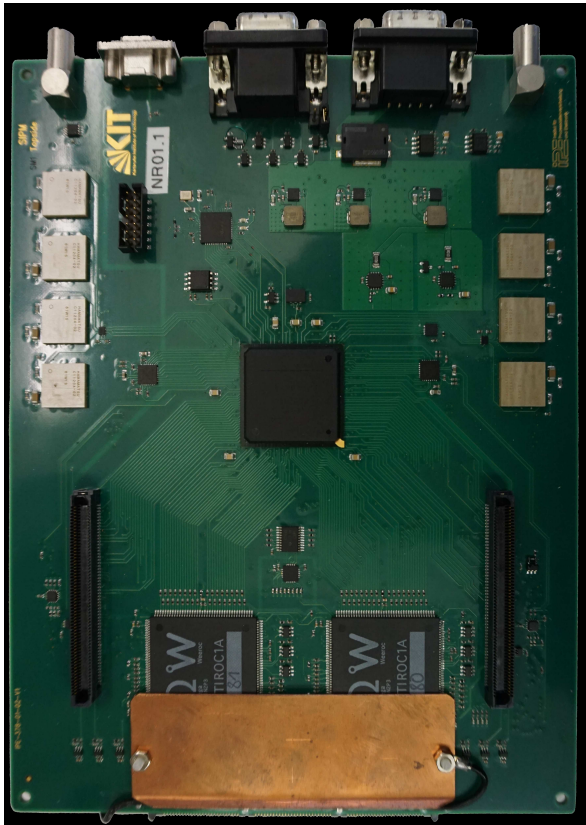


Figure 3.8: DAQ board top side



Figure 3.9: DAQ board bottom side

Rearward from the FPGA are the eight C11204-02 bias power supplies for the MPPC sensors along with various digital and analog chips for proper voltage regulation and generation, clock/trigger management, probe management and the USB interface. Finally, at the back end of the DAC board are the electrical interface connectors comprising two LEMO-00 probe (digital and analog respectively), the mini-USB data connection, the D-Sub9 5 V/2 A connector and the mini-D-Sub15 LVDS clock and trigger connector. These connectors ex-

tend beyond the board dimensions to allow access when mounted in the frame structure or shielding enclosure.

### PCB Frames and Enclosures

Mechanical support for the PCBs is provided by specially produced structural frames. Originally CNC<sup>12</sup> milled from aluminum but in later constructions made from 3D printed plastic for weight and ease of production, these structural members maintain the spacing and orientation of the PCB such that mechanical stress is alleviated from the electrical connectors. The frame structures also provide mounting points for attachment to the host telescope camera. There are two main iterations in the mechanical design. First, the EUSO-SPB1 structure was built to be as minimal as possible, given flight weight restrictions. For this, the external enclosure was not included, and the mounting arm bolted directly to the PDM frame and to SiECA via two M2.5 holes tapped into specifically thickened areas of the DAQ-Mezz frame, made from aluminum. The Si-EC frame was 3D printed from black plastic so as to minimize reflective effects for both cameras and to reduce the antenna effects of a large aluminum frame in close proximity to the sensors.

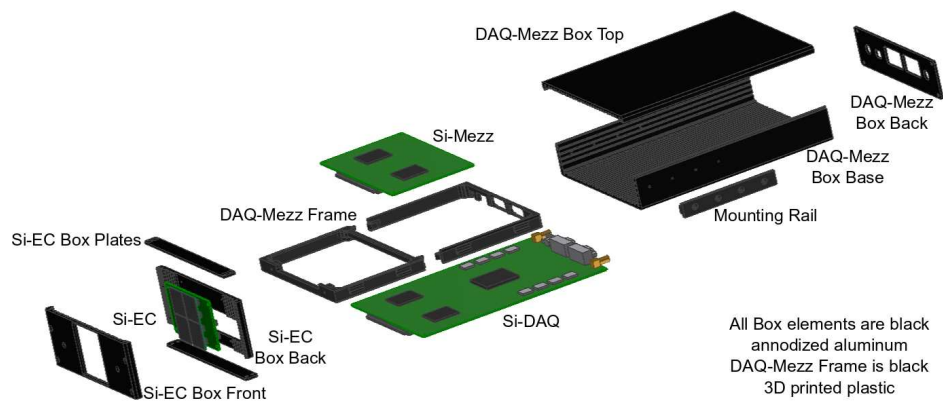


**Figure 3.10:** SiECA complete with isolating aluminum black box and mounting rail

The second produced version of SiECA utilized 3D printing for the DAQ-Mezz frame, which required the design to be halved and bolted together after printing in order to fit in the printable area of the available 3D printer. This plastic frame included rails specifically designed to slide into the internal slots of the stock aluminum box enclosure aligning the connectors with cut slots in the backing plate and QRM8 connectors with the opening in the Si-EC board enclosure and QRF8 connectors. The Si-EC frame was replaced by directly mounting the Si-EC board to the enclosure material. After connecting the Si-EC, already secured in its enclosure, to the DAQ and Mezz boards, secured with two bolts, the two enclosures are directly secured with an additional four bolts providing a structurally rigid frame that both isolates the camera from electronic and physical damage. The extruded aluminum forms are KO HL 0 for the Si-EC enclosure and KO HL 0 and K0 HL 4 for the DAQ/Mezz enclosure with black anodized finish.

### 3.1.2 Sensor-Filter Gluing

Much of the work to understand the filter glass to MPPC gluing process was undertaken by an Erasmus student, Alberto Bertone, from Turino. As it is not previously published, I will be citing him by conversation for his significant contribution to this development [61].

<sup>12</sup>Computer Numerical Control

Like the MAPMTs, the MPPCs accept a wide band of wavelengths, however, EUSO and related missions are most interested in the wavelengths corresponding to the nitrogen fluorescence spectrum as these UV emissions are distinct and discernible from most background sources. Schott BG3 filter glass is used for the necessary bandpass filters on the MAPMTs and for consistency, we sought to use the same material for the filters on SiECA [66]. Similarly, EPO-301<sup>13</sup> is used both for the PDM and SiECA to mechanically and optically couple the filter glass to the silicon window of the MPPC [67].

Unlike the MAPMT trapezoidal filters, SiECA uses simple rectangular filters, alleviating the Winston cone-like effects of collecting light from the areas between MAPMTs into the edge channels. This simplification in design also simplifies the gluing apparatus, which was 3D printed and deemed to be of sufficient accuracy for the limited number (four) MPPCs needing filters affixed for the EUSO-SPB1 flight.

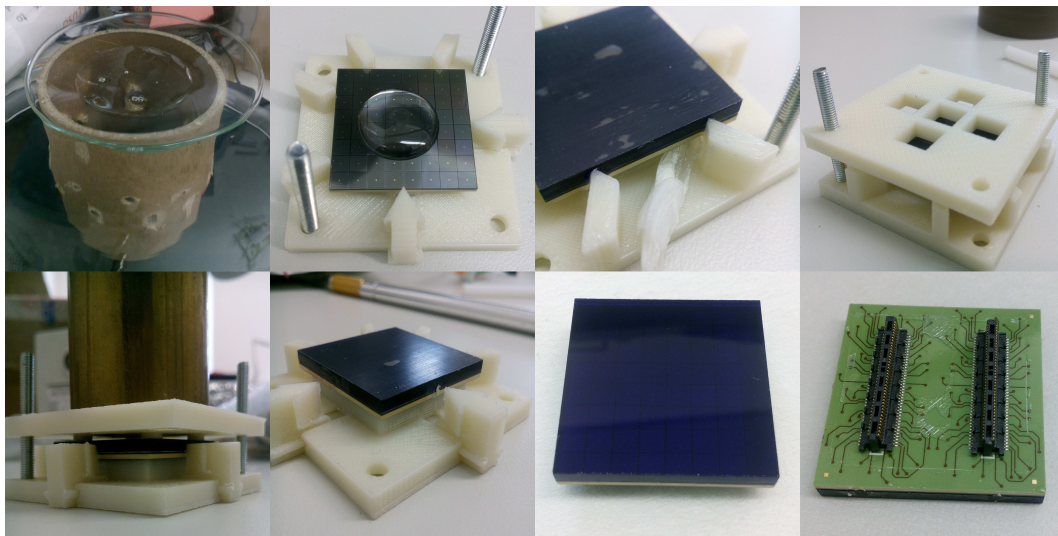


**Figure 3.11:** Left Top: Degassing epoxy, Epoxy on MPPC in jig, Taped filter placed with excess epoxy wicked off, Compression plate added. Left Bottom: Compression for 24 hours, Removing movable blades, Tape removed, Excess epoxy does not interfere with electrical connectivity

The gluing process is adapted from that used for the MAPMTs at Riken, Japan. Given the simplified geometry, alignment is much simpler and can be achieved with vertical, blade like protrusions which minimize epoxy contact cementing the MPPC-filter assembly to the alignment jig. With four contact blades along two sides forming the fixed corner of the jig, and two movable blades positioned independently, the MPPC and filter are held in alignment and compressed by the top plate with securing bolts in the corners of the device. To alleviate bubble formation during curing, the mixed epoxy is off-gassed under low vacuum within a bell chamber connected to a roughing pump. Care must be taken during the chamber evacuation process to allow the bubbles to escape slowly rather than foaming the mixed epoxy leading to a partially cured, inconsistent mixture with unknown optical and mechanical properties. The vacuum procedure takes approximately one hour: 35 minutes of staged pumping to prevent epoxy foaming, 15 minutes at maximum vacuum (approximately 0.1 Pa) and 10 minutes gradual return to ambient pressure. This process is acceptable as the potting time of this epoxy is nominally eight hours [67]. Careful handling to ensure clean surfaces, placement of the filter so as not to create bubbles and minimal wicking of the excess epoxy such that the entire contact area of both pieces are optically bonded is imperative. Similar to application of a glass screen protector, introduction of bubbles to the degassed epoxy defeat

<sup>13</sup>EPO-TEK 301-2 optical 2 part epoxy resin

the purpose however, micro-bubbles can still form during curing. These micro-bubbles are of little concern as they are substantially smaller than each MPPC channel, thus, induced scattering is of negligible consequence. Further study can be undertaken on this point but has not been at this time.

### 3.1.3 Attachment to Host Camera

As an ancillary or add-on camera, SiECA is meant to be attached to a host camera, properly aligned, to provide an extension to the focal surface in an area that the telescope optics focus light but is not measured by the main camera. This was possible both in the EUSO-SPB1 and HEAT telescopes as the optics create a circular focus but the main camera element is effectively square, leaving the area between the edge of the PDM EUSO-SPB1 and eye-frame HEAT open for SiECA. The mounting hardware for these two different arrangements required substantially different approaches with regards to available bolt holes, clearance and operation orientation. Schematics for both are included in Appendix A.

#### Mounting Brackets for SiECA on EUSO-SPB1

Two versions of the mounting bracket for attaching SiECA to the PDM: Bracket1 mounts SiECA so the corner of the BG3 filters closest to the PDM BG3 filters is 1 mm laterally separated. This bracket also tilts SiECA to maintain the 2.5 m concavity of the PDM focal surface.

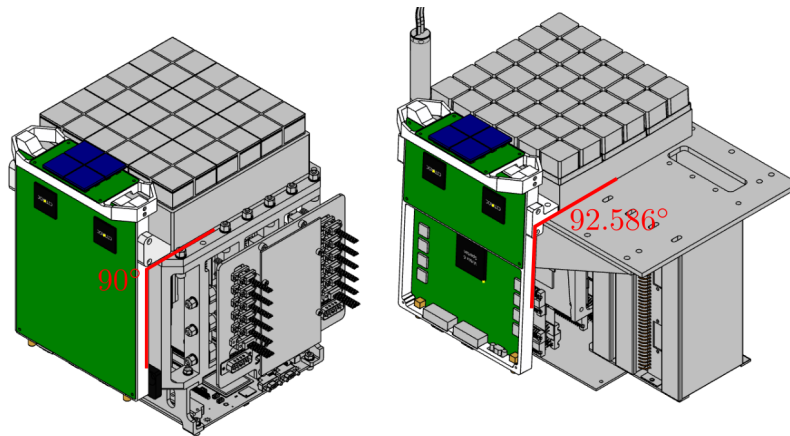


**Figure 3.12:** SiECA to PDM mounting brackets. Left: EUSO-SPB1 PDM, flat focal surface. Right: EUSO-Balloon curved focal surface with correction in bracket to align SiECA with curvature

Due to complexity of design, this curvature was abandoned for the EUSO-SPB1 PDM in favor of the simpler flat focal surface. Defocussing at the edge (where the affect should be maximal) was determined to be substantially less than one pixel and thus of negligible impact to the end measurements [56]. The Bracket2 design accepts the simpler PDM design and maintains flatness across both detectors. An argument could be made that the GAPD layer should be aligned with the photo-cathode of the MAPMTs however alignment of the filter surfaces was more practical. Three versions of Bracket2 were produced by 3D printing to allow for the PDM heating element to be insulated between the readout boards of SiECA and the PDM. Thus, the flight spacing between the two detectors is greater than the ideal 1 mm similar to that of the ECs within the PDM.

### Mounting Clamps for SiECA on HEAT

The machined aluminum PMT frame in HEAT does not have the convenience of additional mounting points so a custom clamp system was designed and 3D printed. Black plastic was used so as not to add reflective materials within the telescope. The design consists of two clamps, two 'L' shaped arms, two jaws and two rails. The clamps mechanically hold onto the PMT frame. The L-arms bolt to the clamps and jaws allowing for two degrees of movement, parallel to the PMT frame edge and perpendicular to it. The jaws are held onto the L-arms by a bolt and, when tightened, hold the rails connected to the outside of the aluminum shielding enclosure. The length of the rails allows for radial adjustment with respect to the curvature of the PMT frame. These three degrees of movement allow SiECA to be positioned close to the Mercedes stars of the edge PMTs with the correct angular orientation and depth of focal surface. Due to a modification to allow the L arms to sit closer to the PMT frame, the printed clamps were not strong enough to hold the camera and had to be supplemented with commercial clamps. Full schematics are included in Appendix A.

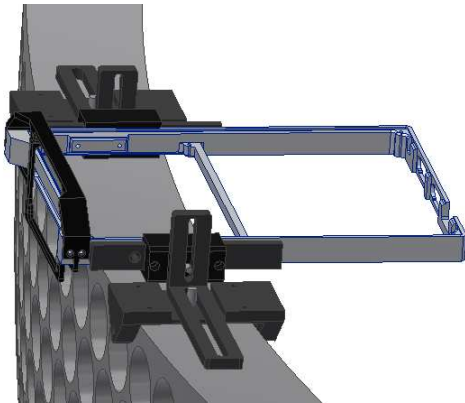


Figure 3.13: HEAT mounting system

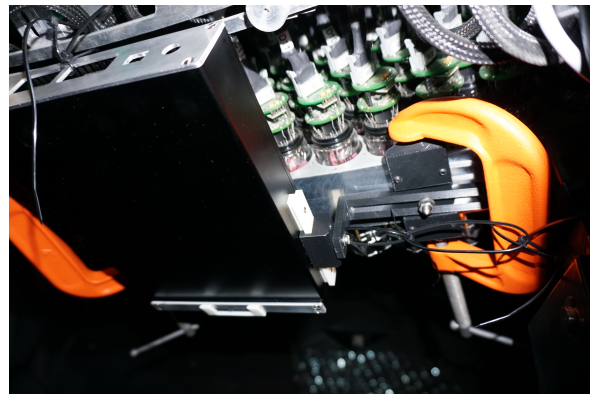


Figure 3.14: SiECA attached to HEAT

## 3.2 SiECA Electrical Design

The mechanical design of SiECA is driven by the electrical requirements, aside from the sensor orientation and proximity to the edge of the camera for alignment. This section will attempt to explain the layout of the SiECA Si-EC, DAQ and Mezz boards, highlighting the relevant features for subsequent developments. The DAQ and Mezz boards were designed and assembled in close cooperation with Alexander Menshikov (KIT-IPE) as well as the FPGA, ASIC, bias generator and interface programming and the initialization routines. The achievement of a working SiECA camera is completely dependent on Alexander's expert knowledge and dedication to this project.

### 3.2.1 Si-EC Board

The mechanical properties and positioning of the sensor connectors on the Si-EC board are dictated by the spacing and orientation of the MPPC. Nominally, the sensor mounting side is taken to be the top while the QRF8 side is the bottom.

The bias voltage is distributed on the top layer with  $\frac{3}{4}$  of the in-line 1 k $\Omega$  resistor and decoupling 100 pF capacitor, both in 0201 packages, while the remaining  $\frac{1}{4}$  are placed on the bottom due to space limitations. To minimize costs, through vias are used throughout

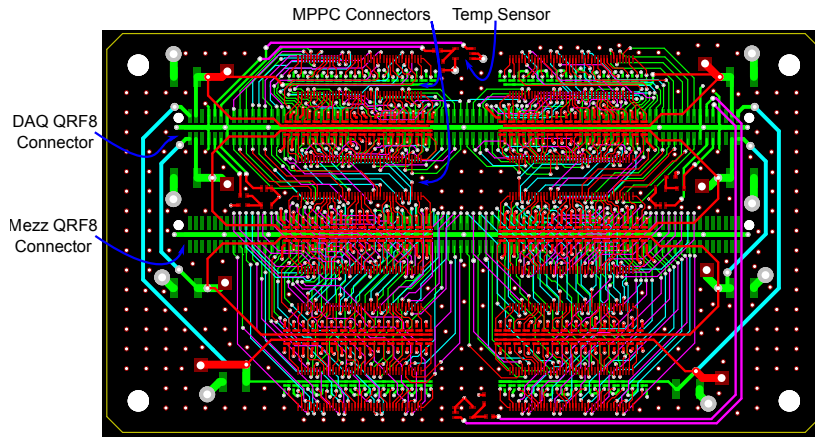


**Figure 3.15:** Schematic of Si-EC PCB routing. Eight layer board with ground plane pours on layers 2, 4, 5, and 7. Top layer (1) with traces in red, pads in dark red (sensor side). Inner trace layers (3 & 6) in cyan and purple. Bottom layer (8) with traces in bright green, pads in dark green (connectors to DAQ and Mezz boards). Yellow outline is board edge

the board. This makes getting both bias voltage and signal traces to the 0.4 mm pitch SS4-40 difficult with standard minimum 0.150 mm traces, 0.450 mm land/0.200 mm drill vias and 0.170 mm clearance. Blind vias were necessary to connect the decoupling capacitors located opposite the QRF8 to the analog ground plane. As can be seen in Appendix A, much of the area between SS4-40s is covered by either resistor and capacitor pairs or vias. The area below the connector is utilized for vias sparingly due to the open wire connection between the pad and the connector contact point. Thus, vias can only be placed in-line with their respective pad to avoid unintended connection between channels, especially for bias voltage contacts. Test points have been included for each bias voltage generator, eight total, to determine in-lab if the voltages specified in the initialization routine are correctly reaching the front board. Additionally, each bias voltage is decoupled by a 4.7  $\mu\text{F}$  capacitor with a 1210 footprint. All the passive elements are rated for 100 V even though operating bias voltages are below 60 V for the MPPC. This high voltage requirement severely limits the capacitance available in the 0201 package but larger footprint capacitors could not be placed nearly in-line with the SS4-40 pads. To unify the grounding planes, stitching vias have been added where possible. This is easiest around the outer area of the board but efforts were made to include them in the more densely traced inner areas. This could be further optimized given additional development time, however, better assessment of the noise impact on the signal quality is necessary to warrant additional grounding.

### 3.2.2 Data Acquisition and Mezzanine Boards

The eight bias voltages, tuned for the MPPC channels they supply, are generated by the eight C11204-02 chips, distinctly silver in color on the DAQ board in Figure 3.8. They are connected to the Si-EC board by the outermost eight channels (two on the top and bottom of each end) of the QRM8-QRF8 connector pair of the DAQ board. One channel on the top and bottom is left non-connected followed by the analog ground. The next two pins inward contain the 3.3 V supply and signal return connections for each of the four temperature sensors on the Si-EC board. One more non-connected pin separates the bias and temperature contacts from the MPPC signal contacts. The Mezz connection to the Si-EC board is the same as the DAQ however the Mezz connection does not carry any bias voltages or temperature signals leaving these pins non-connected.

The DAQ and Mezz boards contain the ASICs, FPGA, bias voltage generators, and interface chipsets. Incoming MPPC signals are terminated with  $50\ \Omega$  resistors and  $100\ \text{nF}$  capacitor in series to ground. Combined, the two boards contain eight Citiroc capable of analyzing 256 continuous signals from the MPPC front board and connected through the QRF8-QRM8 interface. The output of these ASICs is 256 digital trigger lines, 16 multiplexed charge read-outs (one high and one low gain per chip) [68]. The digital trigger lines are individually connected to the FPGA for trigger counting and the multiplexed lines are connected for charge measurement. The Mezz board signals are connected to the DAQ board through the ERM8-ERF8 connector pairs. These connectors also supply power, initialization and clocks to the Mezz Citiroc. More on the signal handling will be discussed in the following section.

The analog temperature measurement is run through the ADC located centrally, between the Citiroc and FPGA on the DAQ before being connected to the FPGA where averaging across two neighboring temperature sensors provides an estimated temperature for each MPPC array. This digital signal is then converted back to analog by DACs close to the bias generators. This correction was turned off during the EUSO-SPB1 and HEAT deployments as it had not been sufficiently tested for stability and reliability.

### 3.2.3 External Interfaces

The back end of the DAQ board is dedicated to external interfacing. Two LEMO Type-00 connectors are available for digital and analog probes, both controlled by command at initialization, with capabilities to examine signals such as pre-amplified MPPC channels, Citiroc digital trigger, bias generator state, and several others useful in testing and diagnosing operation issues. Power is supplied via the D-sub9<sup>14</sup> connector, the upper five pins being 5 V and the lower four being ground. SiECA was allocated a maximum current consumption of 2 A during start-up and operation. To maintain this power limit, staged initialization is utilized by starting the FPGA, then each ASIC in series, and then the bias voltage generators with minor delays between processes. Initialization remained below 1.56 A during laboratory test starts with operation consumption varying between 0.43 A when measuring and waiting for trigger but jumping to 0.96 A when reading out an event and transmitting via USB interface. Hardware level clocks and triggers are passed into SiECA via the VGA<sup>15</sup> connector. These signals are expected as LVDS but 3.3 V TTL<sup>16</sup> logic can be accepted so long as the corresponding LVDS chip is bypassed and correct pin pairs and polarity are observed.

In the current configuration, SiECA can be operated with or without any external clocks but the FPGA is configured to synchronize with a 1 PPS<sup>17</sup> and utilize a 40 MHz for GTU separation if available. Host generated, LVDS trigger signals are accepted if SiECA is initialized to accept them exclusively or in addition to software triggers and internal ring buffer offset can be set to center the event in the 128 GTU event packet based on host camera trigger latency. Event packet structure will be discussed in the following section.

A mini-USB to USB-A cable connects to the operating computer to send initialization commands and files, read system status and collect packaged events when they are made available in the USB buffer memory. This connection is processed by a FT232H<sup>18</sup> configured as a USB-FIFO<sup>19</sup> interface allowing for sequential command responses and event packets to be read out sequentially by the host telescopes operating computer. As triggering SiECA was developed to be accessibly general, a hardware and/or software flag can be generated

<sup>14</sup>D-sub-miniature electrical connectors with 9 pins

<sup>15</sup>Video Graphics Array, 15 pin 'D-sub' style used for LVDS inputs

<sup>16</sup>Transistor-Transistor Logic

<sup>17</sup>Pulse per second, GPS generated synchronization pulse

<sup>18</sup>FTDI single USB 2.0 chip used in FIFO mode with event buffer

<sup>19</sup>First In, First Out operation of the USB interface

(as specified by the run files) when an event is registered in the FIFO buffer. Alternatively, a scheduled delay in the host computer from event triggering to event readout can ensure correlation between main and ancillary camera images.

### 3.3 SiECA Signal Processing and Data Generation

This section will discuss the operation of SiECA and the signal handling and data generation. Additional information can be found in the operations guide in Appendix C.

#### 3.3.1 Initialization of System

When fully connected and powered, SiECA will automatically reload the operation settings from the previous operation period. However, without initializing the system, no triggers will be accepted and no events will be generated. These stored configurations are co-located in the EEPROM<sup>20</sup>. The timing and boot sequence of SiECA is described in the previous section. Depending on the state of the flags in *siecacommon.h* the previous bias voltages and voltage offsets will be reset from the provided configuration file. Parameters in the ASIC such as pre-amplifier gains, discriminator thresholds and fine tunings, and FPGA parameters such as event depth (number of GTUs), GTU length (adjustable but set at 2.5  $\mu$ s EUSO standard), and trigger latency are set by additional flags in *sica\_if.c* and *main.c* if they are not found in *siecacommon.h*. The *main.c* core also contains the data acquisition logic which is user defined allowing for hardware (LVDS to FPGA from host), firmware (clock cycle triggering if implemented in FPGA flash) or software (either by sent command or by system interrupt call) leaving all trigger options to the user. Of course, hardware level vial LVDS signal is the preferred method for making coincidence measurements as it removes any CPU processing time delays.

Once the system is operational and the current consumption from initializing all the on-board hardware has dropped to the stable, low level, the event ring buffer is being filled with the specified measurements from each channel every GTU. When a trigger is received, the specified number of consecutive GTU buffer bins is read out with the defined latency (number of bin delay from current to last bin in the desired event) to the FIFO for USB collection. At this time, if not triggering via software, a signal interrupt is issued from SiECA to the host computer to indicate an event is in the FIFO waiting to be read out. Depending on event depth, several events can be stacked in the FIFO, nominally 6 without noticed issue for 128 GTU deep events, however, for simplicity, it is preferred to read out events as soon as possible to prevent data loss in the event of power loss. In the following sections, discussion of the measured signal and signal processing through SiECA will be described.

#### 3.3.2 Sensor and Front Board Signal Handling

As described in the section concerning SiPM development, the MPPC used in SiECA are arrays of parallel reverse biased GAPDs. In order for an electronic signal to be generated when a photon interacts with a GAPD, the biasing voltage must be above the breakdown voltage of the GAPD. The difference between the operating voltage (delivered by the bias voltage drivers) and the breakdown voltage is the over voltage which determines the field strength within the GAPD which determines the gain of the sensor and is detectable in the total electric charge collected for a single photon-GAPD interaction. A higher over voltage creates a larger discharge when the photon triggered avalanche occurs, depositing more electrons on the anode for measurement.

---

<sup>20</sup>Electrically Erasable Programmable Read-Only Memory

To ensure constant and stable biasing voltages, each of the eight bias voltage generator traces is decoupled to ground via a 1210 package 4.7  $\mu\text{F}$  capacitor. To prevent a discharge in example channel 'A' from impacting the bias voltage in example channel 'B', each MPPC channel's individual bias line is filtered by a series 1 k $\Omega$  resistor and decoupled from ground by a 100 pF capacitor (both 0201 package). The proximity of these passive components to the MPPC channels they regulate mitigates the long trace antenna effects, however, the anode connection from the MPPC to the QRF8 connectors is less protected.

Post routing assessment shows the range of signal trace lengths span from 6 to 25 mm. Concern over the signal trace length is confined to the Si-EC board as the highly parallel distribution from QRM8 connectors to the ASICs on the DAQ and Mezz boards are uniform and with little deviation. Given the intended integration time of 2.5  $\mu\text{s}$ , the relative difference in signal arrival timing between two coincident photons is negligible. Variation in the noise impact is expected despite efforts to keep signal traces mostly within the ground plane shielding layers, this has not been assessed in this work but should be considered in future developments. Where possible, neighboring traces have been separated to different copper planes. This is impossible in areas where additional vias would block neighboring traces from reaching the necessary connector pads. Evaluation and optimization of this layout could not be performed given the production timetable.

Substantial noise was generated by the temperature sensors when operated in parallel with the MPPC. This was corrected in the FPGA firmware causing the temperature to be measured only at start-up and after an event is triggered, meaning the bias voltage was not regulated by the temperature sensors. Connection of the temperature sensors with a dedicated grounding scheme rather than using the same ground as the MPPC could reduce the impact of measurement at the same time at the cost of more complicated PCB layout.

### 3.3.3 DAQ and Mezz Digitization with Citiroc

In the design of the SiECA camera, we selected components that best embodied the operational goals of the EUSO telescope design. Consideration of several ASICs was undertaken early in the design process. The selection of the Citiroc ASIC for SiECA was based primarily on design comparability with the MAPMT ASIC, the Spaciroc3. More capable devices such as the DRS4<sup>21</sup> were eliminated from the consideration due to high power demands and low channel to footprint density [69]. In the case of the DRS4 chipset, 32 individual chips would need to be routed to support the 256 channels of SiECA simultaneously and the supporting PCB design would have been much more complicated. The ability of Citiroc to function in a peak over threshold or charge integration mode proved critical in the design of SiECA despite the charge integration readout time being far too slow for EUSO-like measurements and certainly too slow for Cerenkov events. From this selection, design of the DAQ and Mezz boards could begin. Due to the short development period, minimal testing with a Citiroc development board was undertaken to determine that the signals generated by the selected MPPC would be usable with Citiroc. This comprised one day of connecting and testing with the development board designed around a Citiroc chip. While successful in showing that the MPPC and Citiroc can work together, I have no significant measurements from this testing.

Raw MPPC channel signals from the front board connect to the DAQ and Mezz boards through the QRM8 connectors. A 50  $\Omega$  resistor and 100 nF capacitor in series terminate the signal to ground as specified in the Citiroc datasheet [68]. Each set of 32 channels, half an array divided by row A-D and E-H, have a single high voltage bias generator and Citiroc ASIC. This division allows for fine tuning both of the generated bias voltage and the individ-

<sup>21</sup>Switched Capacitor Array ASIC, 6 GSPS max, Paul Scherrer Institut

ual MPPC bias voltages through the eight bit input DAC. This DAC allows for a non-zero baseline offset voltage to be applied to each channel. Since the offset voltage is positive, the effective bias voltage  $V_{BiasEff}$  is the generated  $V_{Bias}$  minus the positive  $V_{Offset}$  resulting in the ability to flat field the detector both at the half array level and at the individual channel level. With Citiroc,  $V_{Offset}$  is maximally 2.5 V internal reference or 4.5 V external reference and each channel's offset is set in slow control. Further discussion of flat-fielding will be undertaken in the chapter on Calibration.

After the input DAC, signals are amplified with either low or high gain pre-amplifiers. These increase the voltage of the signal allowing for the shapers to properly distinguish peaks from baseline noise. Both are configurable in slow control but only the high gain pre-amp is used in SiECA. At this point the processing progresses either towards photon counting or charge measurement. Both are implemented in SiECA however the single photon counting has proven more functional as the readout time of the multiplexed charge measurement is on the order of 10  $\mu$ s per measurement. This is clearly unacceptable dead-time for a near-continuous capture device. Photon counting loses resolution on multiple incident photons at a time but the triggers are processed by the FPGA continuously so dead-time is negligible between GTUs.

Implementation of the charge measurement is not optimal for the imaging SiECA is designed to capture. Given the long readout time in Citiroc, subsequent images are insufficient to reconstruct even the timing and geometric nature of the shower, even with better energy resolution as each measured GTU is the total charge collected. The time trigger path is of more use for low flux events, when the arrival rate of photons in each sensitive channel are on the order of the reciprocal of the recharge after discharge time. Orbital telescopes for UHECR measurement expect to look for few to few hundred excess photons per GTU above background [56]. This rate is well within the photon counting regime of operation so implementation of the simplistic trigger counting should be sufficient for cosmic ray fluorescence measurement. When the triggering path is selected via the initializing slow control settings, the pre-amplified signals are passed to the fast shaper which has a peaking time of 15 ns effectively elongating the amplified pulse so the discriminator can process the peak and determine if the slow control set threshold is exceeded. When the signal peak amplitude is above threshold, a digital pulse is drawn high until the signal decreases below threshold. These digital pulses are accessible on the 32 time trigger output pins of the Citiroc chip and are connected directly to the FPGA for trigger counting.

As suggested before, counting triggers above a single threshold loses resolution between single and multiple incident photons and, thus, total light collected which, as shown in the introduction, is correlated with primary energy. This could be corrected by careful analysis of the amplified waveform, as is done in most Cerenkov telescopes, or more simply, the duration of the time over threshold as a two photon peak should be measurably wider than a single photon peak and so forth for additional photons. This calibration test has not been undertaken due to time constraints but will be further discussed in the calibration chapter.

### 3.3.4 FPGA Gate Timing, Trigger Processing and Packet Generation

The FPGA handles initialization, operation, timing, peak counting, trigger processing and event packet generation. Interaction with SiECA via the commands implemented in *sica\_if.c* generates bit interpreted packets that the FPGA reads and enacts to carry out camera operation. SiECA is designed to accept external clock signals, delivered on LVDS pairs and can be configured accordingly. In the absence of these signals, they can be internally generated with local oscillators and synchronized with the hosts GPS PPS signal. If no clocks are available, or SiECA is operating autonomously (possible with a Raspberry Pi for data

storage and communication), then the system time of the host computer will be used for time-stamping events however this is subject to processor level inaccuracy unless the network provides correction. SiECA utilizes a 40 MHz rising edge triggered clock to separate GTUs, corresponding to the EUSO standard 2.5  $\mu$ s window. After initialization, for the correct slow control settings and run routine in the C operating code, SiECA will begin writing the count of pulses above threshold for each channel, each GTU, into the ring buffer. This buffer is capable of simultaneously storing the last 1024 GTU corresponding to 2.56 ms. This measurement is continuous, overwriting the oldest bin with the newest by reference such that at any time a trigger can be received and corresponding GTU bins can be collected, wrapped with header and footer information, and pushed to the FIFO buffer.

---

---

# CHAPTER 4

---

## Camera Calibration

### 4.1 Camera Calibration

The calibration of the SiECA camera, and any multi-sensor detector, is carried out so as to minimize the post processing and artificial correction needed to extract physically relevant measurements. In the case of the PDM and SiECA, this is primarily handled by the flat fielding of the camera. Flat fielding is the process by which a set of sensors are tuned so that for an equal signal, equal responses are generated by each element. The nature of the response is dependent on the tuning, in this case, tuning for uniform gain on each sensor does not completely unify the PDE. After the description of each process, a discussion of the benefits and drawbacks of both are presented. After the calibration determination, measurements of the remaining non-uniformities are presented as well as the expected sensitivity. The remaining non-uniformity must be corrected in post processing to accurately reconstruct any measured event.

#### 4.1.1 HV and ASIC capabilities

The four array architecture of SiECA is further subdivided into upper and lower halves. Each 32 channels are supplied by a single C11204-02 and processed by a single Citiroc. This design allows for refined setting of the  $V_{bias}$  at each generator such that the correction at the ASIC input DAC is minimized for the selected flat fielding. While SiECA can be flat fielded on any of the voltage dependent parameters described in the Characterization chapter, gain and PDE are the most logical. Uniformity in gain leads to common PE charge and is useful when integrating total charge collected in a measurement window. This is the method employed by the PDM in EUSO designs. As described earlier, the charge readout time in Citiroc is on the order of 10  $\mu$ s per ASIC but can be parallelized with proper FPGA handling. This is clearly too long to be useful in the 2.5  $\mu$ s GTU binning of EUSO. Design of a faster readout system is possible, as it is implemented in the Spaciroc3 chip however this was not implemented in the Citiroc chip [63, 68]. Alternatively, flat fielding on the PDE results in a uniform probability of generating a signal for uniform illumination across the sensor. The magnitude of the PE will be slightly different between channels however for peak counting, this is sufficient so long as the trigger threshold is set based on the individual gain of each channel.

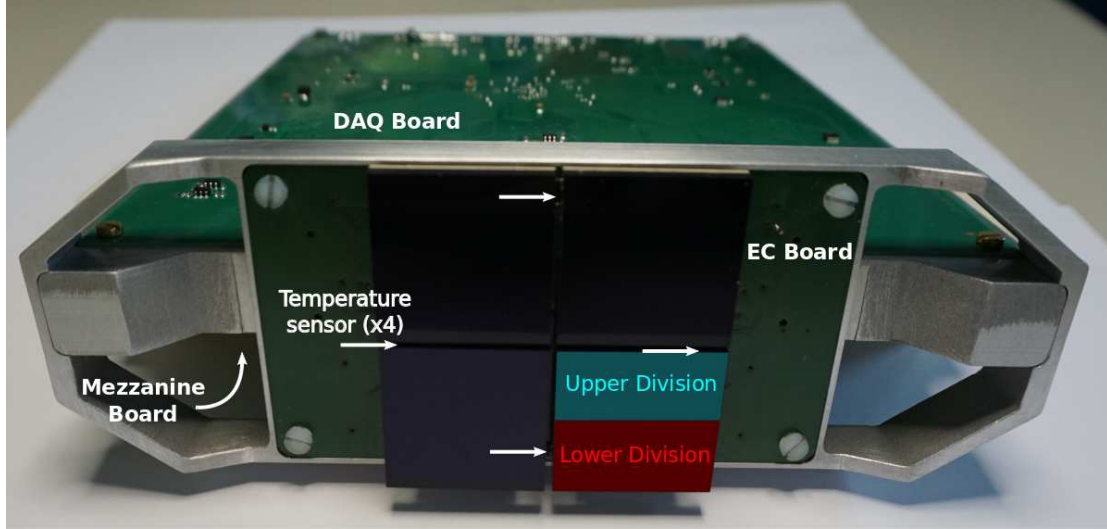


**Figure 4.1:** Subdivision of SiECA focal surface with indication of one bias generator-ASIC pair for 32 channels

### 4.1.2 Gain Flat Fielding Theory

With the generated charge of a single electron generated cascade in a GAPD being dependent on the biasing voltage, tuning of the PE charge in each channel to be uniform is a logical method for flat fielding a photomultiplier based camera. Production of S13361 has been shown in [7] and in this work to be consistent with variation in breakdown voltage at the  $(50.86 \pm 0.46)$  V level and variation in  $\frac{Gain}{V_{over}}$  at the  $(562\,864 \pm 68\,322)$  Gain/V level for four production arrays. This low deviation in breakdown voltage and  $\Delta G = dGain/dV_{ov}$  allows the correction voltage,  $V_{DAC}$ , needed on each channel to provide the  $V_{bias}$  corresponding to a uniform gain across all channels to be achievable with the 0 to 2.25 V range of the Citiroc input DACs for each channel. The resulting calculation is as follows for the  $i$ th channel:

- Determine minimum gain from all channels at  $V_{bias}$ ,  $G_{min}(V_{bias})$
- Determine voltage to achieve  $G_{min}(V_{bias})$ ,  $V_{FFbias_i} = V_{br_i} + G_{min}(V_{bias}) \cdot \Delta G_i^{-1}$
- Offset voltage to be set in Citiroc for each channel is  $V_{DAC_i} = V_{bias} - V_{FFbias_i}$

This process will determine the positive voltage offset  $V_{DAC}$  that raises the anode voltage, thus decreasing the  $V_{bias}$ . Since  $V_{br}$  is unchanged, decreasing  $V_{bias}$  is equivalent to decreasing  $V_{ov}$ . By decreasing the  $V_{ov}$  across the depletion region, the gain is reduced accordingly and when applied to all channels, results in a uniform detector with  $G_i = G_{min}(V_{bias})$ . In the construction of SiECA, the division of the focal surface among eight C11204-02 bias voltage generators allows for further refinement of  $V_{DAC_i}$ . Effectively, the same minimization process is applied for each of the eight subdivisions each containing 32 channels.

- Find  $(V_{bias_{2n}} - V_{br_i}) \cdot \Delta G_i \geq G_{min}(V_{bias})$  for  $n = 1, \dots, 8$  and  $i = 1, \dots, 32$
- Find new  $V_{DAC_{2i}} = V_{bias_{2n}} - V_{br_i} - G_{min}(V_{bias}) \cdot \Delta G_i^{-1}$

The expression for  $V_{bias_{2n}}$  and  $V_{DAC_{2i}}$  are stored in the flat field file which is passed via command line at initialization of the measurement run and retained in the EEPROM of SiECA. These values set the C11204-02 bias voltage and Citiroc input DAC values resulting in uniform gain across all channels of the four S13361s with minimized values for  $V_{bias_{2n}}$

and  $V_{DAC2}$ . These voltages are set based on the room temperature measurements made in SPOCK and correction due to the temperature measurements at the sensors can be made according to the published temperature dependence from Hamamatsu [6].

### 4.1.3 PDE Flat Fielding Theory

Flat fielding with the PDE is similar in process to the method for a gain flat field however the parameterization of the bias voltage dependence is no longer a simple linear regression. Following the exponential formulation presented in [70], we fit the PDE dependence on  $V_{ov} = V_{bias} - V_{br}$  as:

$$PDE(V) = PDE_{max} \cdot [1 - e^{-(V-V_{br})/\alpha}] \quad (4.1)$$

This function provides an estimate of the theoretically achievable PDE in  $PDE_{max}$ , a comparable value to the breakdown voltage and  $\alpha$ , a parameter for the sharpness of the PDE rise to  $PDE_{max}$  which varies between channels substantially. Measurement of  $PDE_{max}$  is intrinsically difficult as further increasing  $V_{ov}$  beyond a few volts above  $V_{br}$  risks damaging the sensor as excess current will be forced through the quenching resistor during a breakdown causing substantial heat. As this leaves the asymptotic approach to  $PDE_{max}$  unconstrained, this value should only be used in reference to the others as a fitting parameter and not an absolute measurement. The intention of PDE flat fielding differs from gain flat fielding in

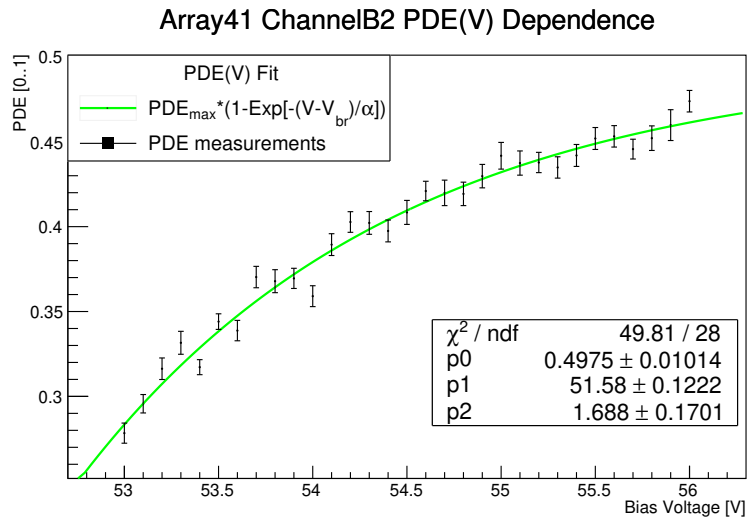


**Figure 4.2:** Example  $PDE[V_{bias}]$  fitting with Equation 4.1

the resulting image. When the rate of arriving photons is less than the recharge time of the SiPM and counting each photon is more useful than measuring the charge deposited, having a camera with uniform PE production capability, and thus number of PE, is more useful than resolving the exact charge of the collected PE and then back calculating the number of incident photons from calibration measurements. Additionally, thresholds on each channel can be set such that a charge excess must exceed  $n$ -PE effectively allowing filtering of dark counts for  $n > 1$ . Cross talk remains, however, the generation of optical crosstalk is minimal for a dark electron drift cascade, and can be corrected for by systematic probabilities.

### 4.1.4 Flat Fielding Results

From the measurements shown in Characterization (Figures 2.7, 2.8, 2.10) we can assess the uniformity before and after flat fielding with each method and compare the estimation

of the breakdown voltage between the two fit based calculations. While  $V_{br_i}$  and  $\Delta G_i$  are independent of bias voltage, PDE and gain for are displayed for the nominal bias voltages of 52 to 57 V. The resulting averages and standard deviations are provided in the legends of the respective plots. Breakdown voltage  $V_{br_i}$  and  $\Delta G_i$  are determined by the linear fit of gain dependence on  $V_{bias}$  and the exponential fit of PDE dependence on  $V_{bias}$  will be carried out following the flat fielding discussion. As shown in the raw characteristics, increased  $V_{bias}$  leads to narrowing of the PDE distribution. This is to be expected given the asymptotic approach to  $PDE_{max}$ . Since the gain is modeled by a linear function, it is also expected that the distribution width will not be impacted changes in  $V_{bias}$ . From these primary measurements, refining the uniformity of the focal surface by the methods described above yields the following results.

### Gain Flat Fielding Impact

Flat fielding on the gain of each channel results in a  $\delta$ -function like distribution, by design. The resulting PDE distribution, however, is also refined slightly at each voltage. The de-

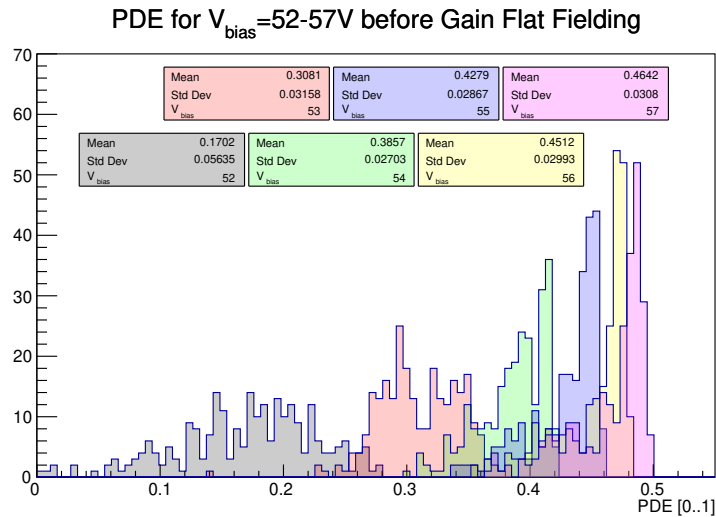


Figure 4.3: PDE distributions for set  $V_{bias}$  before gain flat fielding

crease in the PDE with flat fielding on gain is expected as we take the lowest gain as the reference point and reduce the other channels to match. In reducing the gain to achieve flat fielding, we reduce the  $V_{bias}$  seen by each channel which reduces the PDE in accordance with the exponential fit. Improvement to this method would be taking the average gain as the target, increasing  $V_{bias}$  for the channels with lower than average gain and decreasing for those with greater than average gain for each voltage. Considering the divergent nature of the PDE fit exponential with decreasing  $V_{bias}$ , we would expect the PDE distribution to broaden for decreasing  $V_{bias}$ . The narrowing of the PDE distribution indicates that the PDE and gain are not independent, as expected and discussed in [4, 70] in which the effective  $V_{ov}$  is related to the avalanche probability. Since  $V_{ov}$  is linearly related to the gain and exponentially to the PDE, the improvement in uniformity in PDE when performing a gain flat fielding is a natural benefit.

### PDE Flat Fielding Impact

Application of a PDE flat fielding should provide a focal surface with an equal probability of electron cascade generation for an incident photon in each channel. This uniformity in

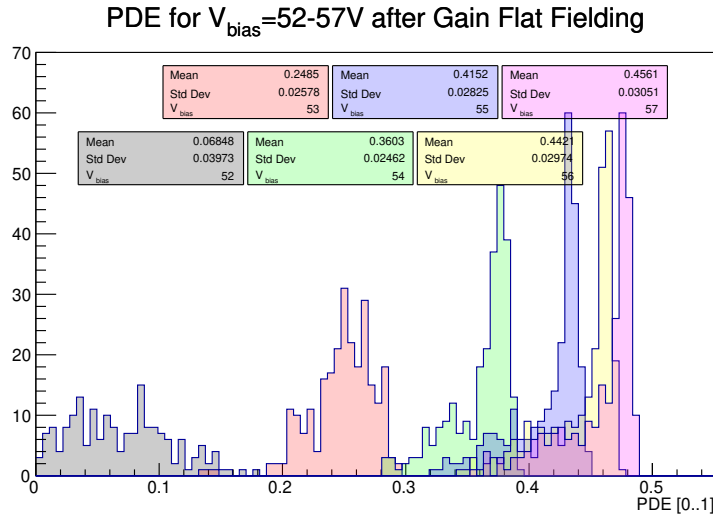


Figure 4.4: PDE distributions for set  $V_{bias}$  after gain flat fielding

probability comes at the cost of uniform gain resulting in a need for a finely tuned threshold setting corresponding to the desired PE triggering amplitude. Where the gain flat fielding resulted in slight narrowing of the PDE distribution with increasing voltage, the exponential form of the PDE results in increased values of  $V_{DAC2}$  at higher voltages. These larger voltage offsets to achieve uniform PDE lead to large deviations in gain. Furthermore, the larger variation in  $V_{DAC2}$  at higher voltages leads to broadening of the gain distribution in addition to the significant decrease in gain across the camera as the least sensitive channels are approaching  $PDE_{max}$ .

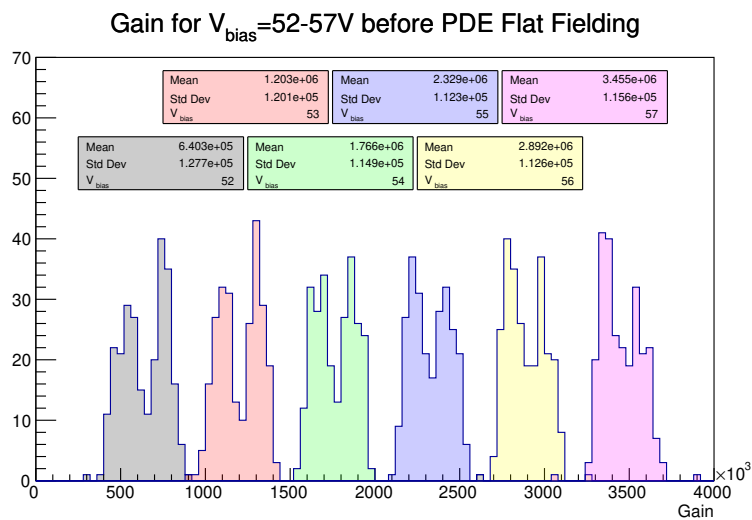


Figure 4.5: Gain distributions for set  $V_{bias}$  before PDE flat fielding

Measurement of the PDE is less robust than the measurement of the gain. The reliance on Poisson distribution of PE, in separate GAPDs for each photon, with uniform PDE assumed for each GAPD is stretching the realistic expectations of SPOCK. An upgrade to a system with a single photon emission laser would greatly reduce the complexity and assumptions made in this calculation. Increasing duration of the PDE measurements was not feasible in this work, neither was correction for small variations in operating temperature, fluctuation in illumination intensity during measurement or ambient electronic noise in the laboratory

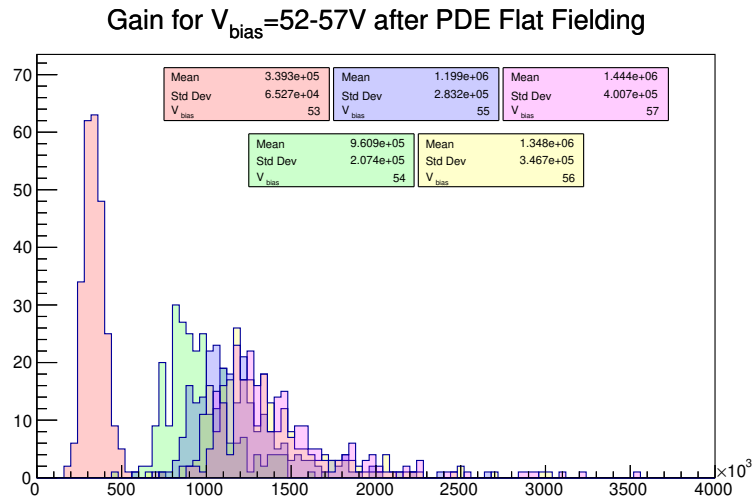


Figure 4.6: Gain distributions for set  $V_{bias}$  after PDE flat fielding

setting. These factors could lead to decreased sensitivity of certain channels exacerbating the spreading characteristics of the PDE flat fielding procedure.

### Breakdown and ASIC Input DAC Voltage

The fitting of gain and PDE dependence on bias voltage both provide a measurement of the breakdown voltage for each channel. Determination of  $V_{br}$  is taken to be the bias voltage at which the gain, or PDE, is zero. In both cases this is an extrapolation from fitting the measured gain, or PDE, above breakdown with the model described in the previous chapter. Neglecting the outliers which can be attributed to systematic error, the PDE calculation

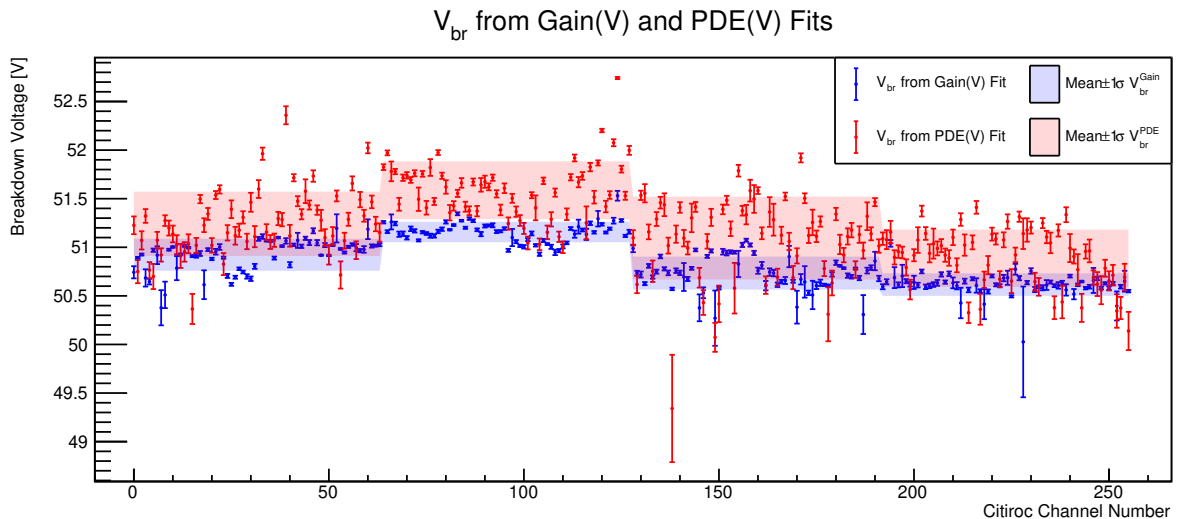
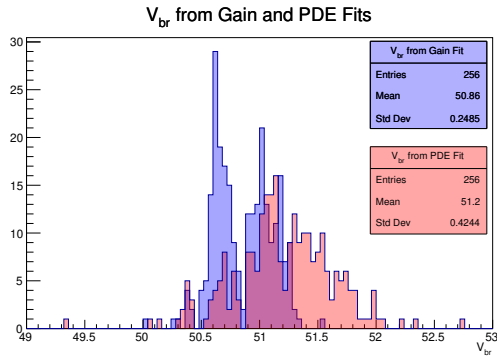


Figure 4.7:  $V_{br}$  from gain and PDE fitting

provides an overestimate compared to the results from the gain calculation. Furthermore, given the larger systematic error from the PDE fit, the error on the breakdown voltage from the PDE exhibits greater uncertainty. The vertical offset between the Gain and PDE fit determinations arises from the difference in fitting function and the deviation from a discrete transition in operation between  $V_{bias} < V_{br}$  and  $V_{bias} > V_{br}$ , as shown in [11]. Despite

these differences, the deviation from average for each channel is comparable indicating that while less accurate, the PDE calculation is valid since it captures the asymptotic approach to  $PDE_{max}$  and the low voltage limit,  $V_{br}$ . While  $V_{br}$  is a key parameter of a SiPM, it is of little consequence in flat fielding calculations so long as the selected target parameters, flat field gain or PDE, are positive. Distributions of the breakdown voltages determined by gain and PDE fits reflect the already described characteristics: PDE determination leads to a higher breakdown voltage with more uncertainty due to measurement methods. The distribution does indicate that for the gain fit determination, the 256 channels used in SiECA are distinctly divided into a lower and higher  $V_{br}$  populations. This separation is not present with the PDE



**Figure 4.8:** Distribution of  $V_{br_i}$  values for the four S13361s arrays used in the second SiECA construction from Gain and PDE fitting

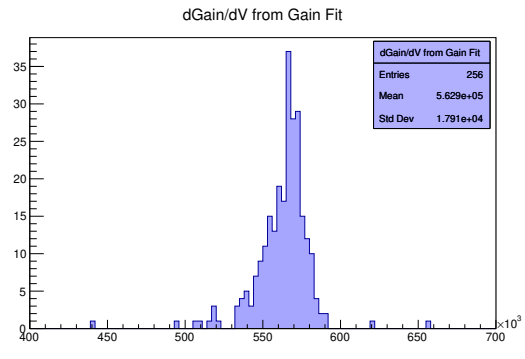


**Figure 4.9:** Distribution of  $\Delta G_i$  for the four S13361s arrays used in the second SiECA construction

determination which I attribute to uncertainty in the measurement and fitting. Additionally, systematic overestimation would lead to a larger impact for the lower  $V_{br}$  channels as the fitting of the PDE is only constrained by non-zero PDE measurements. An improved fit on PDE with the  $V_{br}$  determined from the gain fit should lead to an improvement in matching device response however this has not been further tested in this work.

## 4.2 Sensitivity and Response of SiECA

Measurements discussed so far in this chapter have come from the single channel readout board designed and build by Max Renschler and described in [7]. Application of these measurements allows for tuning of the bias voltage applied to each MPPC channel through the input DAC of the Citiroc to achieve a camera with a focal surface uniform in either gain or PDE. This section details the analysis of the uniformity and sensitivity of SiECA as well as assessing cross-talk in the electronics.

### 4.2.1 Single Channel Illumination

To determine the necessary ASIC settings, specifically the gain and threshold for each channel, to operate in peak counting mode, a parameter scan has been developed. By scanning over the gain and threshold combinations for a set of voltages, it is possible to see the necessary threshold setting for a given gain and bias voltage corresponding to the discrete PE amplitudes. This measurement could be run over the entire camera for excellent understanding of each channel however, for time reasons, here we only illuminate one channel, Array 1 Channel B2. In this measurement, after determining the collimator ratio, the light intensity is set to three photons per pulse with a pulse frequency of 1 MHz. This frequency ensures that each 2.5  $\mu$ s GTU is illuminated on average 2.5 times or an average of 7.5 photons will be

incident on the illuminated channel each GTU. SiECA is then operated with each parameter setting,  $V_{bias}$  and  $V_{DAC2}$ , passed by flat field file, gain and threshold for the camera by editing the *siecatcommon.h* and recompiling the operation code. One hundred events, each containing 128 GTUs, are recorded before moving to the next settings within the bash script *SiECAparameterscan.sh*. This script checks the file size for each set of parameters and if it does not match what is expected, the file is rerun. Errors in file size can occur due to FPGA/FIFO interface faults which are somewhat common, occurring for approximately 2% of measurements. By looping over the parameter list until no setting needs to be rerun, this autonomous scan can be allowed to run unattended. In its current setting, with six voltages, 34 gains and 211 thresholds, this amounts to 142.3 GB and requires approximately 220 h to complete. From the generated measurements, calculation of a signal to noise ratio is determined in the following expressions for illuminated channel  $a$ .

$$N_{light} = \sum_i^{256Channels} \delta(i, a) \sum_j^{100Events} \sum_k^{128GTUs} Counts[i][j][k] \quad (4.2)$$

$$N_{dark} = \left( \sum_i^{256Channels} 1 - \delta(i, a) \right) \sum_j^{100Events} \sum_k^{128GTUs} Counts[i][j][k] / (256 - 1) \quad (4.3)$$

$$SNR = \frac{N_{light} - N_{dark}}{N_{dark} + 1} \quad (4.4)$$

In Equation 4.3, the counts on the non-illuminated channels are normalized by the number of channels. The same should be done in Equation 4.2 if more than one channel is illuminated but here we use only one. By assuming the gain flat fielding is sufficient to also standardize the dark count rate, it is possible to determine the signal to noise ratio,  $SNR$ , from Equation 4.4 where the numerator is the counts in the illuminated channel minus the expected dark counts in channel  $a$  while the denominator is the average dark counts plus one to prevent  $\approx 1/0$  in the case of low dark count measurements. The empirical introduction of this +1 in the denominator suppresses the parameters that have just a few dark counts and thus a near 0  $N_{dark}$  from appearing significant in the resulting  $SNR$  plots. Figure 4.10 is instructive in

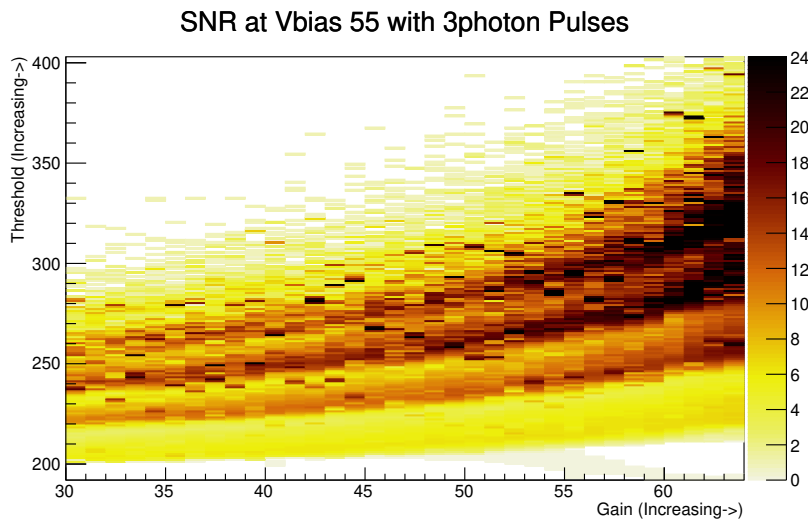


**Figure 4.10:**  $SNR$  plot for  $V_{bias} = 55$  V

illustrating the distinct separation of PE peaks within the measurement parameter space. To understand the implications, we look at the shape for one gain. Moving upward in increasing

threshold from the X-axis we start in a null space in which the threshold is within the 0-PE pedestal. As the pedestal is uniform and measured by all channels, illuminated or not, whenever a PE cascade is not present, the illuminated channel sees less pedestal events than the average dark channel. For this plot, all negative SNR values have been set to 0 to avoid confusion. Above the pedestal, we enter the 1-PE peak signal amplitude. This region is notably lighter than the multi-PE peak due to the signal generated by drifting electrons in the depletion region of the GAPDs in each MPPC channel. For the room temperature measurement, 0.5 MHz dark count rate is expected [6] which is of similar magnitude to the 7.5 MHz-photon signal. Above this level, dark noise is increasingly suppressed as multi-PE dark counts are energetically unlikely. The next dark band is the 2-PE amplitude threshold which is notably darker due to the substantially decreased dark count rate achieving this charge amplitude. Subsequently higher PE peaks are distinct for low to moderate gains but become indistinct due to the non-linearity in the amplifier at high gain levels.

From this plot, determination of the threshold and gain setting can be selectively determined for exclusion of the pedestal and dark count events but also for higher thresholds limiting the selection to several-PE signals at the cost of decreased collection and energy resolution. Generation of a subset of this parameter space in this manner once SiECA is installed in a host telescope provides a useful guide to setting the operational parameters for measurement to exclude background light. Integrated measurements will not have a single illuminated channel with the rest of the camera dark, rather the whole camera will observe the background. Combining the measured background signal and the laboratory reference plots, the voltage, gain and threshold necessary can be determined by inspection.

Comparison with the other measured  $V_{bias}$  voltages can be made in Appendix B. From the measured voltages with applied gain flat fielding from Characterization measurements, the separation of the PE bands is substantially increased with increasing voltage. At high pre-amplifier gain, these bands effectively merge indicating the combined gain of the highly biased MPPC and high gain pre-amplifier are introducing substantial variation into the charge produced during APD discharge. This ambiguity by smearing out the PE peaks makes this  $V_{bias}$  region unsuitable for setting a specific PE threshold. Decreasing the biasing voltage and pre-amplification has an opposite but equally problematic effect by compressing the PE regimes to a single pre-amplifier gain and threshold region of the phase space. Thus, a balance between these two extremes is taken for operation. For the EUSO-SPB1 flight this was at a pre-amplifier gain of 55 and a threshold of 243. This determination was made by hand and eye under limited time for further analysis. Ideally, this setting should be in the 1 PE band which will be sensitive to dark counts but also the most sensitive to any arriving photons from the night sky, both from background and EAS allowing for separation and analysis of both in post processing of the flight data. More details on this flight and the results are presented in the Deployments chapter later in this thesis.

#### 4.2.2 Illuminated Flat Field test

Verification of the calculated flat field corrections made in the bias voltage generators and ASICs can be verified by the use of either full field illumination in which the entire focal surface is uniformly illuminated or calibrated measurement at each channel. As traditional flat fielding utilizes full field illumination, in this thesis we pursue the second approach, measurement of each channel before and after flat fielding corrections for a range of operating parameters. Channel by channel measurement is inherently a very slow process and should be automated as much as possible. Given time constraints of this thesis, testing of only the gain flat field has been carried out. Additional correction of the pre-amplifier

and/or threshold level in the ASIC must be carried out for the use of the PDE flat fielding as described in section detailing the method.

### SiECA Two Dimensional Scan

The flat focal surface of SiECA contains 256 MPPC channels, each with individual parameters as described in the chapter on Characterization. By flat fielding the sensors in gain, the measured signal amplitude for a single GAPD discharge should be the same regardless of channel. Thus, measurement of the uniformity after flat field corrections provide information about the parameters not flat fielded upon, PDE in the case of a gain flat field, as well as systematic issues such as electronic cross-talk due to PCB layout. By scanning over each channel individually we can separate these two sources of inhomogeneity while a full field illumination measurement does not allow this level of deconvolution.

In the case of SiECA, we utilize the SPOCK hardware with the movable light source to scan over each channel, record one hundred measurement events (100 events with 128 GTUs each integrating counts over  $2.5\ \mu\text{s}$  generates binary files of approximately 3.3 MB) and then move to the next channel. The collimated light source is tuned to emit 3 photons per pulse at 1 MHz yielding an average illumination of 7.5 photons/GTU. To minimize absorption by the TSV in each channel, the exit aperture of the collimator is positioned 2 mm from the MPPC surface. Spread of the emitted light from the collimator at this distance is well within the  $3\ \text{mm} \times 3\ \text{mm}$  area of each channel so illumination of other channels is negligible. Furthermore, the black absorptive collimator, and black SPOCK interior should absorb any light reflected from the MPPC surface before arrival at a second MPPC channel can occur.

Measurement of individual channels directly is still necessary to determine PDE however, even with uncharacterized MPPC a successful flat fielding could be carried out by performing the same scan over each channel for the range of operational settings: bias voltage, pre-amplifier gain, and threshold. Without access to the integrated charge finger spectra, PDE would have to be inferred from the measurements of count rate for a known light source which is susceptible to systematic error and would require extensive measurement to amass statistical accuracy but it is theoretically feasible. Again, given the time constraints of the SiECA development and the desire to verify the previously measured MPPC characteristics, here we undertake the full characterization with dedicated hardware as described in Characterization and then correct for non-uniformity with bias voltage and ASIC parameter manipulation. We verify these corrections with measurement of each channel for a nominal voltage of 55 V, nominal pre-amplifier gain corresponding to a region of the parameter scan space with clearly distinct PE peaks in Figure 4.10, nominally 55, and then scan over the range of thresholds for proof of principle. Refinement of this practice should be considered for all future applications as it is tedious to scan a large parameter space for every channel.

### Results of 2D Scan

Since full events are recorded, with every channel's count in each GTU included, we can make assessment of the uniformity under illumination but also the impact of illumination on a neighboring channel or electronic noise. Thus, we have insight into both the uniformity of each sensor and the electronic effects of the supporting electronics. This type of scan will also highlight any channel mapping errors such as a mismatch of ASIC orientation in the hardware and analysis software. For simplicity, we will look at uniformity, the number of counts on each channel per GTU of illumination and the noise impact in neighboring channels of the illuminated channel. In this instance, neighboring is taken to be the up to eight channels (four meeting at a common edge and four meeting at a common corner) closest to the illuminated channel though in principle the influence of any channel could be



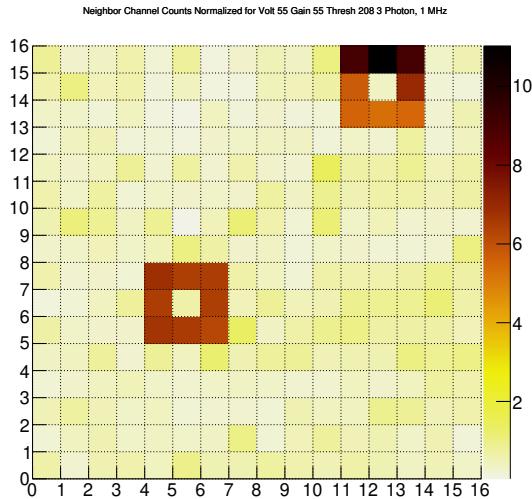


**Figure 4.13:** Neighbor noise counts with characteristic noise rings around locally influential channels. Low threshold in 1 PE region

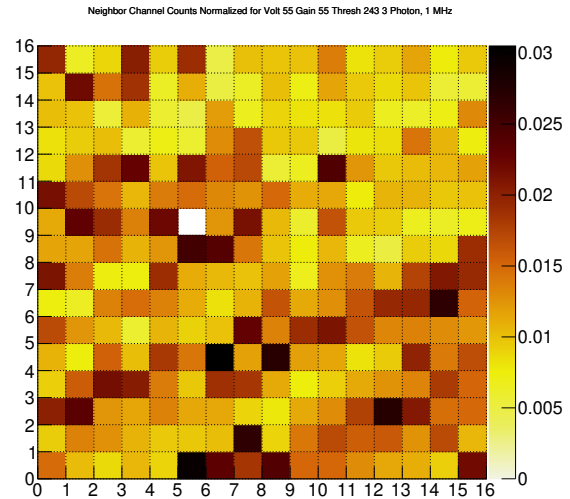


**Figure 4.14:** Neighbor noise count at EUSO-SPB1 flight threshold setting

dark current is more likely than the uniform crosstalk in the PCB routing. However, this measurement corresponds to a threshold well within the pedestal (0 PE peak) level which will be saturated with both the illuminated avalanches, dark counts and dark current (since SiECA only has one trigger, low thresholds will exhibit all higher signals as well as the low amplitude signals in total counts). This assessment could be repeated with reversed logic: By plotting the combined counts on the surrounding neighbor pixels of the illuminated channel, we will see only the influence of illuminated counts. As this scan is currently implemented to look for any cause of noise, the current summation is preferred but further analysis is already possible with current measurement.

Examining Figure 4.14 we can see that there is a distinct structure spanning multiple channels and even multiple MPPC arrays at the EUSO-SPB1 flight gain and threshold. Diagonal influence paths moving upward from left to right across the focal surface are also clear for other thresholds within the 1 PE region. Currently, I do not have an explanation for this channel influence structure. Further analysis of the board layout, highlighting the noisy channels and looking for possible sources of crosstalk is being undertaken however no indications of origin currently are apparent.

In brief conclusion to this chapter on the application of Characterization measurements for constructing uniform arrays of sensors, the following points are of the most significance:

- Flat fielding on Gain
  - Similar amplitude signal
  - PDE must be corrected manually
  - Better for charge integration when many photons are arriving
- Flat fielding on PDE
  - Uniform probability of detection across sensitive surface
  - Gain and Threshold can be corrected in ASIC
  - Better for individual photon counting
- Full field flat fielding is more efficient

- Channel by Channel flat fielding indicates readout chain noise issues

Once Calibration is complete, the resulting camera is properly optimized for measurement, at least as well as is possible in the laboratory. The next step is deployment to a facility or installation which maximizes the possibility to achieve the scientific goals set out prior to the construction of the camera. In the case of SiECA, these opportunities take the form of the EUSO-SPB1 flight and installation in the Pierre Auger Observatory HEAT telescope number one as described in the following chapter.



---

---

# CHAPTER 5

---

## SiECA Deployments

The development of SiECA envisioned successful camera construction and testing before deployment with a host telescope designed for the detection of cosmic rays. As a prototype for future orbital detection systems, such as EUSO or POEMMA, the clear opportunity presented by the EUSO-SPB1 flight was ideal. Additional testing at the Pierre Auger Observatory HEAT telescope site was envisioned as an evaluation of the Central Laser Facility (CLF<sup>1</sup>) and chance to detect cosmic ray signatures. Regrettably, both of these endeavors were cut short due to technical failures, as explained in this chapter, however the integration and available measurements provide insight for future developments.

### 5.1 EUSO-SPB1

As described in the Introduction, EUSO-SPB1 was a refractive telescope designed for downward looking measurements of UHECR fluorescence and Cerenkov signatures from an altitude of 33 km while carried as the 2017 NASA Super Pressure Balloon scientific payload. In flight configuration, two PMMA lenses provided a field of view of  $11.1^\circ \times 11.1^\circ$  to the PDM constructed from 36 MAPMT modules with BG3 filter glass to bandpass wavelengths corresponding to the nitrogen fluorescence spectrum [56]. SiECA was attached to the edge of the PDM with the sensitive surface of the MPPC in-plane with the MAPMT photo-cathode. To maximize the field of view of SiECA, it was positioned in the center of the edge to make use of the circular focal area of the lenses which extends beyond the PDM. Originally designed to maintain the EC spacing of the PDM with 1 mm between edges of the BG3 filter glass windows on each sensor, SiECA was displaced further away from the PDM, 7.5 mm, to prevent contact between the filter glass windows during a potentially violent launch and to allow the insulation for the PDM heating system to be placed between the two cameras. The 3D printed plastic brace connecting the aluminum SiECA main frame to the PDM frame maintains the horizontal and vertical position of SiECA with minimal flex under expected launch forces. It is square to keep the orientation of the SiECA focal plane parallel to that of the PDM. Calculation and design of braces angled to match the 2.5 m focal surface specified by the lens configuration were abandoned due to the inclusion of the heater and the choice to make the PDM planar rather than curved. Optical testing by Johannes Eser indicates the impact of a flat focal plane is less than the variation in focal surface due to wavelength dependence of the lenses, 15 mm when the middle chromatic correction lens

---

<sup>1</sup>Central Laser Facility



**Figure 5.1:** EUSO-SPB1 PDM and SiECA alignment before cleaning and heater insulation installation

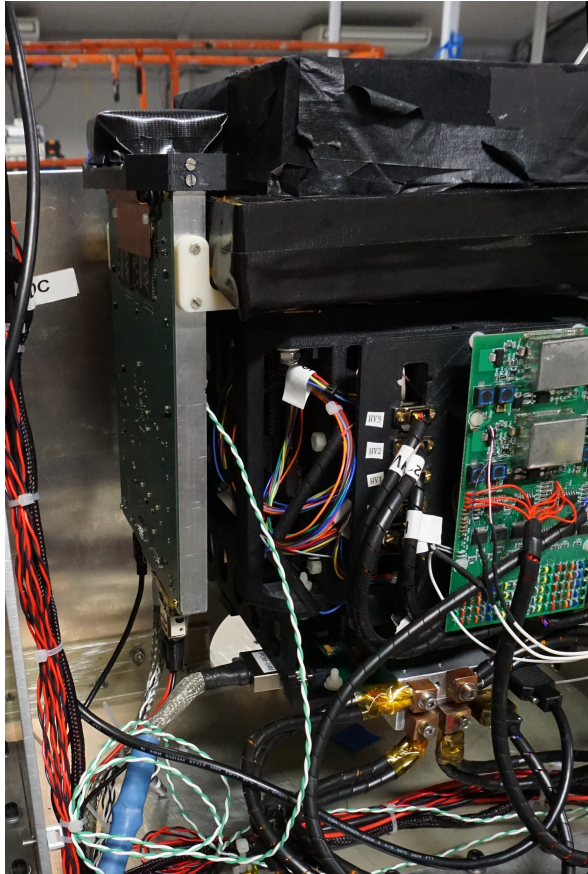


**Figure 5.2:** EUSO-SPB1 PDM and SiECA with PDM heater shortly before detector plate inversion

is omitted from the setup, as was flown [56]. Power supply for SiECA was a commercial DC-DC<sup>2</sup> converter (DPX4024WS05) from TDK-Lambda) to step the nominally 24 V battery supply voltage down to 5 V. SiECA was allocated 5 V with a maximum current draw capped at 2 A however during operation SiECA operates with 0.42 to 0.79 A with a startup current draw of  $\leq 1.28$  A. This DC-DC was switched by the EUSO-SPB1 relay board directly via slow control or via the automated start measurement procedure when the PDM was switched on prior to measurement periods [57]. The clocks described in the chapter titled Hardware were provided by the Clock Board of the EUSO-SPB1-DP<sup>3</sup> as well as a trigger when the second level trigger of the PDM was achieved, indicating a cosmic ray candidate event.

### 5.1.1 SiECA issues on EUSO-SPB1

Despite testing at KIT and extensive communication with the DP development group responsible for the trigger generation, the LVDS trigger signal did not initiate an event readout in SiECA. Through testing, we determined the LVDS signal was being correctly interpreted by the input IC<sup>4</sup> however the FPGA did not respond to the IC generated LVCMOS<sup>5</sup> pulse indicating possible damage to the FPGA for that input. As triggering was not possible in

<sup>2</sup>Direct Current to Direct Current voltage converter

<sup>3</sup>Data Processor, Data and telemetry computer on EUSO-SPB1

<sup>4</sup>Integrated Circuit

<sup>5</sup>Low voltage complementary metal oxide semiconductor digital logic

real time, an alternative, clock based measurement routine was decided on in which SiECA measured constantly when on and software triggered every 15 s effectively measuring background. This triggering routine was definitely not optimal however, with the hardware level trigger inoperable and a software trigger coming from the DP-CPU arriving well after the event of interest was over-written in the ring buffer, a CPU clock trigger was the most reliable method available. Notable interference between SiECA and the PDM-EC located in the adjacent corner, away from the PDM mounting plate. As indicated in Figure 5.4, primarily

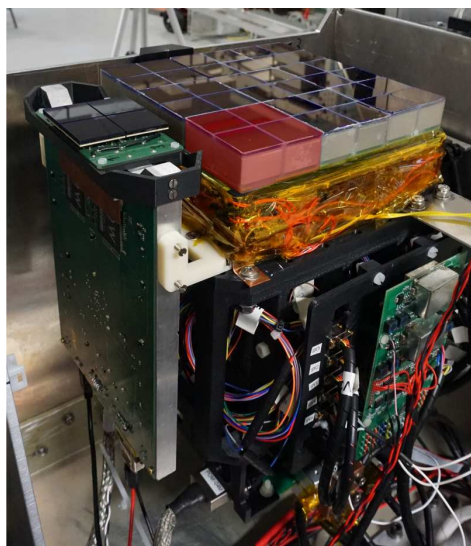


**Figure 5.3:** EUSO-SPB1 PDM and SiECA with noise influenced EC highlighted

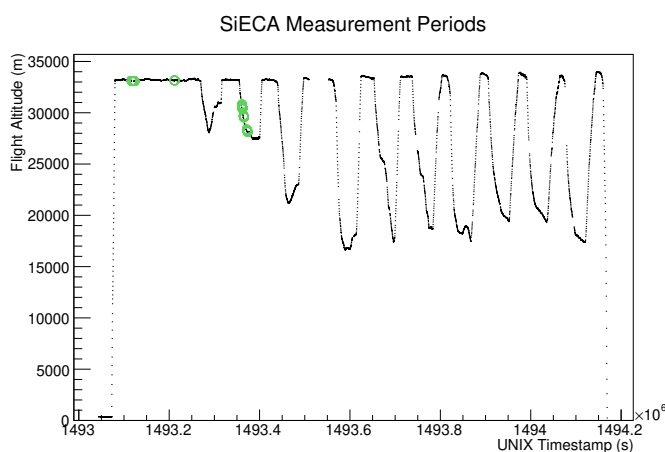


**Figure 5.4:** EUSO-SPB1 altitude with SiECA operation periods indicated in green circles. Descents indicate night cold cycles, rising with heat from the sun

due to the noise impact in the PDM EC indicated in Figure 5.3, SiECA was often not switched on during the flight. The end result of the short flight and constant work by the operators to maximize the scientific benefit of this mission despite less than ideal flight conditions produced nearly 400 SiECA events, each with 128 GTUs integrating 2.5  $\mu$ s windows. These events are substantially varied in composition from empty to amplifier oscillation signals. Understanding the operational conditions, both internal settings and external contributions such as temperature, SiECA was tested under during the EUSO-SPB1 flight provides the first deployment test of SiPM arrays for cosmic ray measurement at the edge of the atmosphere. Thus, the dataset recorded and the subsequent analysis is critical for future developments of similar sensor systems. Preparation for the EUSO-SPB1 flight required the Characterization and Calibration processes detailed in previous chapters to be carried out. Due to time constraints, a full flat fielding, in-situ testing at the EUSO-TA<sup>6</sup> site and laser energy calibration were not possible. Primarily, the calibration settings selected for testing were at the 1 PE level which led to high count rates due to thermal dark counts in addition to atmospheric background. Additionally, the Si-EC PCB flown contained larger blocking capacitors for each channel than were available during the EUSO-SPB1 at EUSO-TA test. The smaller capacitors led to noise on the ground plane for each GAPD discharge further complicating measurement with the pre-flight SiECA model. The resulting flight measurements can be

<sup>6</sup>EUSO prototype telescope at Telescope Array

roughly separated by average channel count rate during the EUSO-SPB1 flight. An arbitrary Interest parameter is calculated for each event where Interest is give by Equation 5.1.

$$Interest = \sum_{Channels} \sum_{GTUs} [Counts - AverageCounts] > 0 \quad (5.1)$$

This is a crude classification as it has minimal consideration of event nature however it does indicate the deviation of an event from constant background. Low interest events have similar counts for each channel in each GTU while high interest events have deviation. Since only the counts above average are considered for interest calculation, and most of the time background is expected to be uniform, this classifier should highlight any event with a short excess of counts above the average background. This is not the case for the 378 flight events as current assessment shows all to be artificially low, expected background or electronic noise leading to high count rates (65 of the 378 recorded events exhibit high count noise signatures).

### 5.1.2 Low Count Events

These events exhibit count rates below the expected UV air-glow of up to 5 MHz per channel FoV. Including the PMMA lens absorption (36.4% throughput) and nominal MPPC PDE (40%) an expected background count rate of  $\approx 0.7$  MHz [56]. Due to the PDM heaters, this is roughly equal to the dark count rate of each SiECA channel leading to an expected combined minimum background of 1.4 MHz or 3.5 photons/channel/GTU. Events recorded during flight with lower count rates than this are clearly indication of a system fault, possibly a misconfiguration at startup however, this issue has not been reproduced in the laboratory with the second SiECA construction so it remains an open issue. The majority of events fell into this category during flight. In fact, all events displaying background like characteristics are below the expected combined background rate. Events of higher count rates all contain a noise signature that can clearly be identified as non-cosmic ray signals.

### 5.1.3 High Count Events

The events that deviate from the low count characteristics previously discussed contain at least one clear indication of electronic noise influence. One is a singular spike in an event in the 124th GTU as seen in Figure 5.5. This noise originates in a few channels for a distinct time

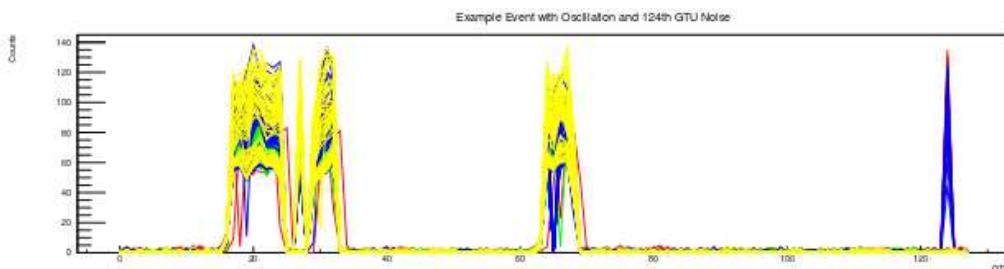


Figure 5.5: Example event with oscillation and 124th GTU noise spike

indicating a process in coincidence with event generation. If this was randomly present in an event then it could be any FPGA or ASIC process however since it is always in the 124th GTU when present, this is clearly an effect from event generation. Assessment with the second construction found this noise to be generated by the FPGA reading the temperature sensors. Correction of the timing for readout of the temperature sensors outside of measurement

window, after an event is triggered either by software or hardware, in the dead-time while the select ring buffer GTUs are being transferred to the FIFO buffer has been performed in the FPGA eliminating this effect. The second form of noise leading to high count rates is more complicated and less understood. Similar to the ground plane feedback issues corrected between the first and second SiECA constructions, this effect impacts all channels, arises quickly, leads to high count oscillations and then quits. This effect is unexplained but seems to be related to ASIC or bias voltage distribution as separation can be seen in the yellow channel's count rates in Figure 5.5 between two equal populations. As each MPPC is driven and read out by two bias voltage generators and two ASICs, separation of the channels into two groups indicates the issue lies with one of these devices. The connection of the bias voltage generators to each half MPPC through the blocking capacitors could allow for this noise to be transmitted through the ground plane of the Si-EC board or feedback from the digital ASIC output could interfere with the amplified analog inputs, spreading over the ground plane of the DAQ and Mezz boards. Deeper assessment of this noise signature has not been undertaken. Regrettably, recovery of the EUSO-SPB1 telescope is not possible as it is currently resting on the floor of the Pacific Ocean. An optimist may comment that a new underwater fluorescence detector has been installed however communication is severely limited and no requests for data transmission have been acknowledged or responded to since splash-down.

## 5.2 Pierre Auger Observatory, HEAT

Following the limited results of the EUSO-SPB1 flight, an attempt was made to measure in coincidence with the HEAT system at the Pierre Auger Observatory in Argentina. Due to the low probability of having an EAS pass through the field of view of SiECA and trigger in HEAT, recall that SiECA does not have internal trigger logic so an external trigger is required, measurement of the calibration beam was determined to be the most beneficial test for SiECA. Despite testing with spare SLT<sup>7</sup> boards at KIT, the trigger LVDS signal again did not generate an event for readout further indicating issues with the LVDS chip, implementation or FPGA handling of this signal. Much of the time at the Pierre Auger Observatory was wasted trying to get this trigger working. Final solution was a work around involving the data handling Raspberry Pi receiving the SLT signal and then initiating a software trigger. Regrettably, wind damage to HEAT-1, where SiECA was positioned to see the CLF beam, and an unstable UPS<sup>8</sup> prevented measurement aside from a partial preliminary parameter scan. The parameter scan was a subset of Figure 4.10 run during the night wind damaged the telescope enclosure. Ideally, the resulting scan would be used to set the proper voltage, gain and trigger threshold to determine optimal operation parameters for the location. Regrettably, this deployment was a complete failure.

---

<sup>7</sup>Second level trigger: pattern recognition trigger in HEAT

<sup>8</sup>Uninterruptible Power Supply



---

---

# CHAPTER 6

---

## Conclusions

Continued development of silicon photomultipliers has brought devices with similar detection capabilities to the vacuum photomultipliers to the public market however, implementation of these devices in astro-particle physics has yet to fully benefit from the decreased operating voltage, decreased volume and mass, increased durability and mass production capability of SiPM. The challenges of implementing a new sensor in place of an older but fully developed system remain until the engineering and testing is done. SiECA establishes the current capability of available components and construction techniques available at the time and shows that MPPC arrays are comparable, even preferable in some instances, to MAPMTs for astro-particle physics devices.

This chapter will likely be the most useful for anyone looking to continue in this work, developing camera systems with SiPM. Here I will attempt to outline the challenges that remain and the lessons learned that are not explicitly stated in the rest of the thesis. As the majority of the main body is devoted to the logical progression, this will be where all the odd occurrences, lesser known issues and things that get overlooked by those with extensive experience but are often stumbled upon by those actually tasked with the work. I hope to separate the issues by hardware and logistics as software and analysis is mostly included in the main chapters of this thesis.

### 6.1 Hardware

This thesis is devoted to the development of hardware, however, many of the complexities are overlooked in the main chapters for continuity. This section will be less supported by measurement and more directed at the experiences during the construction of SiECA that will be most influential for similar cameras or applications of similar camera elements. I will attempt to present the issue encountered, the process of resolving said issue and the final result of each consideration with the emphasis on the impact to design and function.

#### 6.1.1 Connector or SMD MPPC

In the construction of SiECA, we opted for the S13361 devices with connectors already attached. This was beneficial for prototype testing and calibrating the MPPC arrays in already developed boards used previously. However, this ease of connecting the arrays to a calibration board and then to the Si-EC board lead to complications in the routing of the necessary traces for biasing and reading out the MPPC channels. Due to the high density connections,

two for each channel plus a few no contact pins for standard connector sizing, the resulting ST4-40<sup>1</sup> array connector and the SS4-40 receptacle on the Si-EC board have a pitch of 0.4 mm. This is currently a very small pitch for making all the necessary connections, especially when considering the need for individual channel decoupling resistor and capacitor pairs.

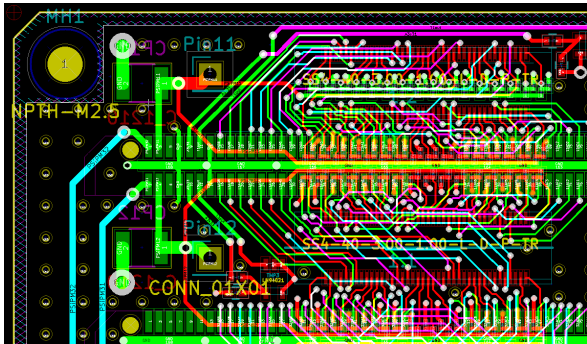


**Figure 6.1:** Complexity of PCB routing with MPPC connectors requiring 0201 scale resistors and capacitors

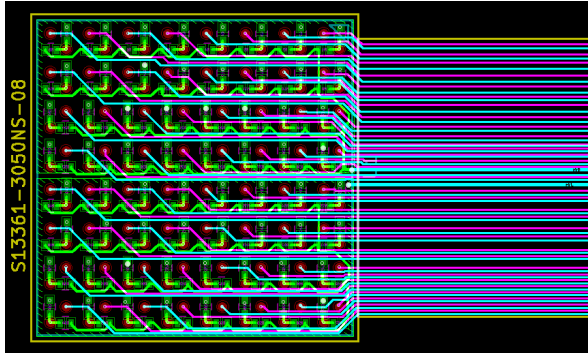


**Figure 6.2:** MPPC routing with kapton flexible PCB connection to ASIC support chip. Channel resistor and capacitor are 0402 scale

Comparing the PCB layout complexity for MPPC with the ST4-40 connector, Figure 6.1, and for directly soldering the MPPC to the support PCB with a kapton flexible PCB connection to the bias voltage and ASIC PCB, Figure 6.2, the benefits of direct assembly are apparent. Reduced vias per channel, reduced signal trace overlap, more uniform trace length, all are benefits of the kapton flexible PCB solution however the assembly process for this BGA<sup>2</sup> structure is more complicated and must be completed before MPPC characterization can be started. Given the experience and developed hardware for testing S13361 with connectors, SiECA used these devices however future developments are urged to consider the connector-less option critically.

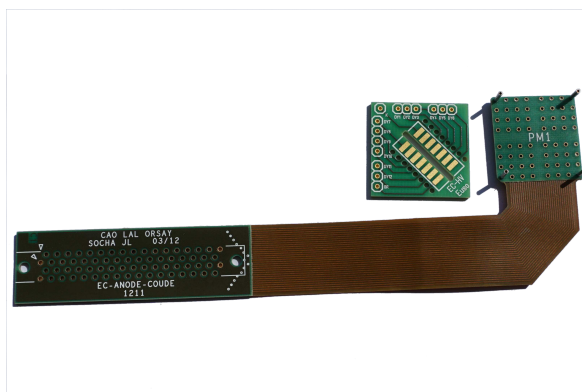


**Figure 6.3:** MAPMT EC PCB with kapton flexible PCB for signal transmission and second bias voltage distribution PCB

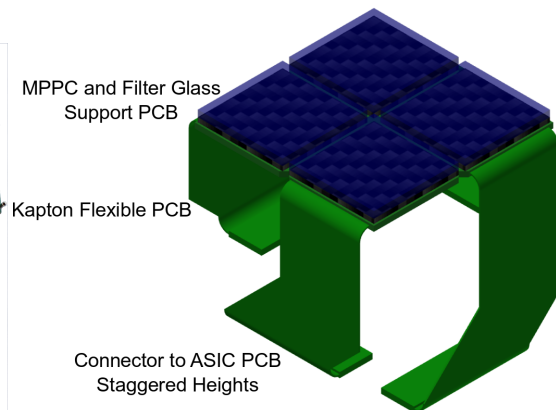


**Figure 6.4:** Rough mock design for EC using kapton flexible PCB and S13361-NS<sup>a</sup>

<sup>a</sup>Hamamatsu S13361-3050NS-08 64 channel MPPC

In the case of SiECA, the connectors to the DAQ and Mezz boards further restricted the space available for biasing passive components and complicated the via structure in order to retain the 4 active layer design. This complication could be reduced by the use

<sup>1</sup>Samtec ST4-40-1.00-L-D-P-TR array connector

<sup>2</sup>Ball-Grid Array, 2D grid of contacts instead of edge only packages

of blind or buried vias however this method would at least double the PCB production cost. For a large scale project in which parallel production is more essential, use of the SMD version of the MPPC array, S13361-NS. Each array should be mounted to a modular support PCB either holding four arrays as done in SiECA or individually in which case a more complex support structure is needed to unify the EC unit, as done in the MAPMT EC design. Modularization of the EC surface with individual boards for each MPPC array would allow for a stand alone calibration stand to be built for testing one array at a time. Any defect or failure of a given array could be replaced as easily as the S13361 arrays but connection to the ASIC board(s) would be simplified. To implement a flexible EC arrangement, for angular correction in the focal surface, flex-rigid PCB construction should be used, as done in the PDM. Since the MPPC array is in direct thermal contact with the support PCB, connection of the temperature sensor(s) to the back side of the board should be possible with careful arrangement to minimize noise.

### 6.1.2 PCB Warp

Significant board warping during solder reflow occurred with the second iteration of Si-EC boards. The prevailing theory for this thermal warping is due to copper pour on bottom, QRF8 side, layer with the long traces connecting the temperature sensors causing uneven pour connection. During heating and cooling this uneven thermal mass (the copper pour) lead to differential cooling and thermal stress. The warp constitutes a 0.4 mm bowing (convex on sensor side) across the long dimension of the Si-EC board. While small, this deviation from flatness is significant for the SS4-40s sensor connectors but catastrophic for the QRF8s connectors, resulting in failed solder contacts even when substantially weighted during the reflow soldering process. Consideration of the impact to optical sensitivity uniformity of the EC focal surface has not been evaluated as no boards were successfully produced. Alleviation of this issue could be realized with a structural clamp of significant rigidity but this would require much longer reflow times to prevent cold shoulder solders near the clamp (as the clamping material would act as a cold thermal reservoir). For practical purposes, the board was redesigned with copper pours only on traceless layers and the warping seems to not occur with the latest version of the Si-EC boards. The substantial increase in the size and

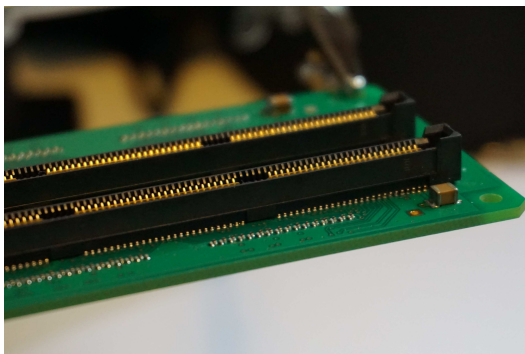


**Figure 6.5:** Solder disconnect due to warp visible on right side of QRF8 connector

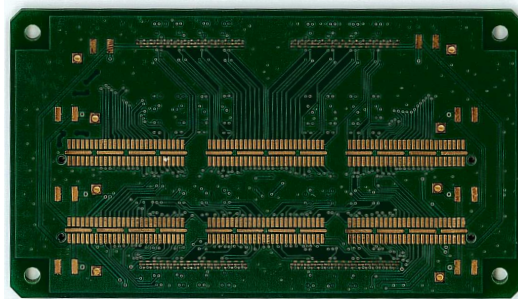


**Figure 6.6:** Si-EC-V2 PCB, QRF8 side. Bowing traces separating sections of ground plane copper pour seem to be the cause of PCB warp during reflow soldering

number of vias connecting the ground planes helped alleviate thermal stress during reflow and cooling. This issue could have been eliminated by the use of modular MPPC support boards as all traces would be much shorter and therefore less likely to lead to thermal defor-

mation during soldering. Furthermore, the use of rigid-flex PCB would eliminate the need for connectors on the sensor support board(s).

### 6.1.3 ASIC Considerations

The work done to construct the readout chain for SiECA is impeccable for the time available. Now at the end of the project I have realized that one of the improvements that would make SiECA a more stand alone device would be space in the FPGA for a self triggering capability. Currently, the under utilized charge readout is possible but incredibly slow at the ASIC level so pulse counting is the best we can do with these ASICs while still being able to reconstruct the shower progression as the charge integration readout time is on the order of  $10\ \mu\text{s}$ , much too long to capture multiple consecutive images of the shower development. This timing issue becomes even more of an issue when detection of Cerenkov signatures is desired as the entire luminous event occurs in less than  $100\ \text{ns}$ . To resolve the development of the Cerenkov event, time binning at the level of at least five bins per event is necessary to constrain the light production curve which resolves  $X_{max}$  and the relative steepness needed for composition studies. This indicates the need for faster ASICs and SiPM tuned for faster recharge times than the S13361 used in SiECA.

## 6.2 Final Remarks

The development of the SiECA camera has provided substantial insight into the complexity of building a complete sensor and readout chain in a short time limit. However, the resulting camera does show that current technology is sufficient to build a camera with SiPM arrays with single photon sensitivity, compatible timing (down to  $1\ \mu\text{s}$  or faster GTU) with minimal dead time, in a structurally compact and low power consumption package. With this camera we have shown the benefit of channel by channel bias voltage regulation to flat field at the sensor level with methods for flat fielding in sensor gain and PDE with motivations for each in the respective high and low relative flux detection regimes. While the deployment opportunities with SiECA, in EUSO-SPB1 and HEAT at the Pierre Auger Observatory, suffered host camera failures severely limiting data production, the capability of SiECA to adapt to a wide range of operational settings is evident. Thus, the search for cosmic rays with the SiECA camera is left to the successor of the author and I wish you the best of luck.

---

---

# APPENDIX A

---

## Appendix A: Schematics

### A.1 Mechanical Drawings

These drawings have been generated with AutoDesk Inventor 2019 under a student license by the author. They are intended to provide insight into the design characteristics of SiECA and supporting hardware. Brief descriptions are provided however the main text will provide substantially better information concerning the use and significance of each component shown here.

**Table A.1:** Modifications not shown in Technical Drawings

<a href="#">A.2</a> , <a href="#">A.3</a> , <a href="#">A.4</a>	Slot for DAQ/Mezz frame rounded corners for easier assembly.
<a href="#">A.5</a>	Inserted corners rounded to match Si-EC frame rounded corners.

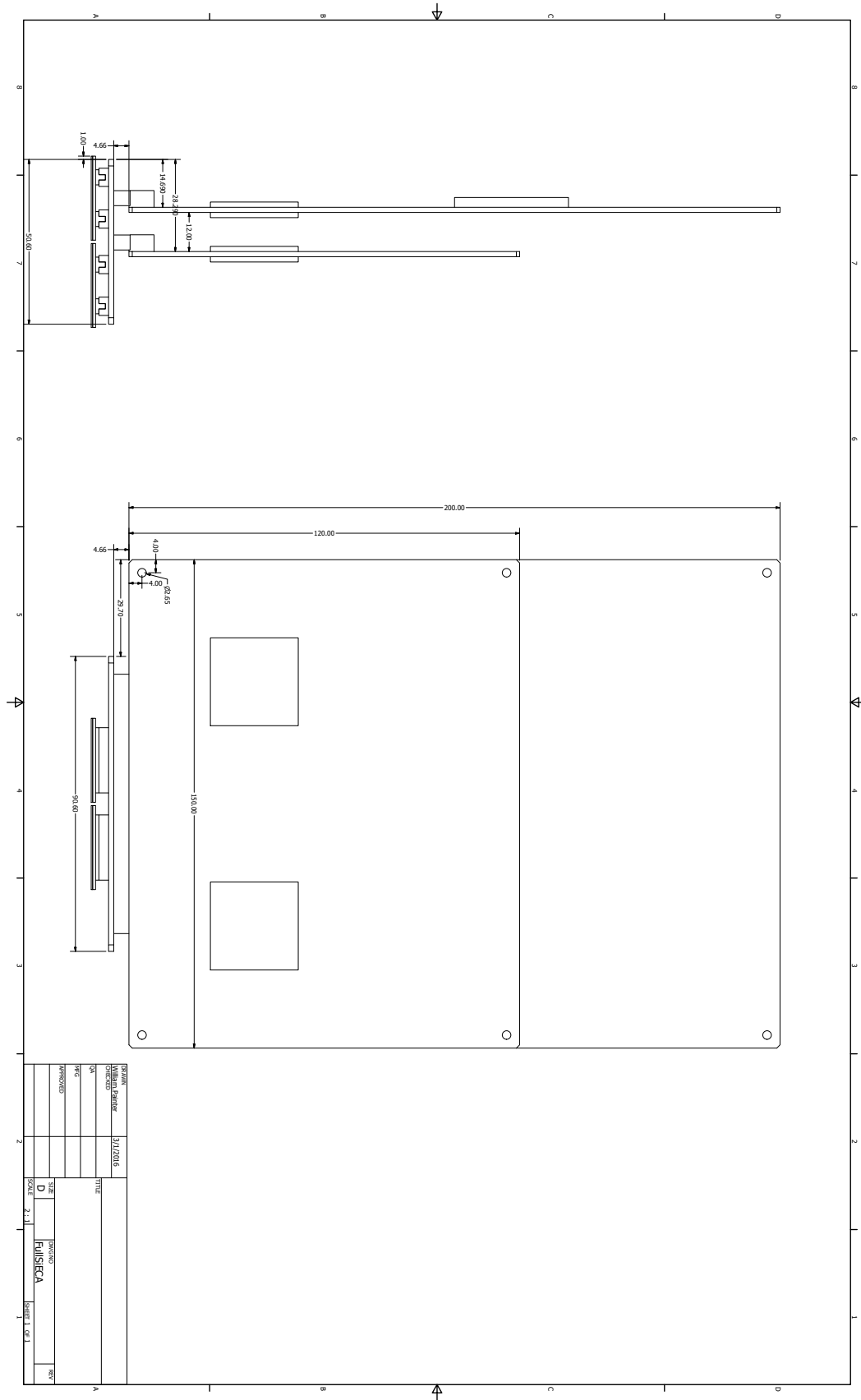


Figure A.1: SiECA Si-EC, DAQ and Mezz PCBs connected with frames omitted

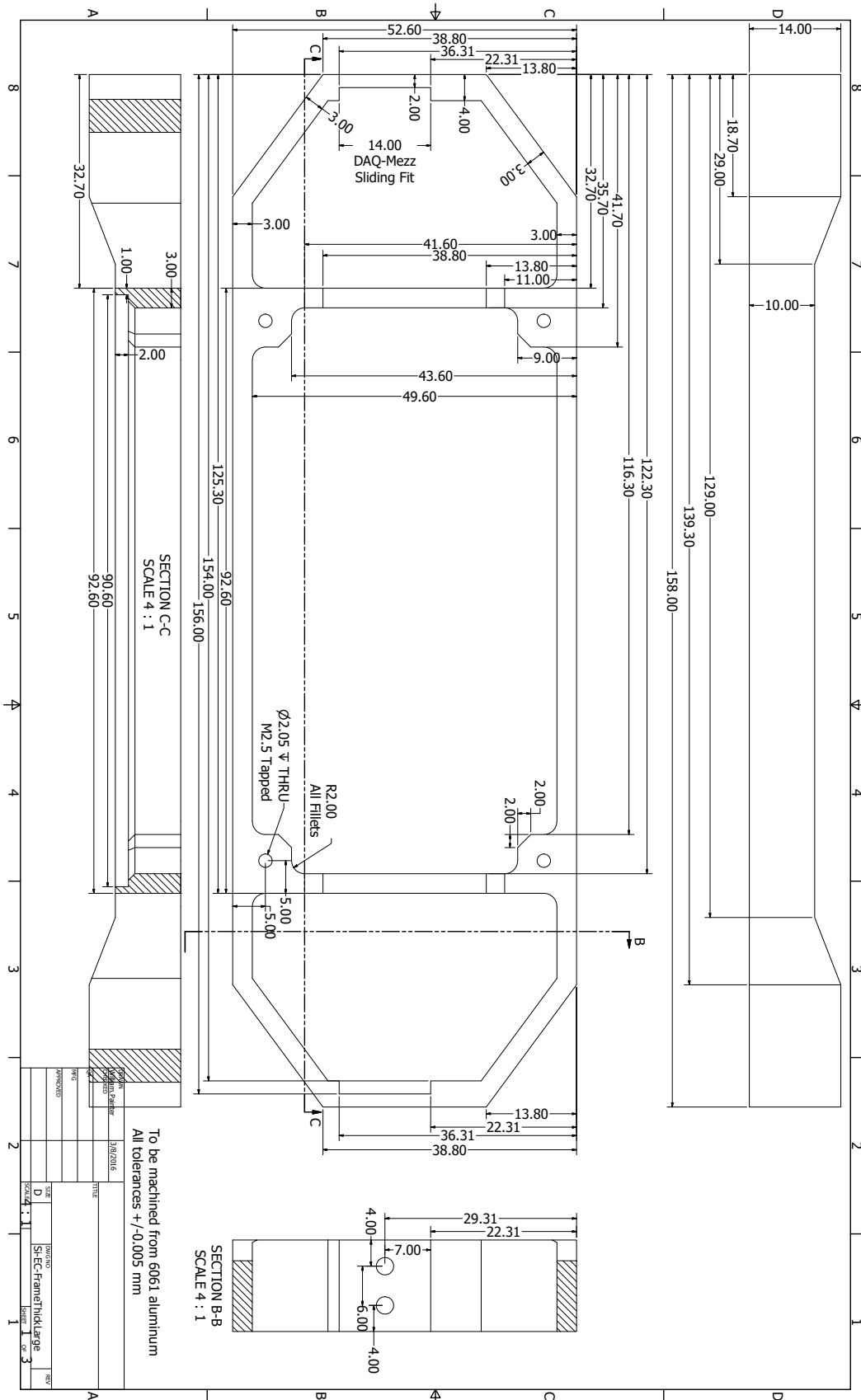


Figure A.2: SiECA Si-EC aluminum frame

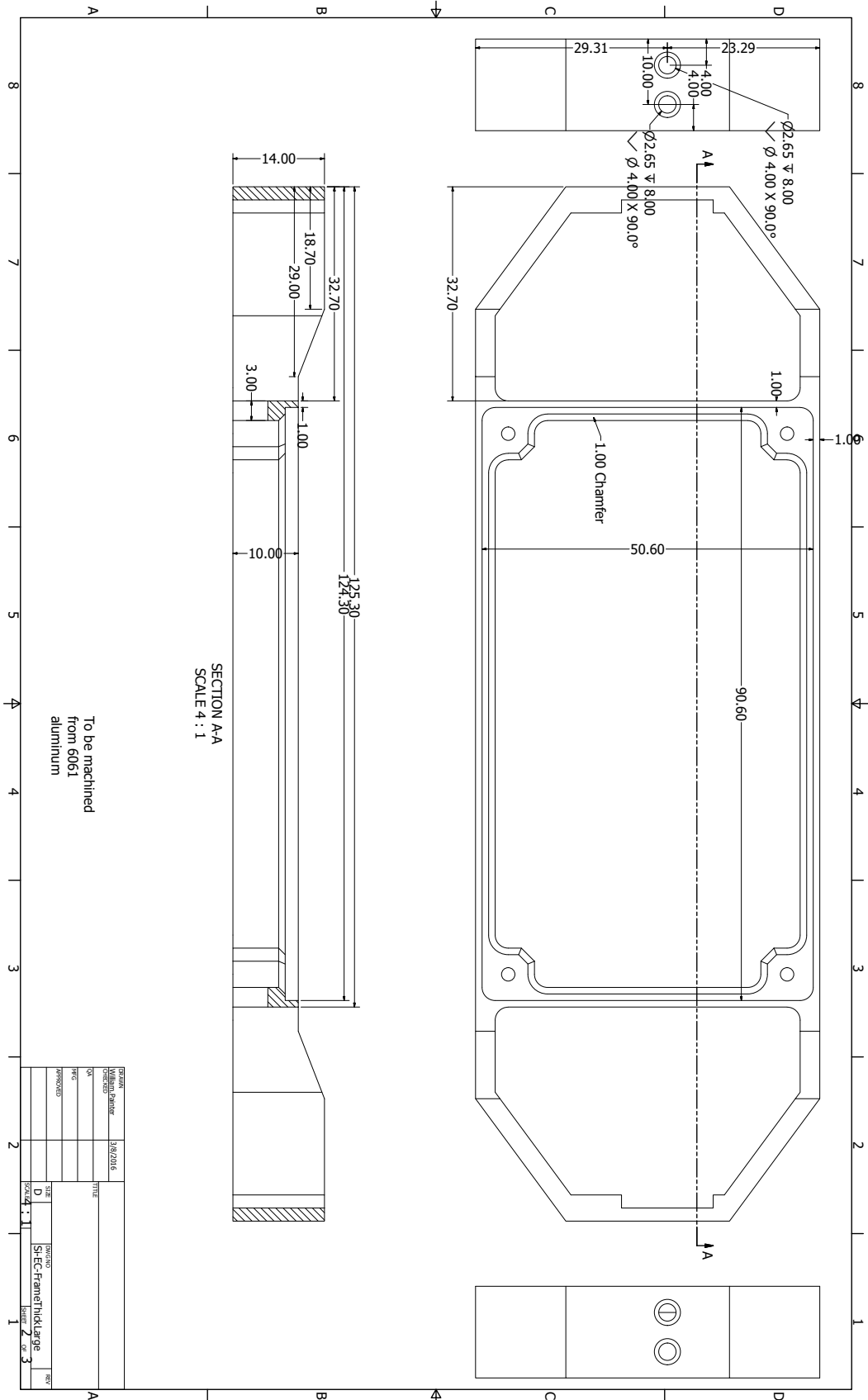


Figure A.3: SiECA Si-EC aluminum frame

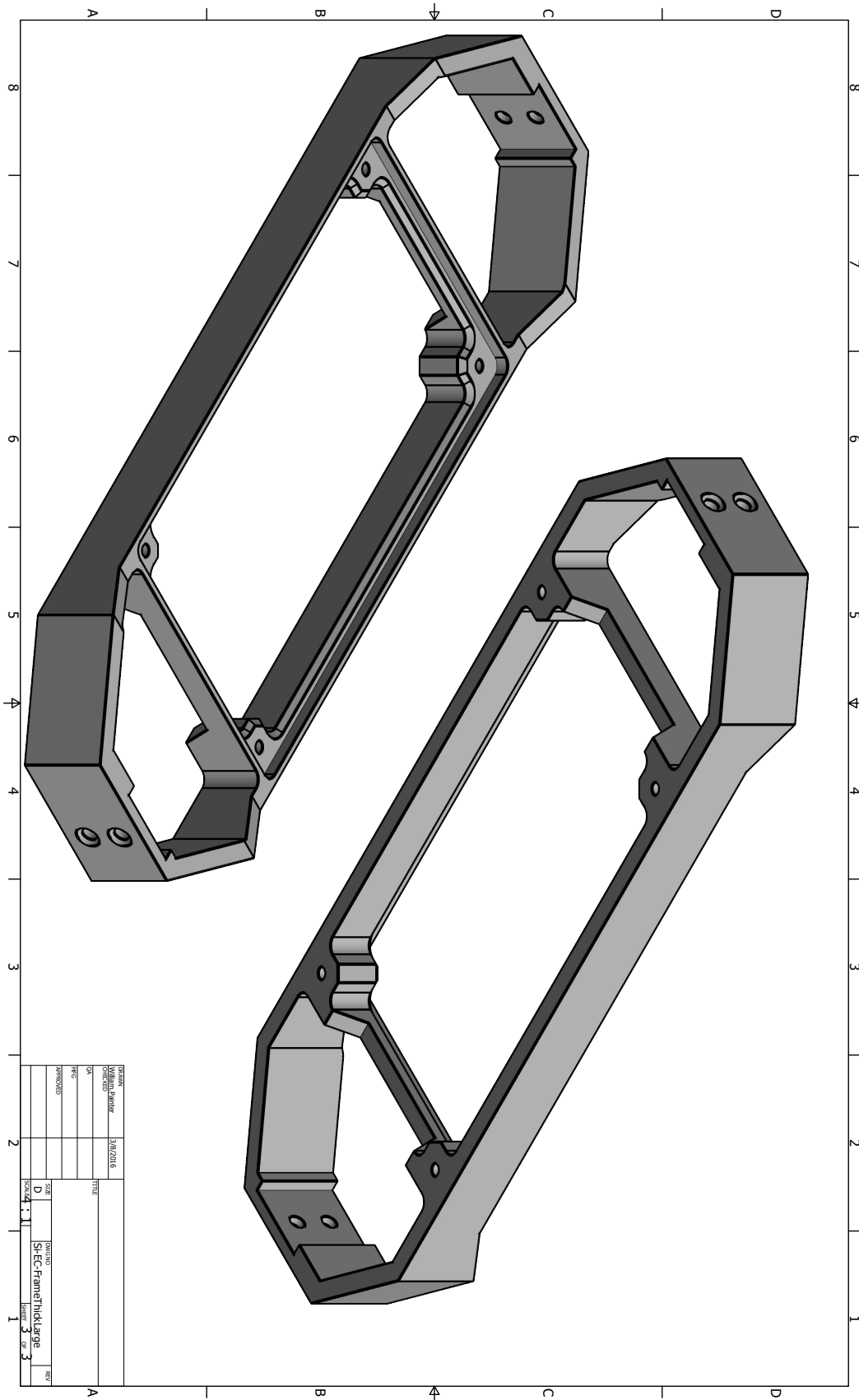


Figure A.4: SiECA Si-EC aluminum frame

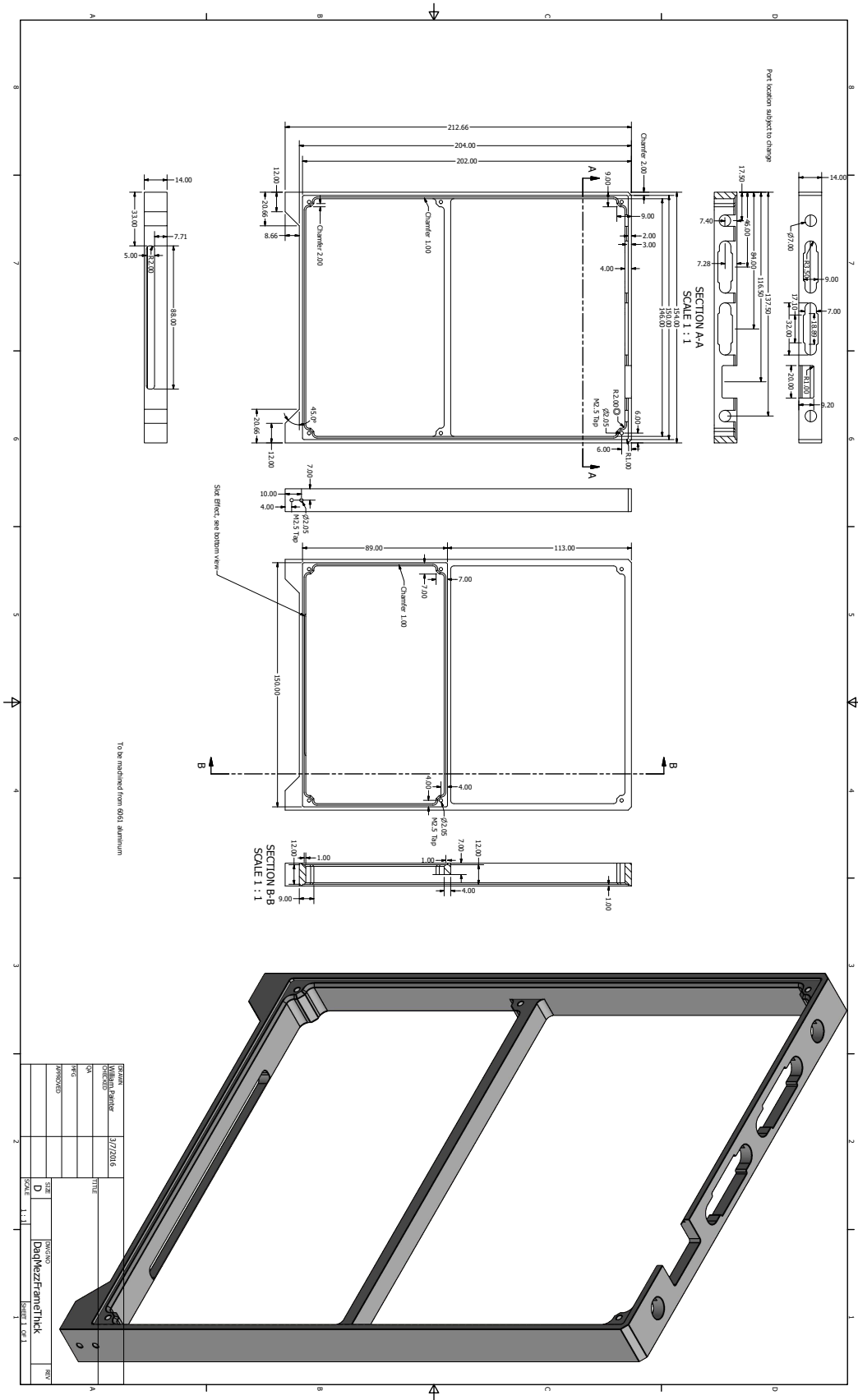


Figure A.5: SiECA DAQ and Mezz aluminum frame



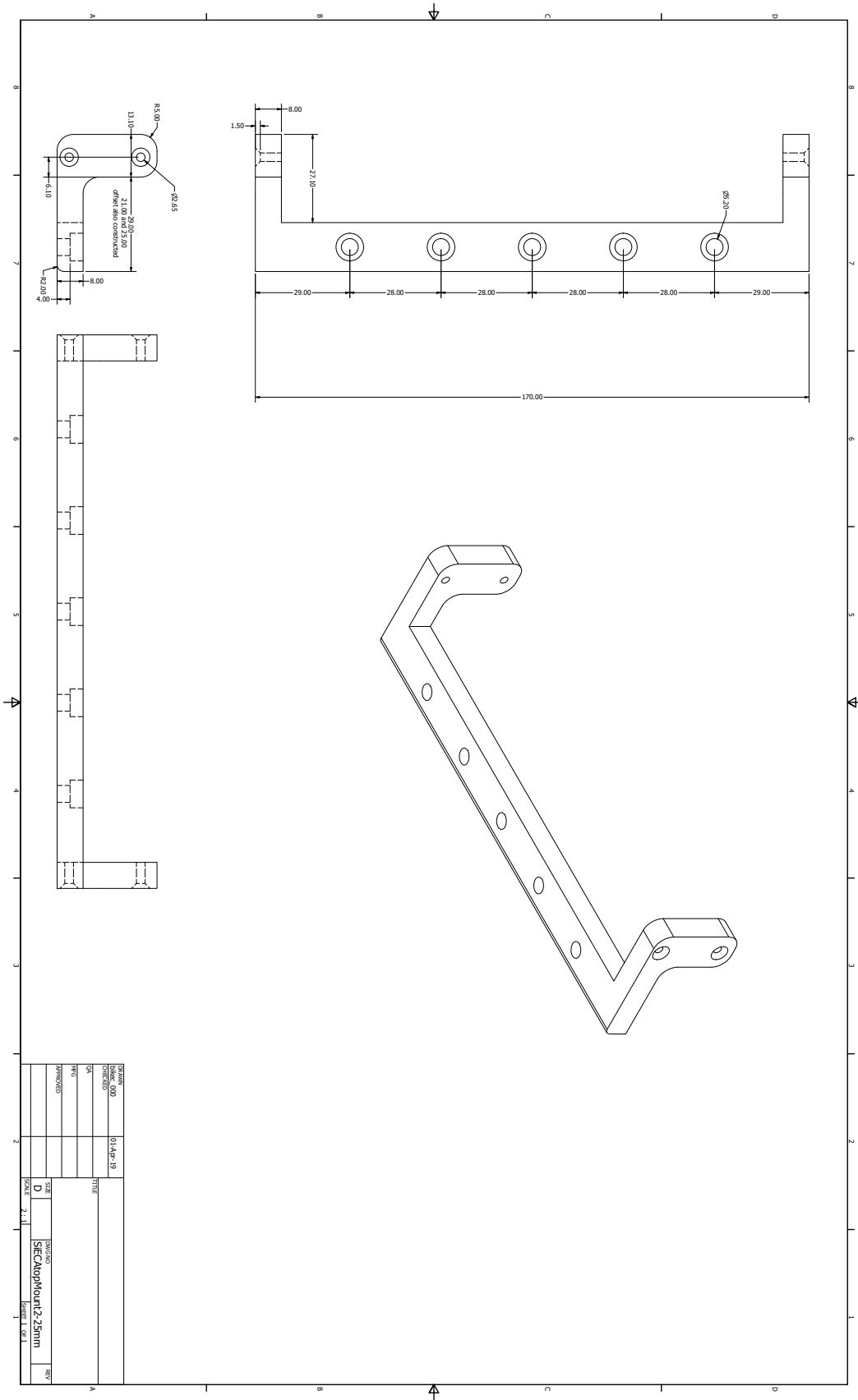


Figure A.7: Square mounting bracket for attaching SiECA to a flat EUSO-PDM

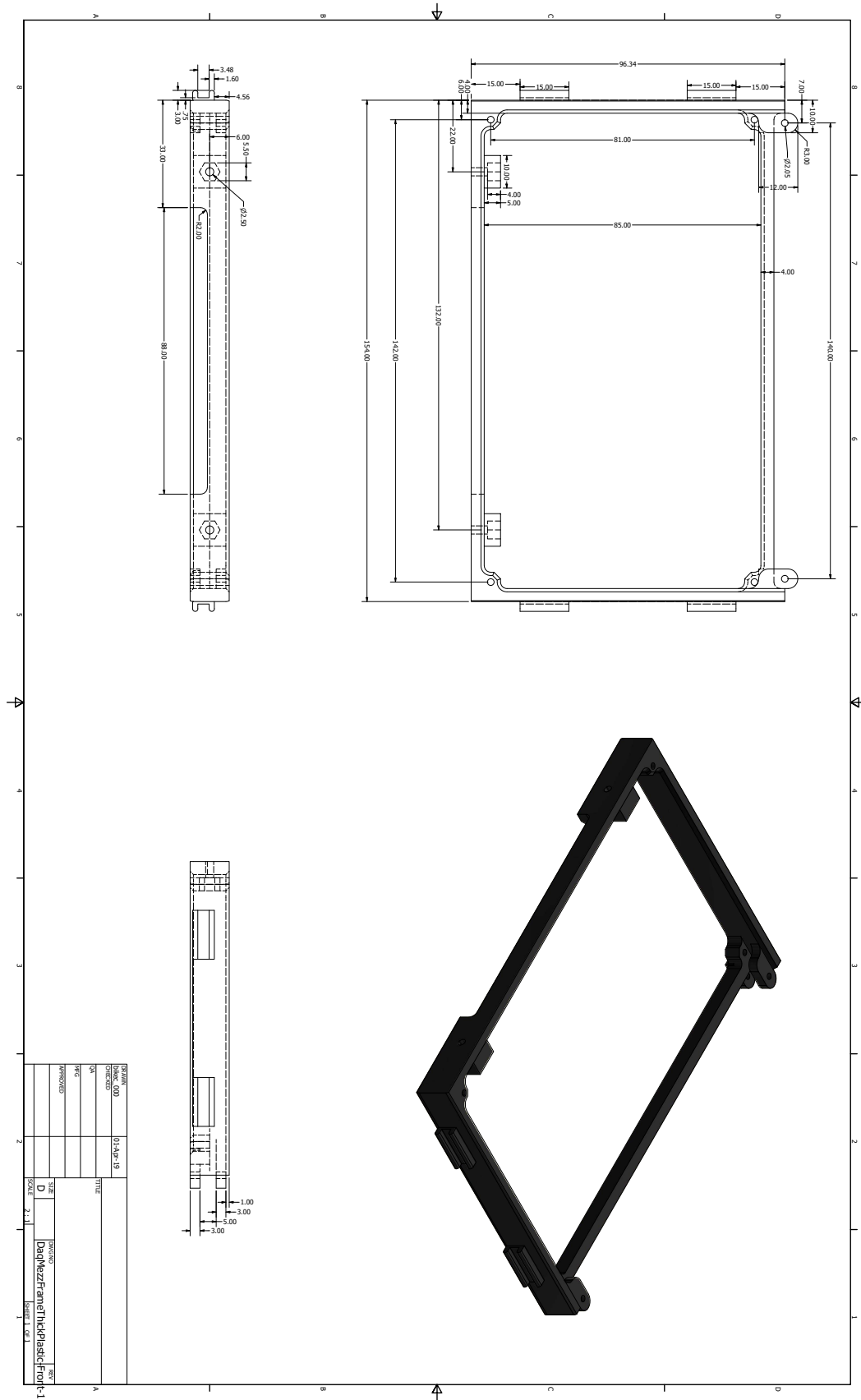


Figure A.8: SiECA DAQ and Mezz 3D printed front half



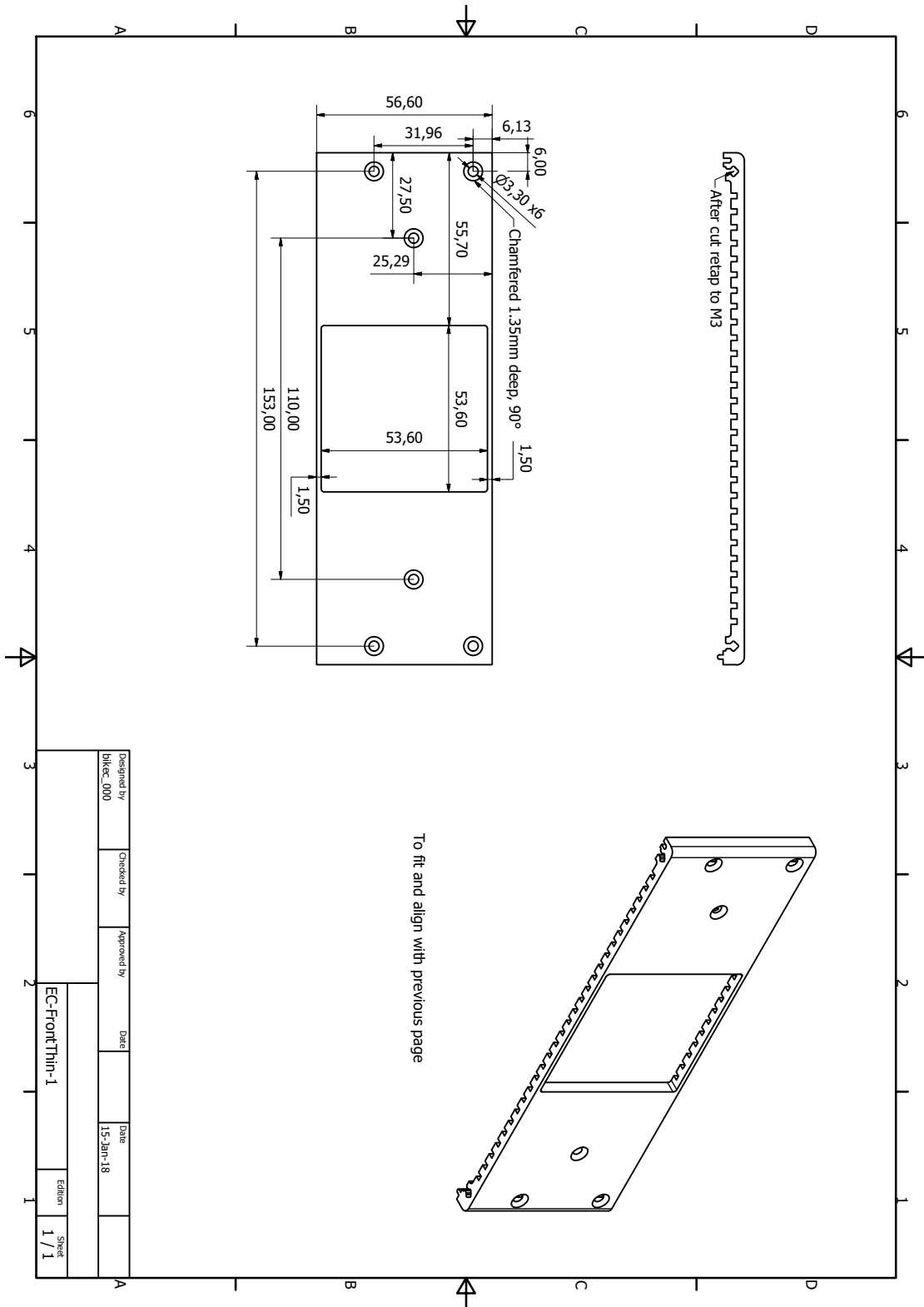


Figure A.10: SiECA Si-EC enclosure front with cutout for sensors

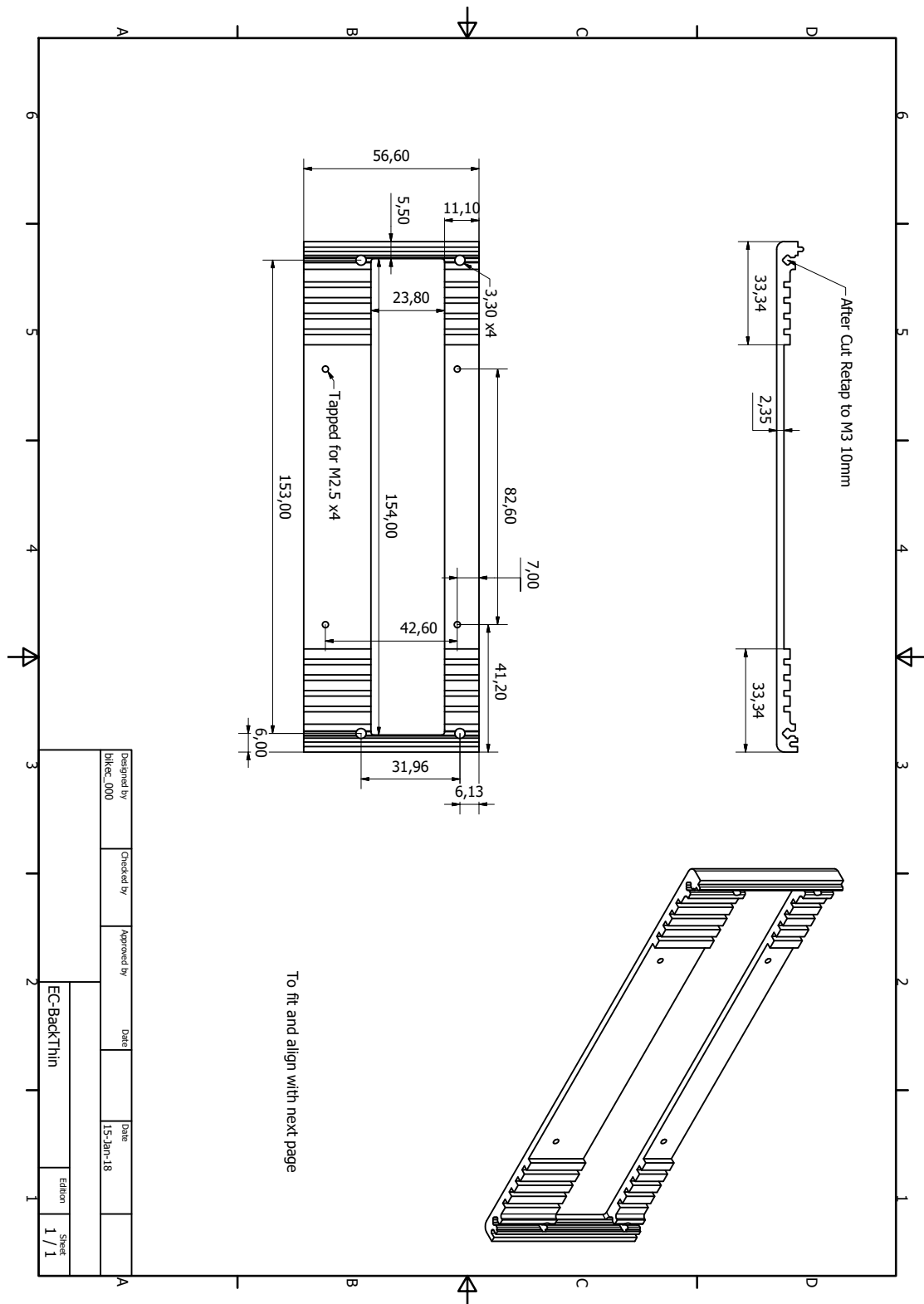


Figure A.11: SiECA Si-EC enclosure back with cutout for connection to DAQ and Mezz. Si-EC board secured with isolated brass bolts

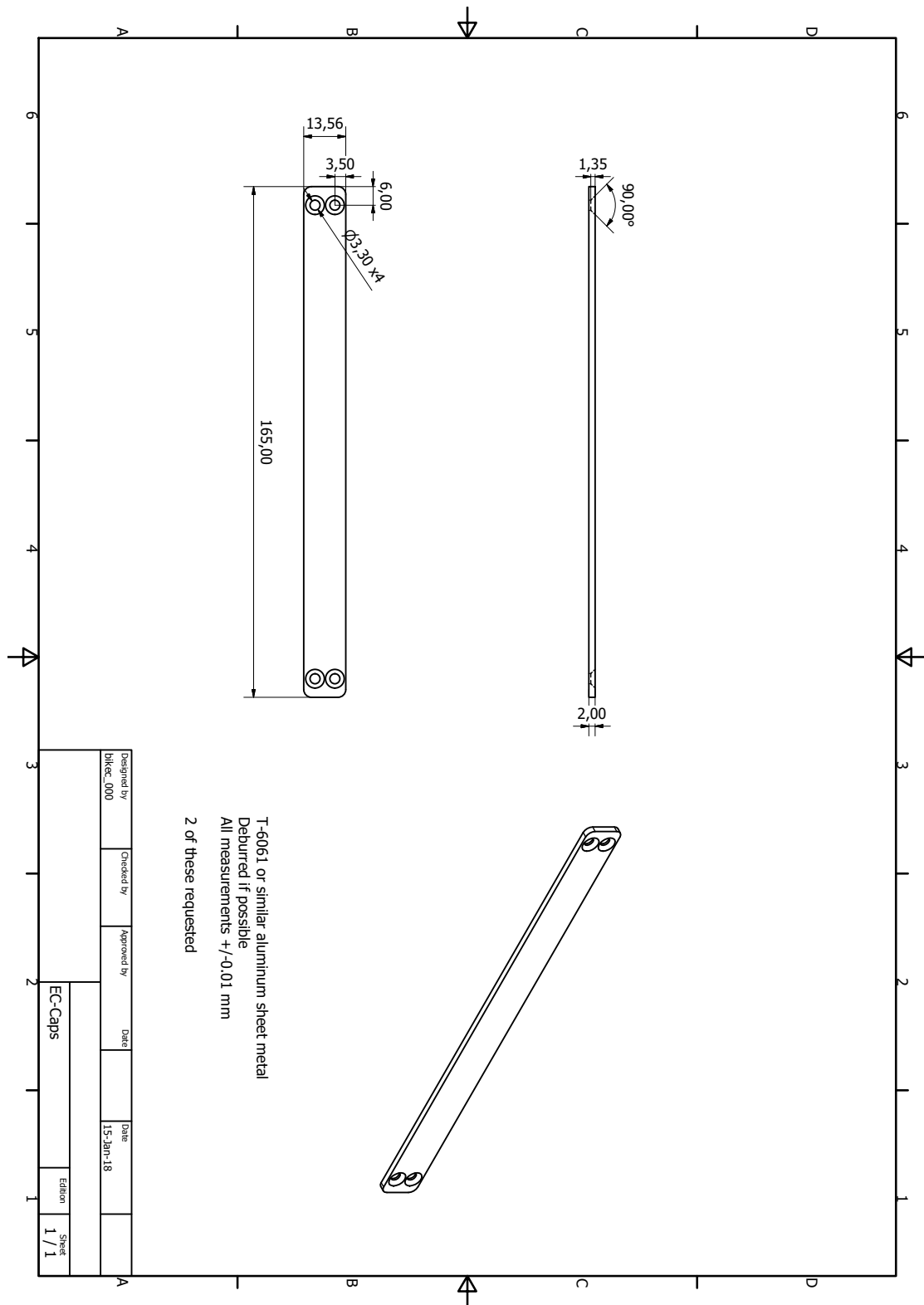


Figure A.12: SiECA Si-EC enclosure top and bottom plates

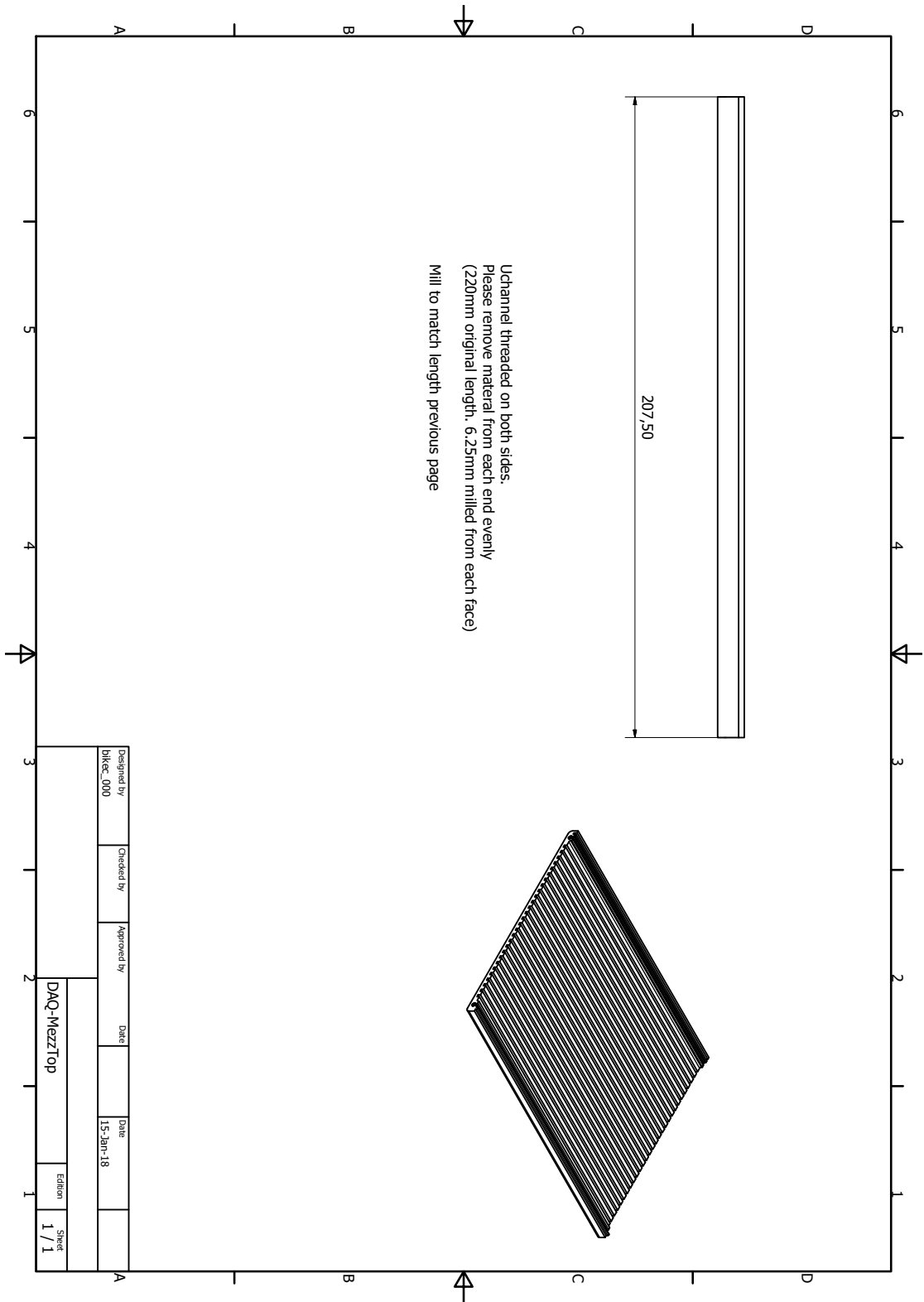


Figure A.13: SiECA DAQ and Mezz enclosure top

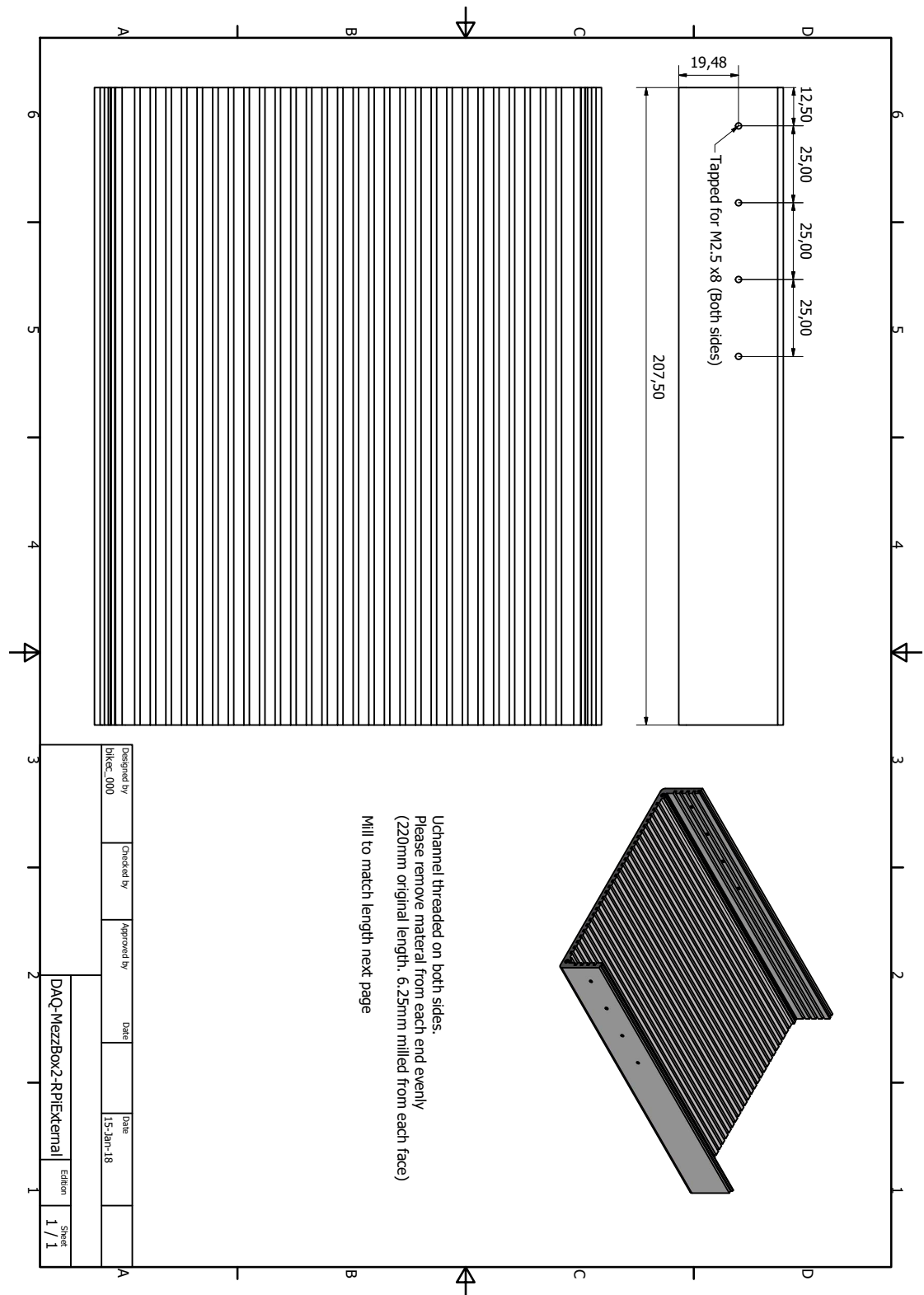


Figure A.14: SiECA DAQ and Mezz enclosure bottom with holes for mounting attachment system

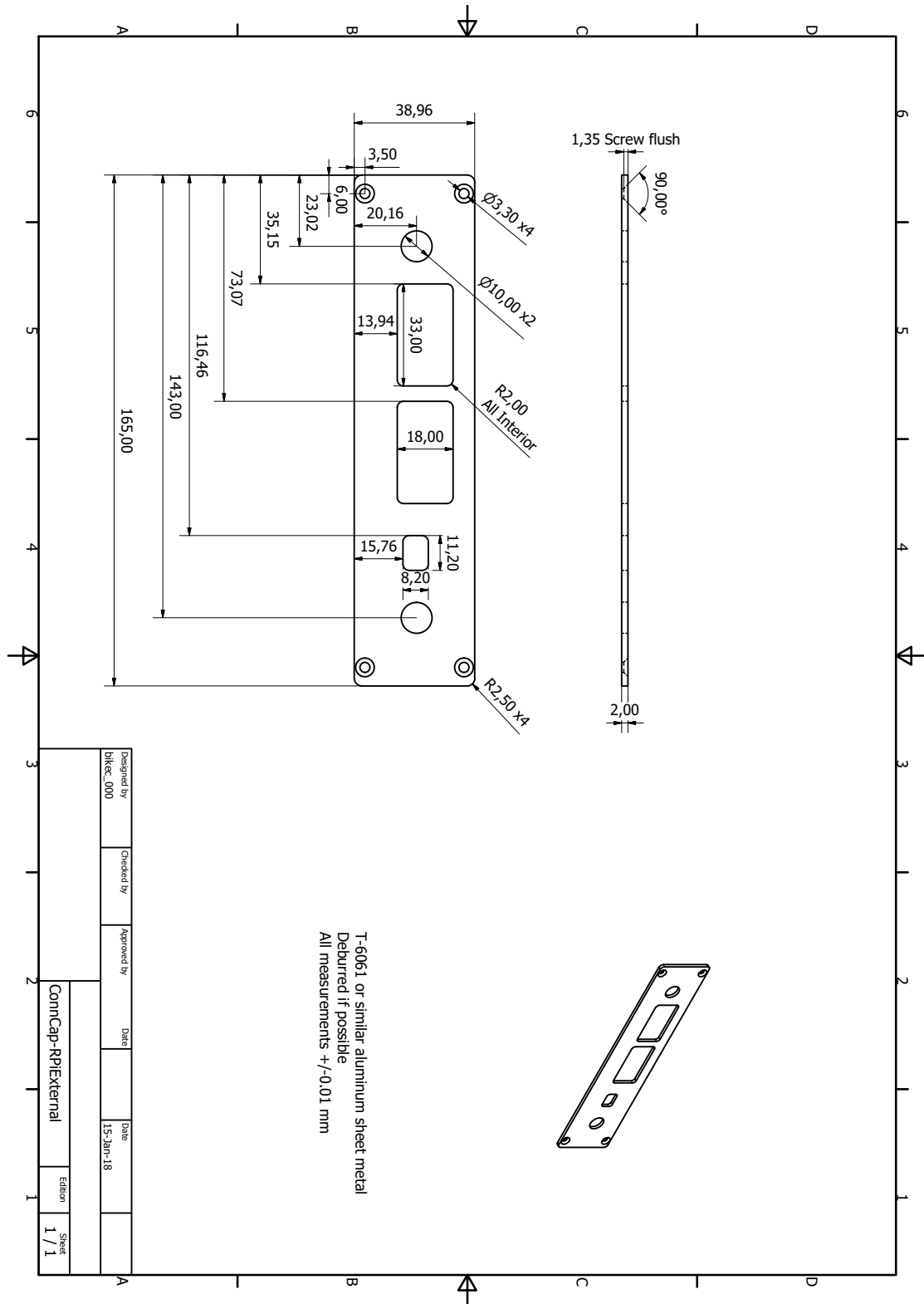


Figure A.15: SiECA DAQ and Mezz enclosure back plate with ports for connections

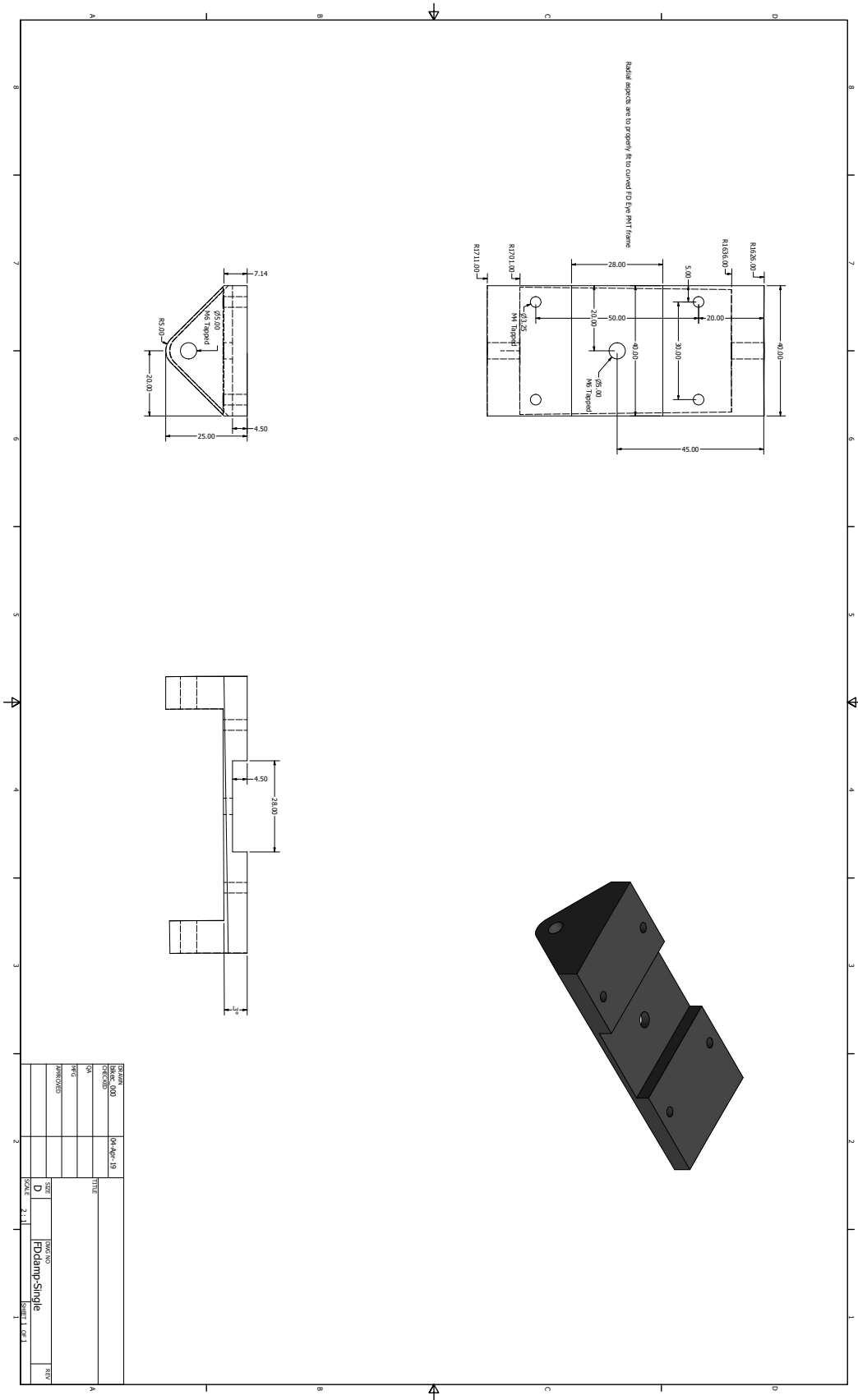
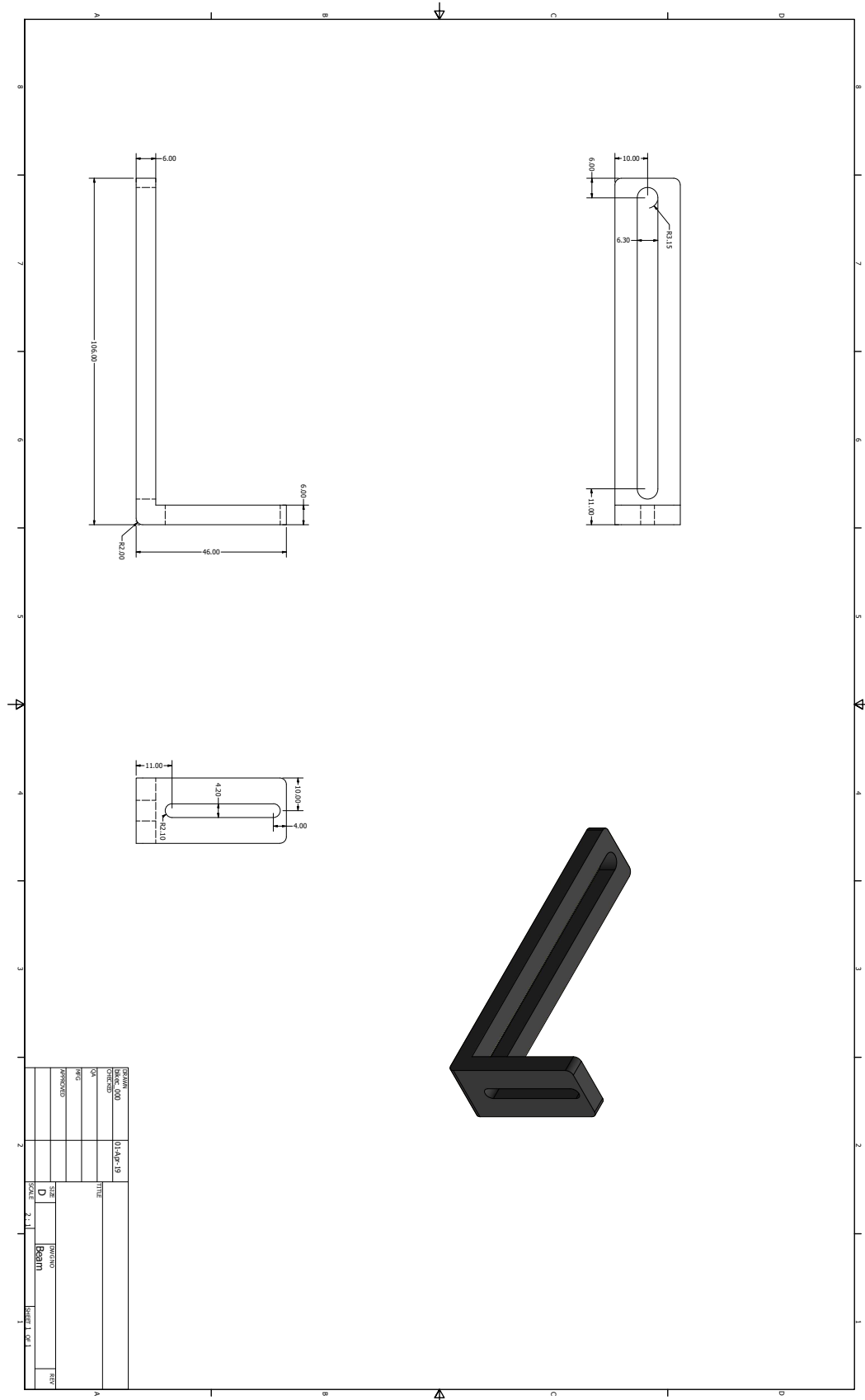
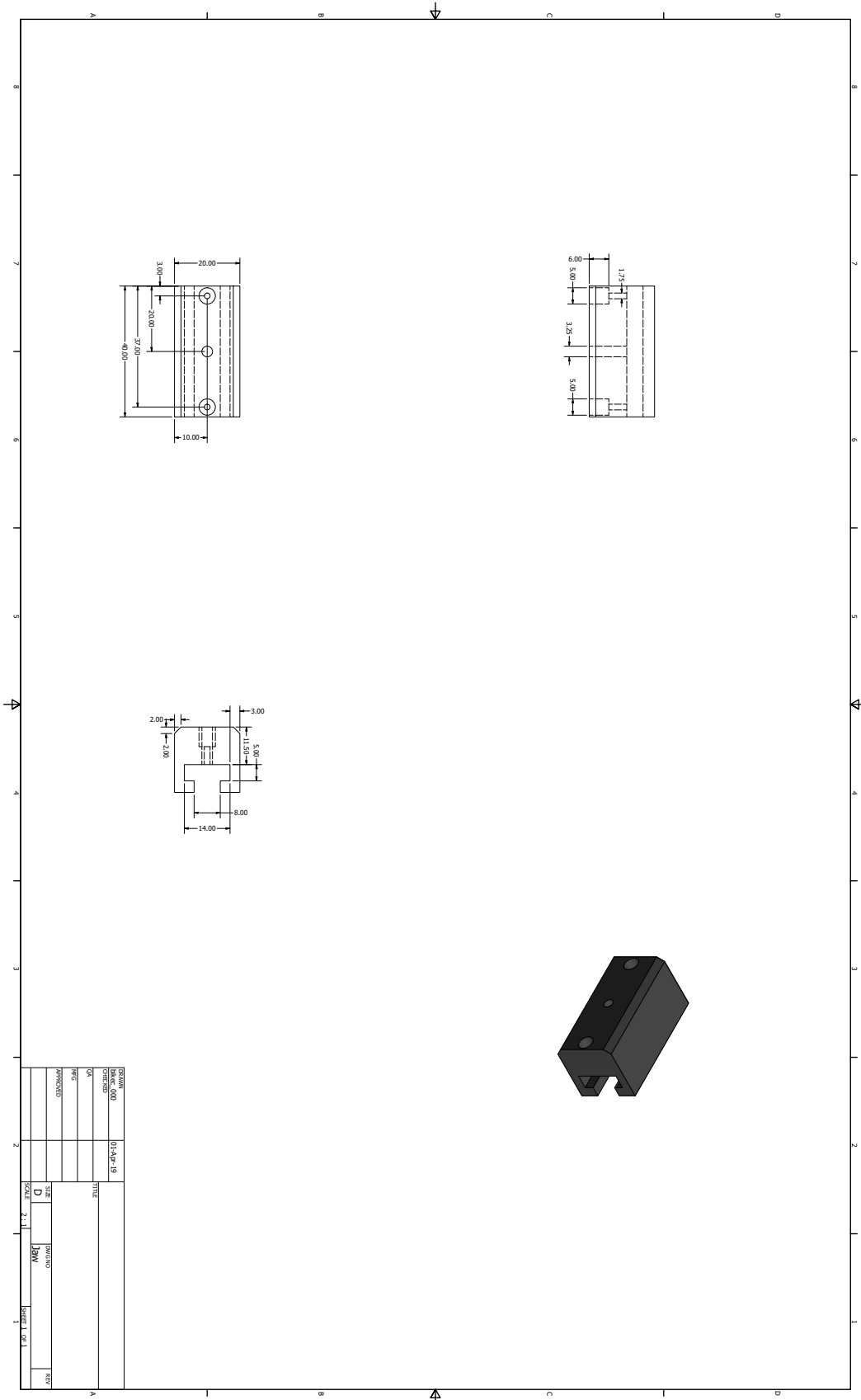


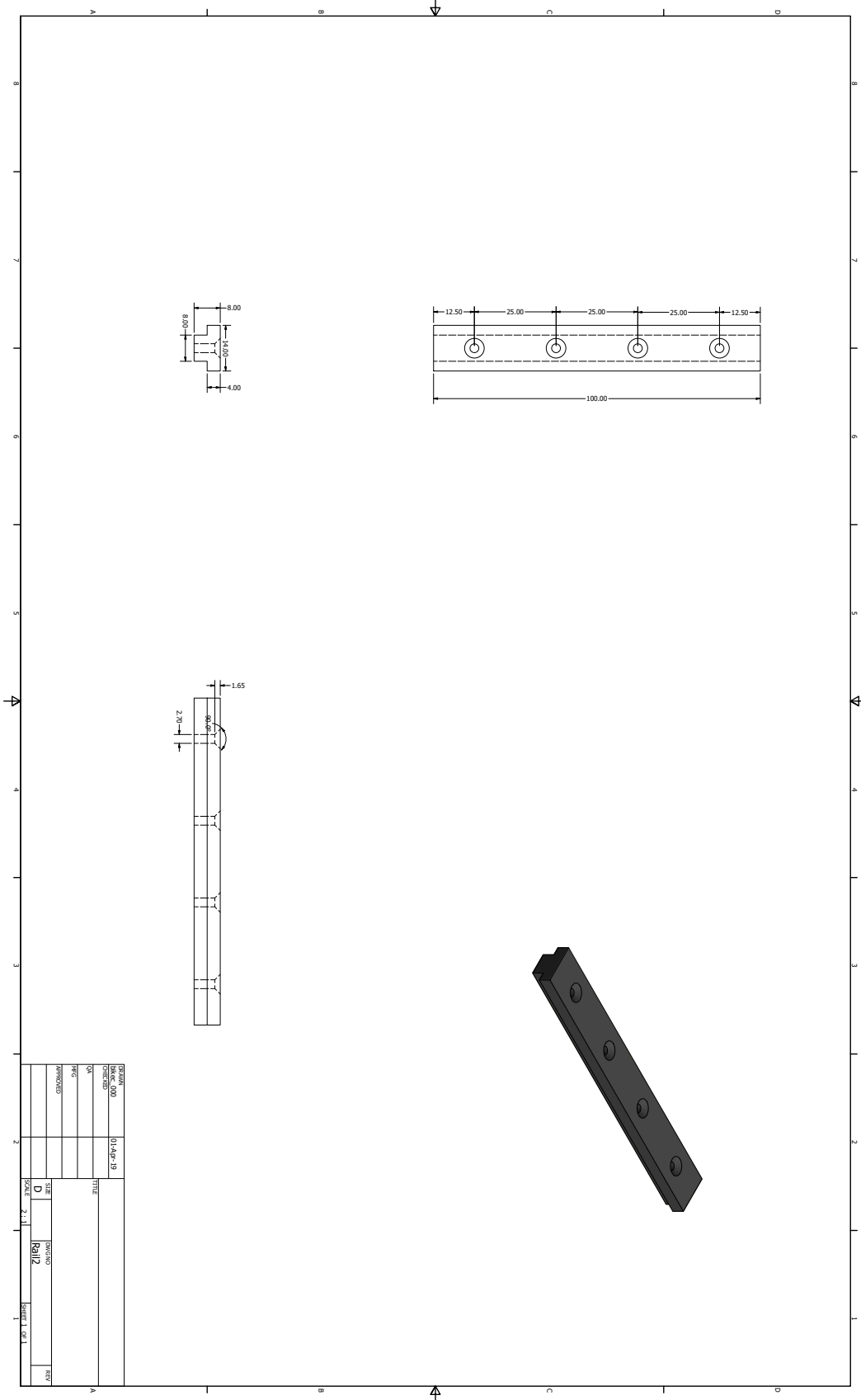
Figure A.16: SiECA DAQ and Mezz enclosure back plate with ports for connections



**Figure A.17:** Beam connecting FD Eye Clamp to SiECA Jaw clamp. Allows for centering and vertical adjustment of SiECA in relation to Mercedes stars and PMTs of FD Eye



**Figure A.18:** Jaw connects to Beam and clamps on Rail allowing for rotational alignment along the securing bolt axis



## A.2 PCB Layout

Included here are the complete and internal layers of the Si-EC board. The DAQ and Mezz board layouts and routings are property of KIT-IPE and can be obtained by contacting Alexander Menshikov.

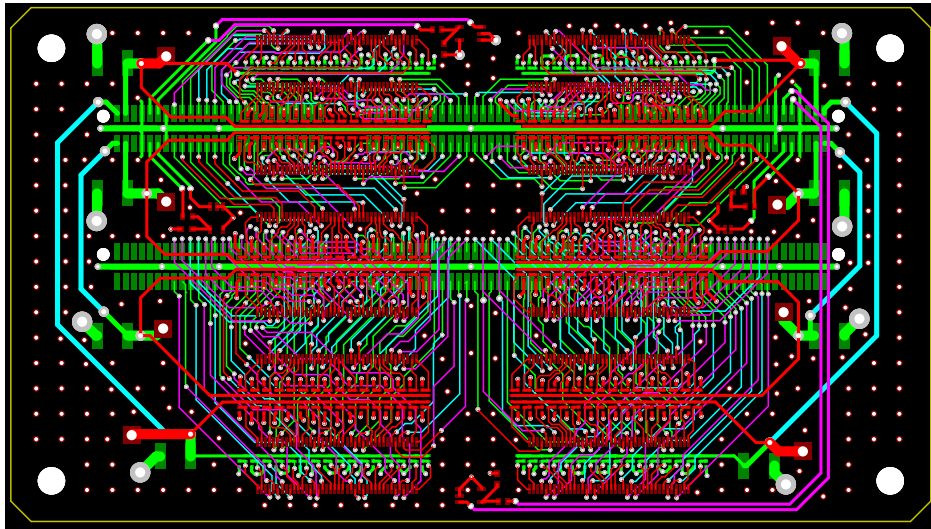


Figure A.20: Complete SiEC board

F.Cu: SiPM connectors, Temperature Sensors  
B.Cu: QRx8 connectors, Molex 8Pin, Capacitors

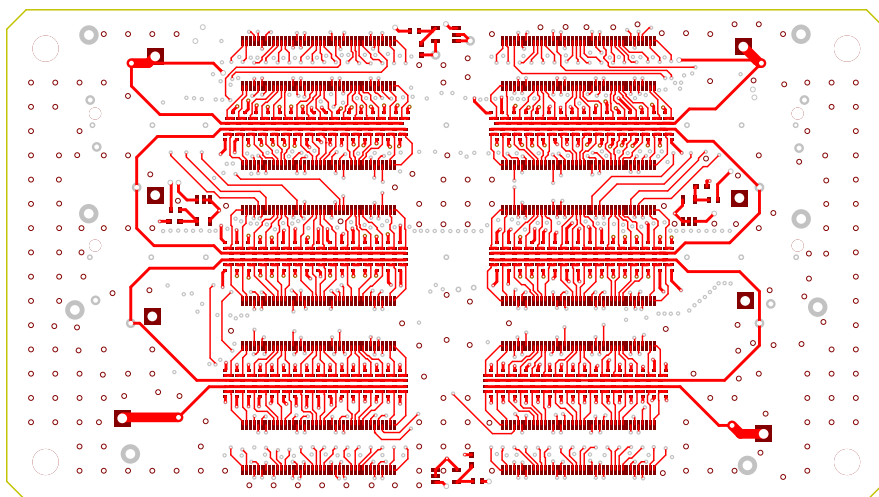


Figure A.21: SiEC board Front (sensor side)

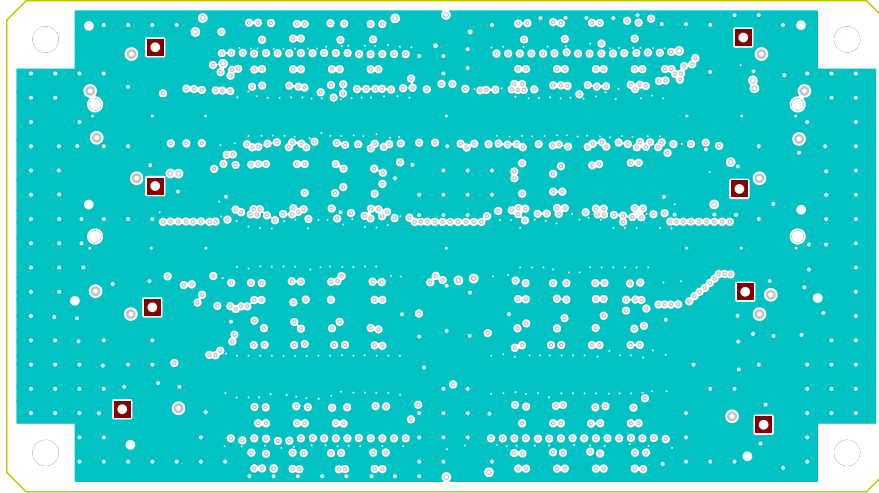


Figure A.22: SiEC Inner Layer 1

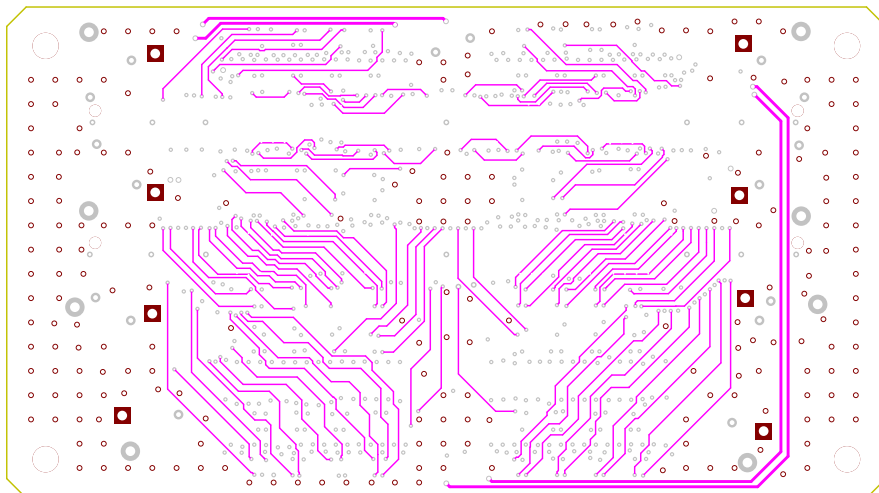


Figure A.23: SiEC Inner Layer 2

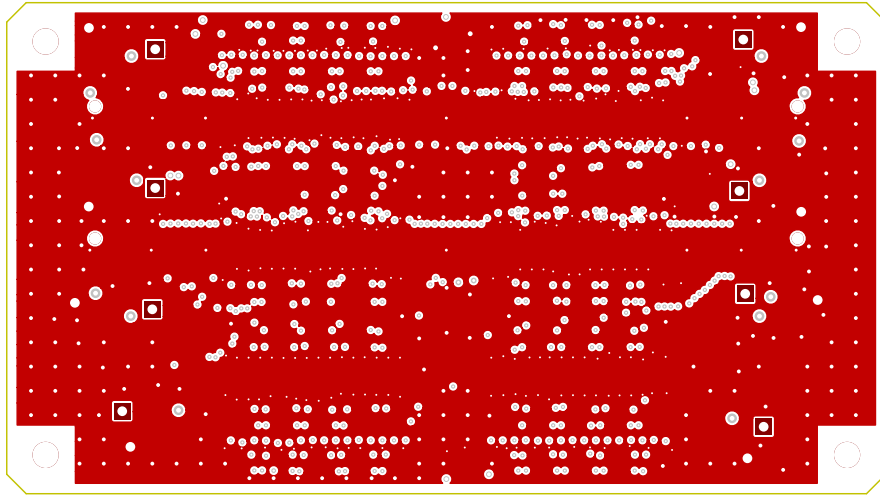


Figure A.24: SiEC Inner Layer 3

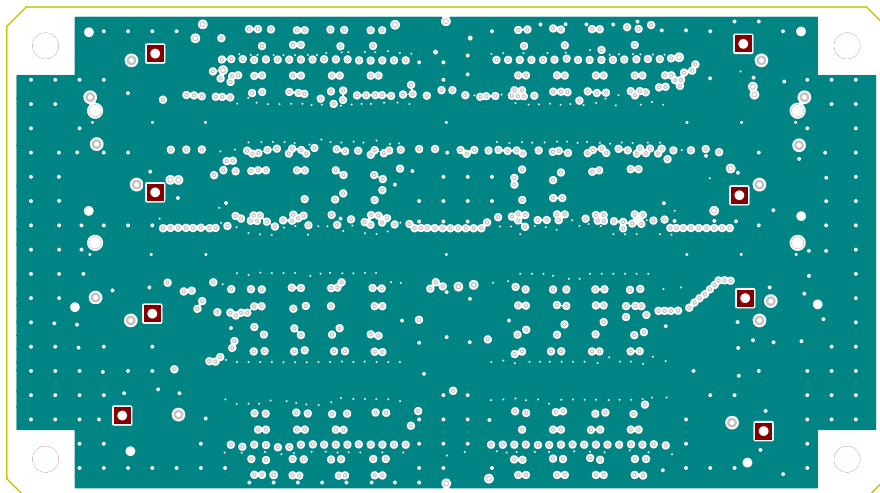


Figure A.25: SiEC Inner Layer 4

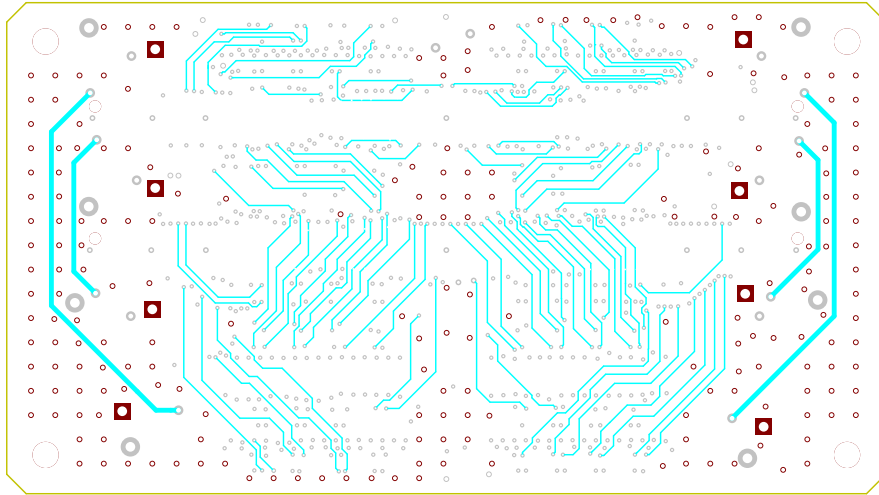


Figure A.26: SiEC Inner Layer 5

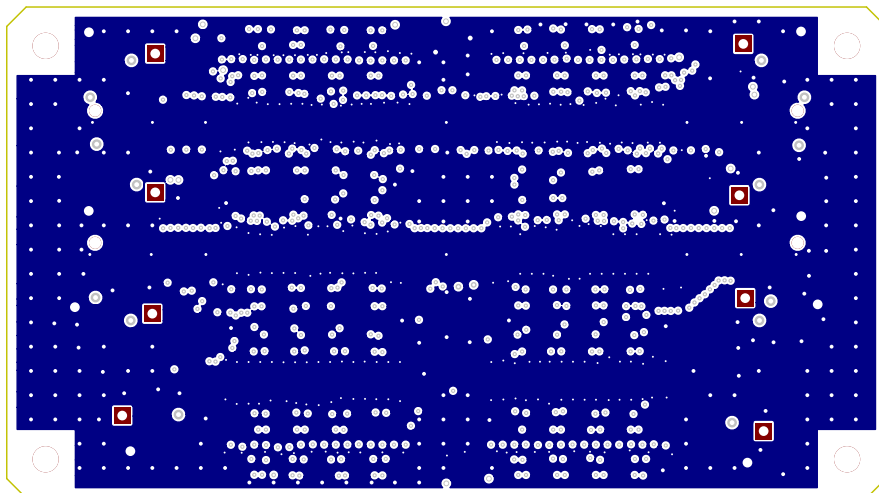


Figure A.27: SiEC Inner Layer 6

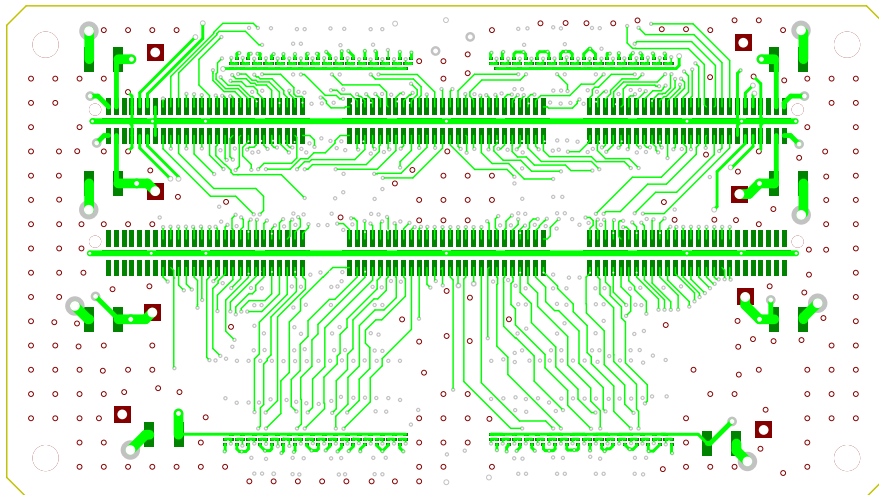


Figure A.28: SiEC board Bottom (DAQ/Mezz connector side)

### A.3 Citiroc Architecture

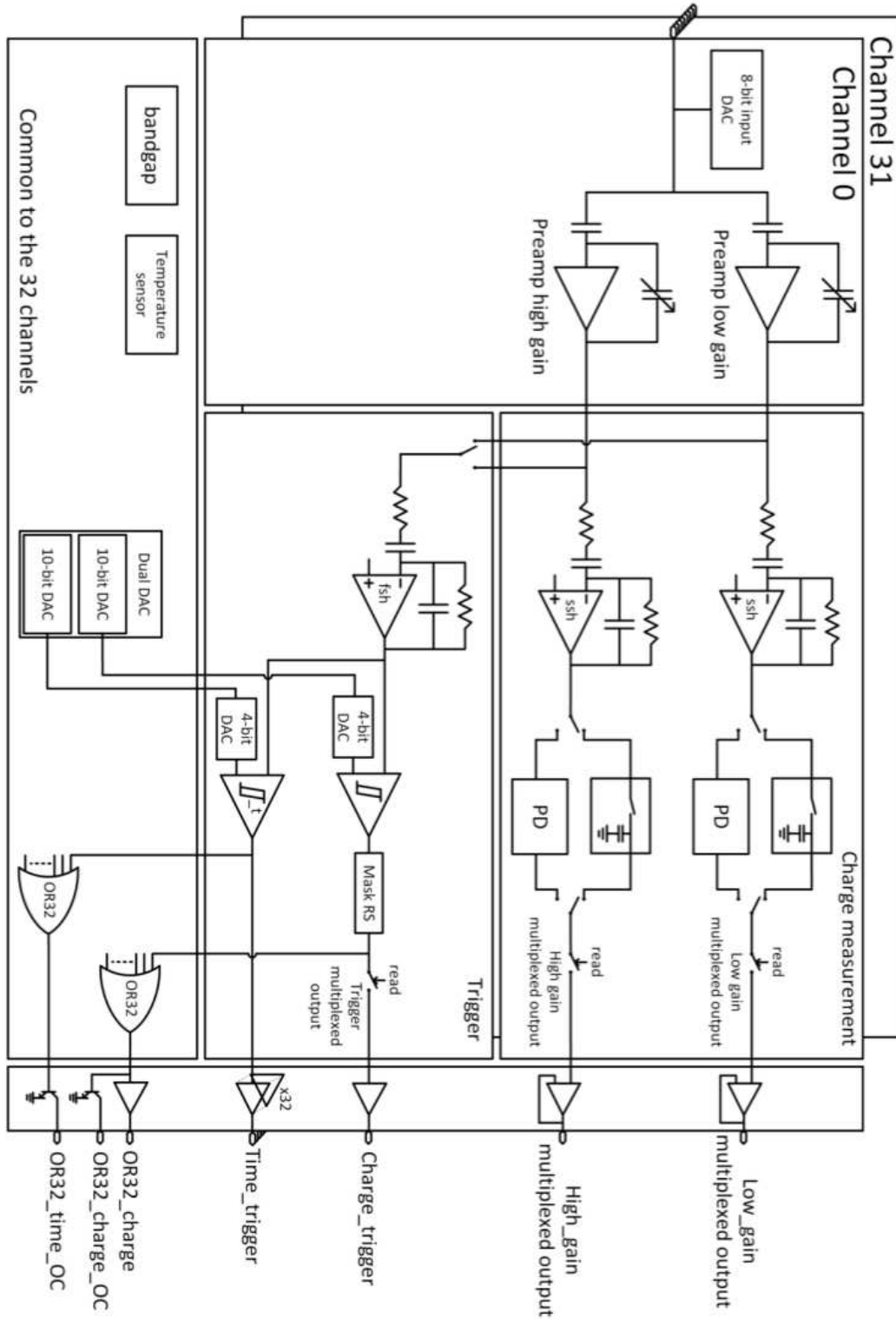


Figure A.29: Citiroc1A architecture

# APPENDIX B

## Appendix B: Plots

This appendix is meant to contain the plots shown in the thesis plus those for comparison that are not already shown. Hopefully, the relevant differences will be apparent and can be appreciated after reading the description and explanation presented in the main body of this work.

### B.1 Calibration Characteristic Plots

The combine plots in the main text are a bit convoluted. Here I include the plots separated so the reader can make a better assessment of the impact of flat fielding. The first, and colorful, plot is the same combined plot in the main text for comparison.

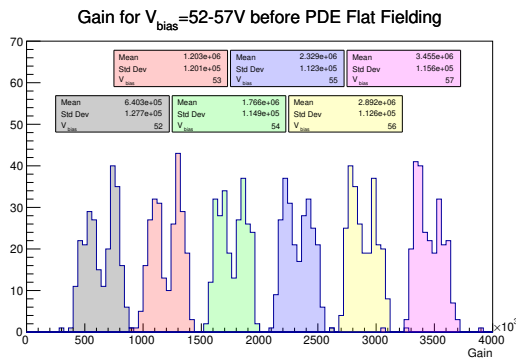


**Figure B.1:** Distribution of Gain for indicated  $V_{bias}$  before PDE Flat Fielding

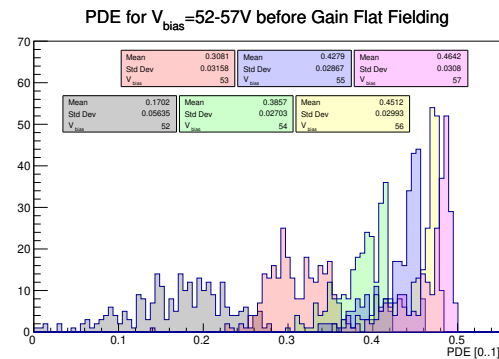


**Figure B.2:** Distribution of PDE for indicated  $V_{bias}$  before Gain Flat Fielding

### B.1.1 Gain before Flat Fielding at given Bias Voltage

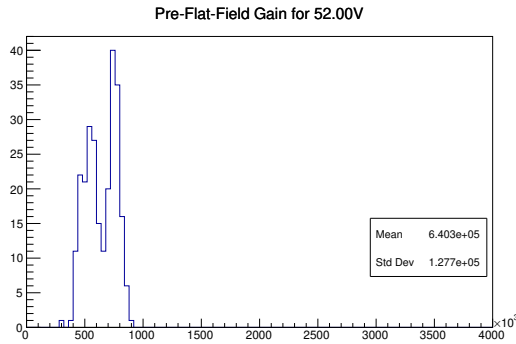


**Figure B.3:** Distribution of Gain at  $V_{bias} = 52.00$  V before PDE Flat Fielding

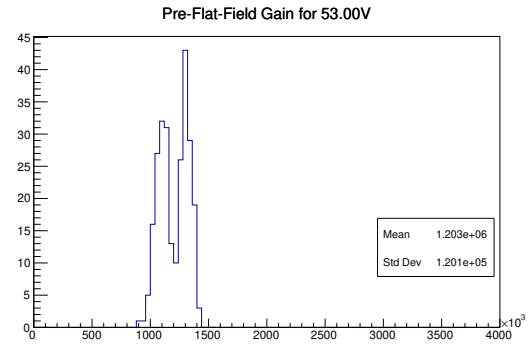


**Figure B.4:** Distribution of Gain at  $V_{bias} = 53.00$  V before PDE Flat Fielding

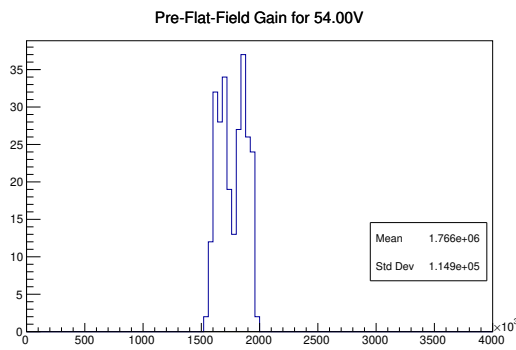


**Figure B.5:** Distribution of Gain at  $V_{bias} = 54.00$  V before PDE Flat Fielding

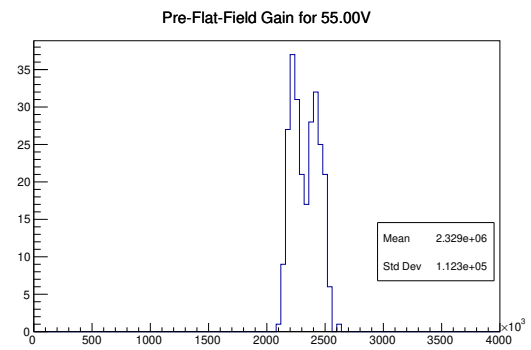


**Figure B.6:** Distribution of Gain at  $V_{bias} = 55.00$  V before PDE Flat Fielding

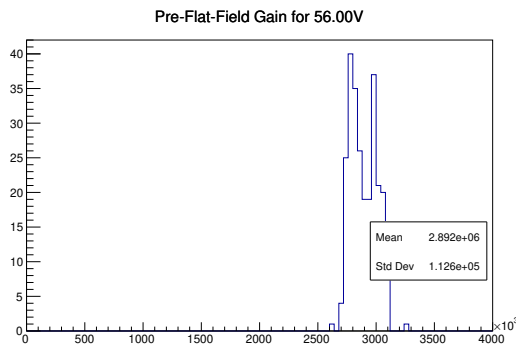


**Figure B.7:** Distribution of Gain at  $V_{bias} = 56.00$  V before PDE Flat Fielding

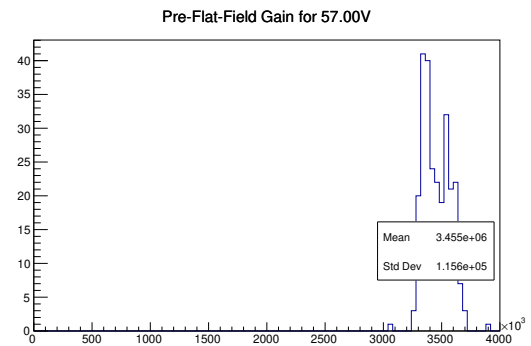


**Figure B.8:** Distribution of Gain at  $V_{bias} = 57.00$  V before PDE Flat Fielding

**B.1.2 PDE before Flat Fielding at given Bias Voltage**

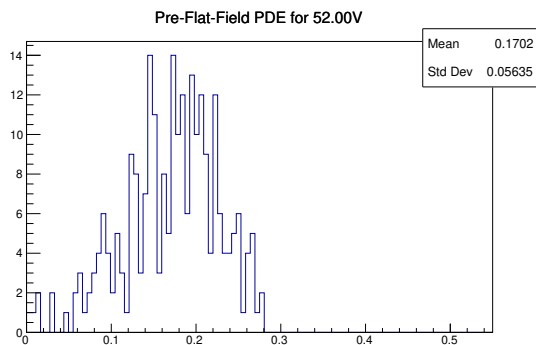


**Figure B.9:** Distribution of PDE at  $V_{bias} = 52.00$  V before Gain Flat Fielding

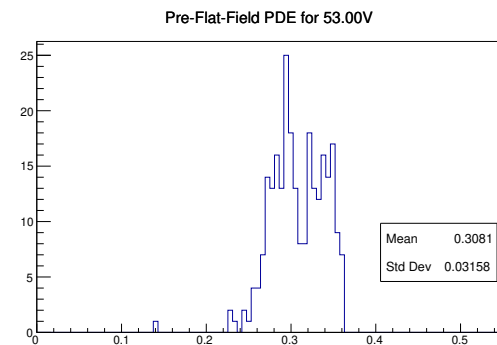


**Figure B.10:** Distribution of PDE at  $V_{bias} = 53.00$  V before Gain Flat Fielding

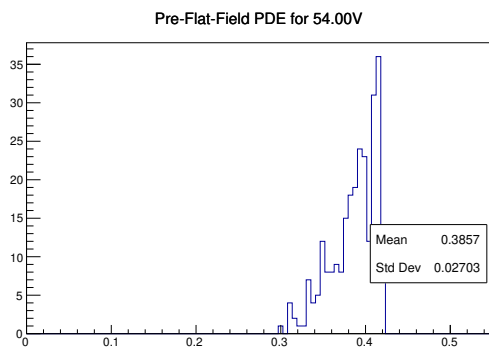


**Figure B.11:** Distribution of PDE at  $V_{bias} = 54.00$  V before Gain Flat Fielding

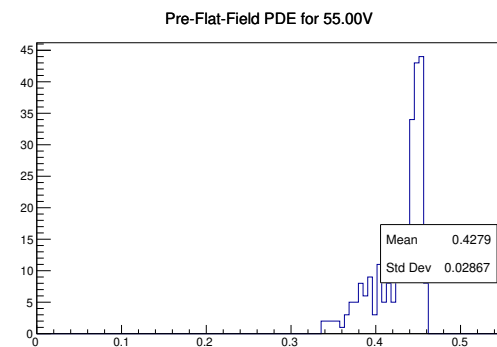


**Figure B.12:** Distribution of PDE at  $V_{bias} = 55.00$  V before Gain Flat Fielding

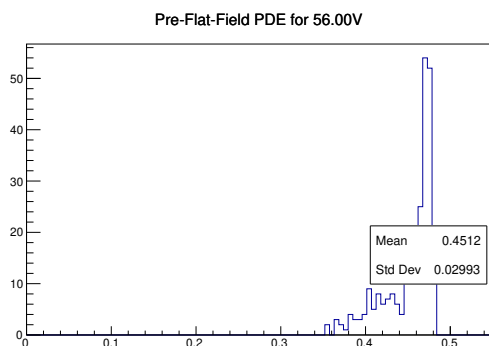


**Figure B.13:** Distribution of PDE at  $V_{bias} = 56.00$  V before Gain Flat Fielding

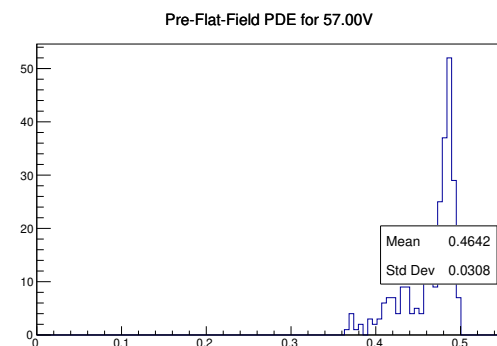


**Figure B.14:** Distribution of PDE at  $V_{bias} = 57.00$  V before Gain Flat Fielding

Now the post flat fielding combined plots, as shown in the main text but also here for comparison.

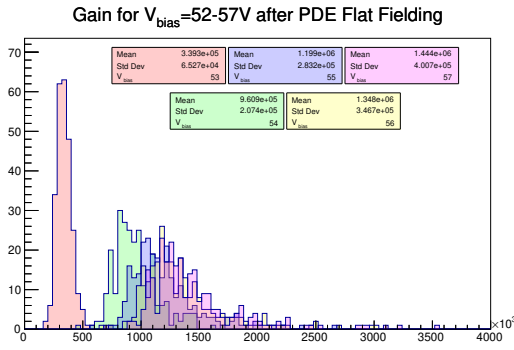


Figure B.15: Distribution of Gain for indicated  $V_{bias}$  after PDE Flat Fielding

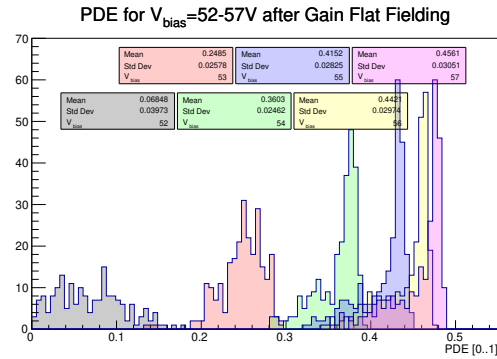


Figure B.16: Distribution of PDE for indicated  $V_{bias}$  after Gain Flat Fielding

### B.1.3 Gain after PDE Flat Fielding at given Bias Voltage

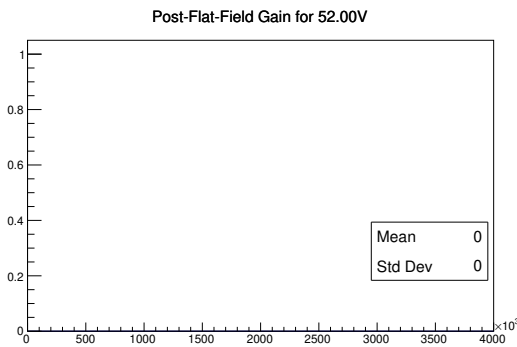


Figure B.17: At  $V_{bias} = 52.00$  V, at least one channel has a PDE of zero

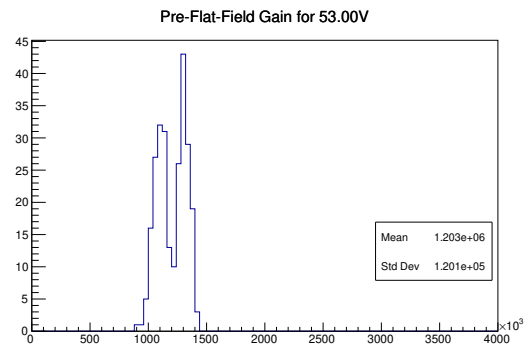


Figure B.18: Distribution of Gain at  $V_{bias} = 53.00$  V after PDE Flat Fielding

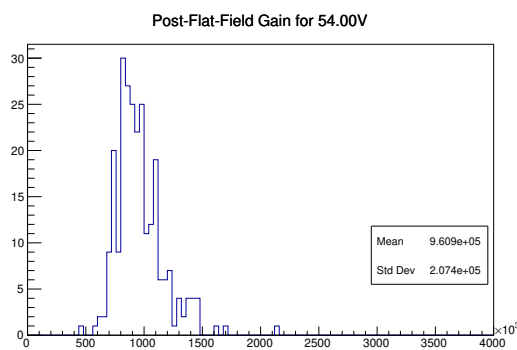


Figure B.19: Distribution of Gain at  $V_{bias} = 54.00$  V after PDE Flat Fielding

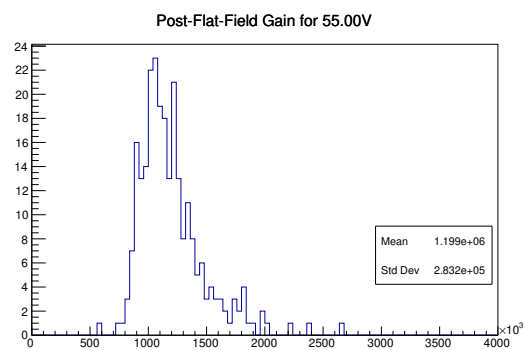
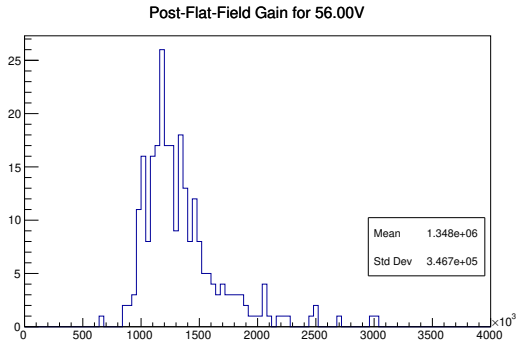
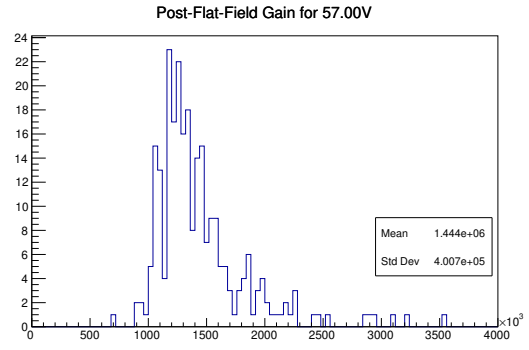


Figure B.20: Distribution of Gain at  $V_{bias} = 55.00$  V after PDE Flat Fielding



**Figure B.21:** Distribution of Gain at  $V_{bias} = 56.00$  V after PDE Flat Fielding



**Figure B.22:** Distribution of Gain at  $V_{bias} = 57.00$  V after PDE Flat Fielding

**B.1.4 PDE after Gain Flat Fielding at given Bias Voltage**

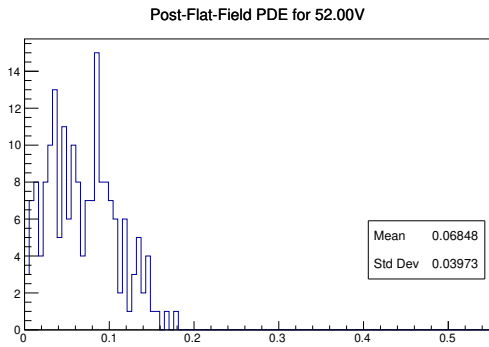


**Figure B.23:** Distribution of PDE at  $V_{bias} = 52.00$  V after Gain Flat Fielding

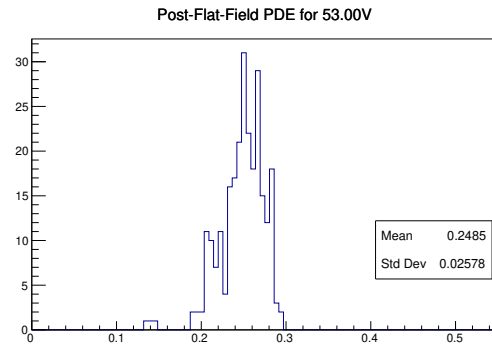


**Figure B.24:** Distribution of PDE at  $V_{bias} = 53.00$  V after Gain Flat Fielding

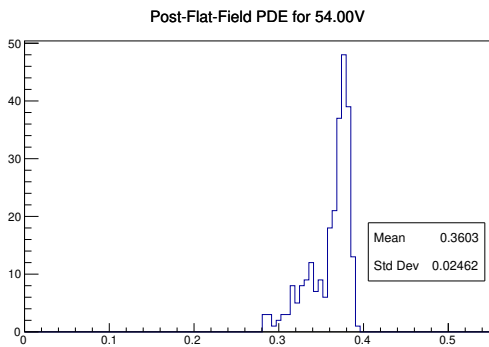


**Figure B.25:** Distribution of PDE at  $V_{bias} = 54.00$  V after Gain Flat Fielding

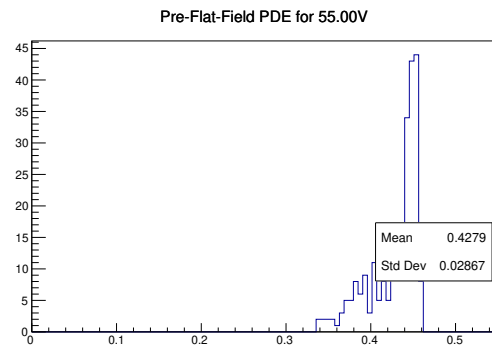


**Figure B.26:** Distribution of PDE at  $V_{bias} = 55.00$  V after Gain Flat Fielding

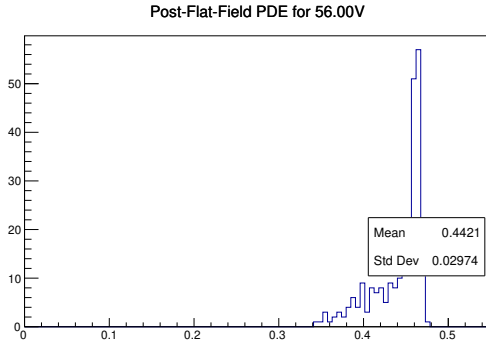


**Figure B.27:** Distribution of PDE at  $V_{bias} = 56.00$  V after Gain Flat Fielding

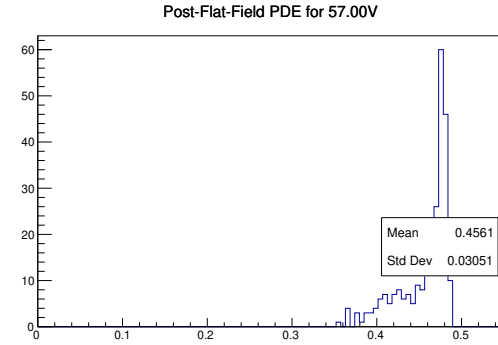


**Figure B.28:** Distribution of PDE at  $V_{bias} = 57.00$  V after Gain Flat Fielding

## B.2 Signal to Noise Ratio measurements

The comparison of signal to noise plots allows for the selection of the biasing voltage and ASIC gain-threshold settings. For the EUSO-SPB1 flight,  $V_{bias} = 55$  V with gain=55 and threshold=243 in the arbitrary units of the Citiroc slow control. We can see that the low

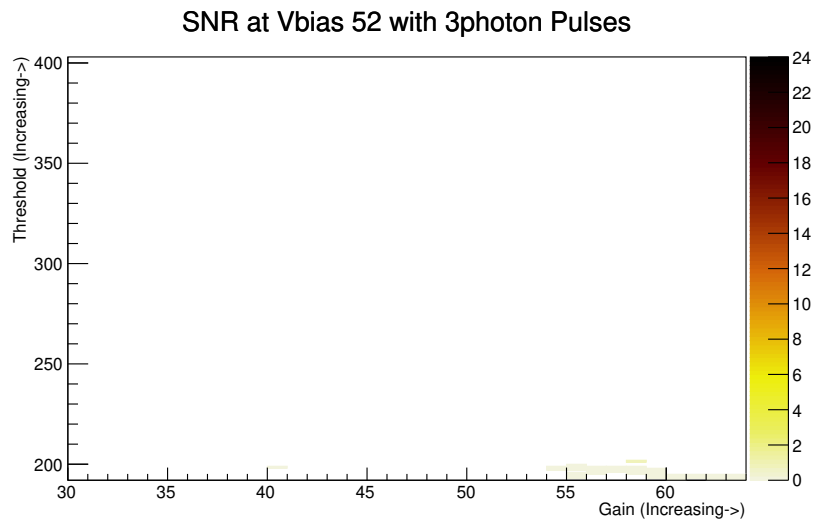


**Figure B.29:** SNR plot for  $V_{bias} = 52$  V

biasing voltage settings does not allow distinguishable difference between the PE peaks even at high ASIC gain. Likewise, at  $V_{bias} = 57$  V, the gain of the sensor and the increased dark count rate leads to the fourth PE peak being seen and smearing of all peaks due to dark counts occurring with a similar rate as incident photons. Thus, a mid voltage must be selected. More careful tuning on  $V_{bias}$  to non-integer values can be undertaken by future studies.

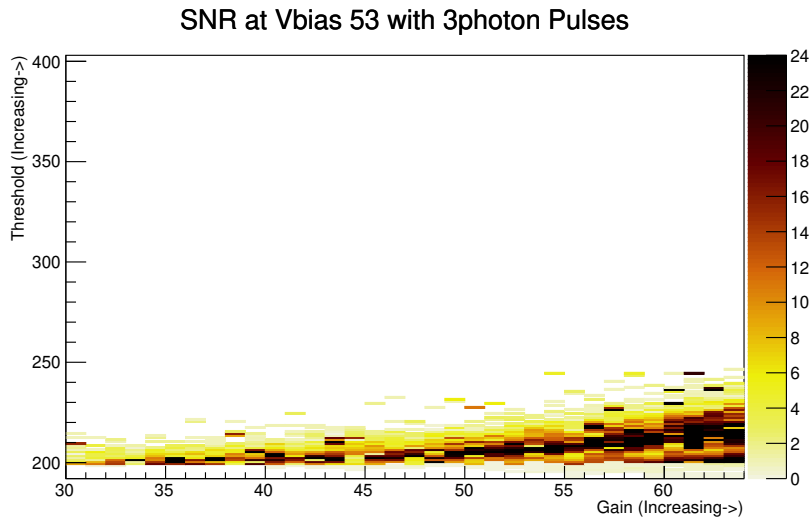


**Figure B.30:** SNR plot for  $V_{bias} = 53$  V

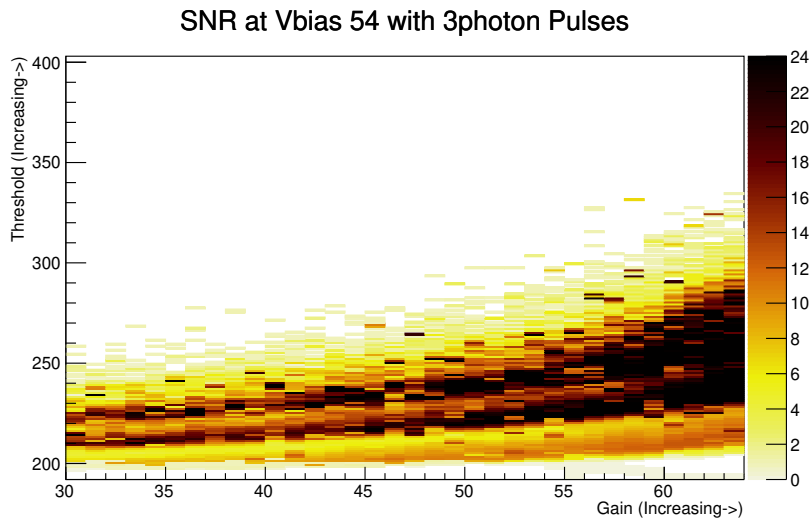


**Figure B.31:** SNR plot for  $V_{bias} = 54$  V

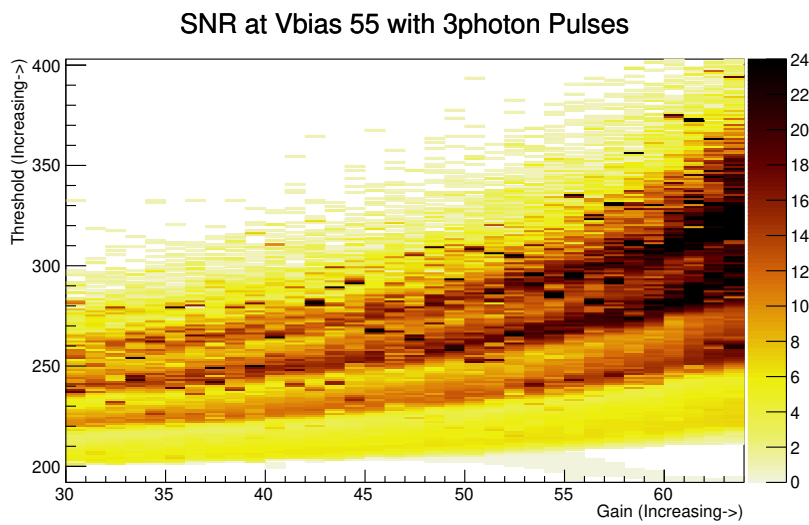


**Figure B.32:** SNR plot for  $V_{bias} = 55$  V

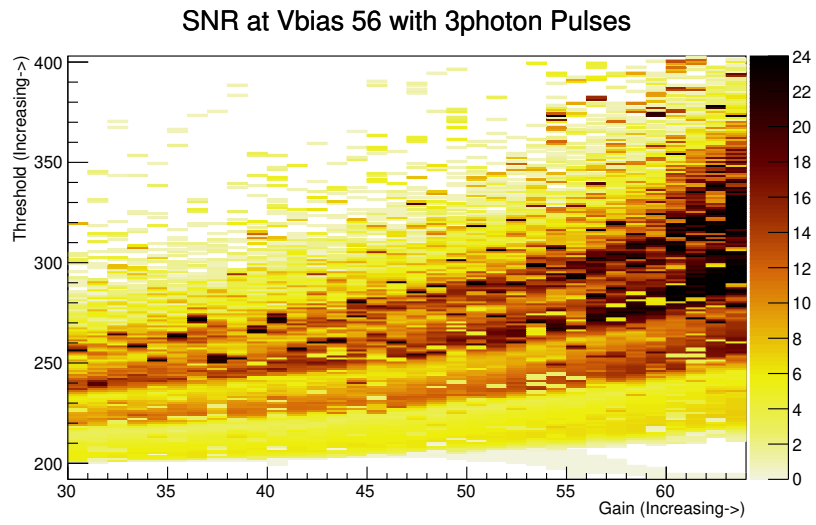


**Figure B.33:** SNR plot for  $V_{bias} = 56$  V

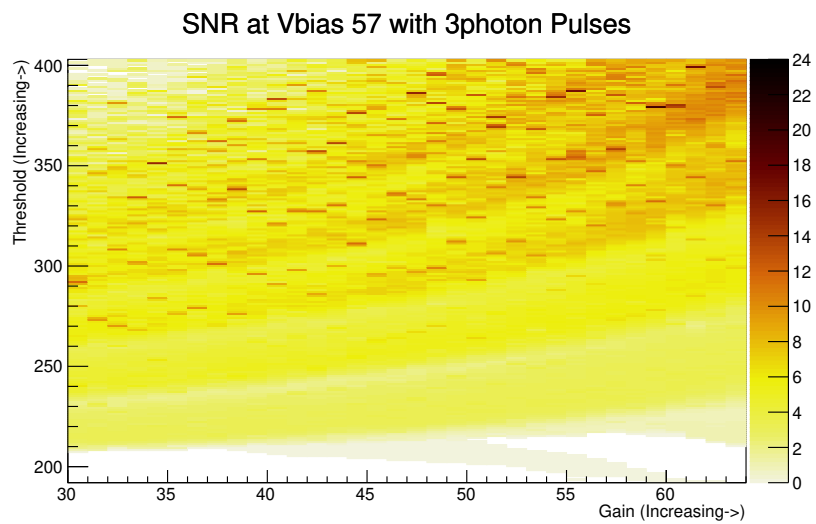


**Figure B.34:** SNR plot for  $V_{bias} = 57$  V

---

---

# APPENDIX C

---

## Appendix C: Operation Manual

### C.1 Single Channel Analysis

The code in this section contains and builds on the work by Max Renschler and Marie Oehler. Their combined python code for analyzing the finger spectra measured in SPOCK are the basis for all the measurements made in the Characterization chapter.

#### C.1.1 `qadc_peakfinding_wp.py`

This code takes a given finger spectrum and fits the Gaussian peaks to each recognizable PE peak. The output is the gain, derived from the separation of each peak from its neighbors, the area of the pedestal (required for determining PDE) and the relevant errors on each. This function is invoked by `process_SiPM_measurement_wp.py` and should likely not be run on single files as it is far more useful in a scan over many bias voltages. This code is adopted from the code used in [7].

#### C.1.2 `process_SiPM_measurement_wp.py`

This is the core operation for analyzing SiPM channels in SPOCK. From the measurements, this program iterates through the channel directory, processes the light power measurements to determine the number of photons emitted, measurement with the light for the gain and measurement with the light source turned off to determine the PDE by the method described in the main text. I invoke this with a script that runs over all the channels used in SiECA called `DirWalk.py` generating an output file `AllArrayCharacteristics.txt` which contains all the necessary parameters for each channel analyzed. This file is then read and processed by `FFC2.cpp` with CERN Root 6.

#### C.1.3 `FFC2.cpp`

From the `AllArrayCharacteristics.txt` file, this script calculates the required bias offsets in the ASICs to generate a flat fielded focal surface either in gain or PDE. Additionally, this script generates plots for the key characteristic parameters both before and after flat fielding. The size of the fixed arrays will have to be changed if you are using more than 256 channels, also, the naming system for filtering channels into each array and sub-array for offset calculation but it should be adaptable for someone with limited C++ experience.

## C.2 SiECA Operation Guide

In the current state, SiECA is semi-autonomous. Within the Pelican case there should be the SiECA camera and a Raspberry Pi, labeled with the user and password. Together, SiECA can be operated in laboratory conditions or if a lens system and external trigger are available, it is ready for field deployment. Testing and repair of the external trigger input is necessary. Please contact Alexander Menshikov at KIT for more information about this interface. Within the Raspberry Pi, there is a *SiECA* directory which contains all the required operations files sub-divided amongst the revisions. In the case latter revisions are developed, they should be placed here. Within a revision directory there are the *Example\_sica* and *libsica\_if* directories. *Example\_sica* is the run directory containing the `main.c` which is compiled into *SiECA\_reader* by running `make` inside the revision directory. Most user parameters are specified in *libsica\_if/siecacommon.h* while operation routines are defined in *Example\_sica/main.c*. The other files in *libsica\_if/* are necessary libraries created by Alexander Menshikov to establish connection, handle signals, handle USB interfaces, etc. To operate SiECA, provide 5 V with a maximum current of 2.5 A and a USB connection from SiECA to the Pi. Additional clocks and trigger lines are optional but the jumper by the LVDS inputs should be open unless these lines are used to prevent open collector noise. With SiECA in a dark environment, it will draw up to 1 A at power on but this will drop to about 0.5 A shortly (10 s) and then decrease to 0.3 to 0.4 A when all initialization from previous settings is complete. Once the current draw has dropped, new commands can be issued. First, it is necessary to revert the USB interface by

```
sudo rmmmod ftdi_sio
```

with the password provided if prompted. Without this, the USB interface will not work.

Once this is done, and *SiECA\_reader* is compiled, it is called simply by

```
./SiECA_reader -f Path/to/Flat/Field/File -o Path/to/Output/File -s
```

The `-s` is for software triggering and is necessary if the trigger is coming via USB rather than the LVDS signal. After issuing this command, the current will increase while generating an event to approximately 0.65 A and then drop back to the 0.4 A range when in between events. If the current again reaches greater than 0.7 A then SiECA is likely caught in a loop, most likely trying to send a partial event and failing packet size checks, and should be power cycled. This happens from time to time. More commonly the packet will be transmitted and accepted but not be complete. Consult the *SiECA2D.py* code for how to automatically check the file size and re-run the measurement if not correct.

## C.3 SiECA with RaspberryPi in SPOCK

Most of the more advanced analysis of SiECA's capabilities have been determined in the SPOCK laboratory with the use of a RaspberryPi as the host computer. This Pi can be connected to remotely allowing the operator to set long measurements to work over the weekend and check on them as necessary without physically accessing the Pi. An external hard drive as data storage point is suggested for all of the following functions as they generate many `.sca` files which can quickly fill the 32 GB SD card in the Pi. If you are accessing SiECA, a Pi should be included in the transport case with the relevant programs already available, simply change the file paths to suit your storage system.

### C.3.1 AxisHelper.py and AxisPrep.py

These two programs setup the 2D translation stage setup in SPOCK for control via python commands. `AxisPrep.py` uses the functions defined in `AxisHelper.py` to determine the

origin and move to where it expects the first (lower right corner looking from the light source at the sensor arrays of SiECA) channel to be scanned. The user can then input movement in mm increments to tune the start location. This must be done before running `SiECA2Dscan.py` or `SiECA2Dscan2.py`.

### C.3.2 `SiECA2Dscan.py` and `SiECA2Dscan2.py`

This code scans over the specified range of bias voltages, gains and thresholds for each channel making a highly detailed mapping of the signal response at each channel. The `SiECA2Dscan2.py` version is a bit faster as it measures all the parameters at each channel before moving to next channel while the original would set the operating parameters and then move through each channel before returning to the first, changing parameters and starting the scan again. By reversing the order and minimizing the number of movements, the process is much faster in `SiECA2Dscan2.py`. No inputs are needed after the light source is properly set on the first channel but one must specify the locations of the lower right channel of each array. In this case, since they are equally spaced, this is a simple calculation at the start of the script but it could be replaced with a user defined list. For the four arrays in SiECA, scanning over a single bias voltage and gain but the range of thresholds from 192 – 402 with each measurement containing 100 events, each file is 3 304 500 B so the total scan contains approximately 54,000 files amounting to nearly 180 GB of data. The python will loop over the scan checking if the corresponding file exists and if so if it is the right size. If this check fails, that measurement is rerun until it succeeds. This can cause an infinite loop if the storage device is full as the file will never be written properly so the loop will never complete. Please use a sufficiently large drive for this scan.

### C.3.3 `SiECAparameterscan.sh`

Similar to the above 2D scans, `SiECAparameterscan.sh` edits the configuration file and recompiles the run code for SiECA before making a measurement with the parameters. In this case, only one channel of SiECA is illuminated so a more broad scan over bias voltages, gains and thresholds is possible without generating too much data. The parameter values are hard coded in the loops so be careful in changing your ranges. Likewise, the sleep commands are necessary to keep the system operating in a stable way. Removing them will likely lead to SiECA getting caught in a transmission loop and hanging. As above, specifying a proper directory for the output files is necessary, specifically one that can handle the large number of files total volume. In the current version, this scan generates 143 GB of data for the specified parameter ranges. It is called without parameters as they are all internally specified.

## C.4 SiECA Data Analysis

### C.4.1 `EventViewerSCA.cpp` and `EventViewerRoot.cpp`

This is a simple viewing program that takes a single SiECA event file (.sca extension binary file), reads it into memory and makes a plot of the total or averaged counts on each channel for the event. It is invoked with:

```
root -l -q EventViewerSCA.cpp "SCAfilename"
```

and the output plot is saved as a PDF in the specified directory. The Root version takes the files from `SiECABinaryReader.cpp` and performs the same plotting. These two are meant to provide a simple introduction to handling .sca files and being able to plot basic results from SiECA data.

### C.4.2 SiECABinaryReader.cpp

This script converts the .sca files from the EUSO-SPB1 mission into CERN Root files for easier navigation. It also reads the telemetry file and combines the information so analysis of the flight and recorded events can be performed. The .sca file structure has changed slightly after the EUSO-SPB1 flight so this reader is not longer appropriate. Calling this program with root is simple:

```
root -l -q SiECABinaryReader.cpp "SCAfilename", "RootFilename"
```

however the *RootFilename* is not needed as it is automatically generated from the event time stamp so this field is ignored but could be implemented if needed later.

### C.4.3 FlightAnalysis.cpp

This program is invoked with Root via:

```
root -l -q FlightAnalysis.cpp
```

It reads the Root files generated by SiECABinaryReader.cpp and performs a cursory analysis looking for charge excess above background, plotting the times SiECA was active during the flight and at what altitude, etc. The output files require a substantial creation of directories that I have not sanitized so it is left to the next user to take this code and improve it or likely rewrite it for the mission you are looking to analyze with this as a rough guide.

### C.4.4 SiECA\_SNR2.cpp

This script calculates the signal to noise ratio for the scans over  $V_{bias}$ , ASIC gain and ASIC threshold generated by SiECAparameterscan.sh. The ratio is described in the main text but amounts to the number of counts on the illuminated channel minus the average number of counts on a non-illuminated channel, divided by the average counts on a non-illuminated channel. This has two effects, the subtraction removes counts due to dark noise and the ratio of the light induced counts on the illuminated channel to the average dark counts on a non illuminated channel provides clear indication of the sensitivity of the parameter setting ( $V_{bias}$ , gain and threshold.)

### C.4.5 SiECA2D.cpp

This program generates all the plots you could ask for from the 2D scan function SiECA2Dscan2.py. Basically, specify the file location and naming if you change it and then this script will create plots showing the uniformity of response for each channel when illuminated, when unilluminated, and when a neighboring channel is illuminated. These plots and the analysis is described in the main text. This script is called with CERN Root, as all the .cpp files are, and does not need any inputs. It will take a while to process through the massive number of files generated in the scan so running in Screen is recommended.

## C.5 Remarks on other scripts

The additional files included on the Pi may be useful but are not as well developed. Most are quick tests that the user can play around with to get an idea what I have done with SiECA. Maybe you think of a better way to test this device or see something useful for another project.

---

---

# CHAPTER 7

---

## Acknowledgments

I would like to thank Professor Bümer and Professor Perić for the opportunity to seek this degree through the development of SiECA. Also, Dr. Haungs for the initial direction and often reminding me that it will work, to persevere and to try just a little more at several points in this work. Immense thanks to Dr. Kleifges for facilitating the cooperation with Alexander Menshikov, the true expert in the development of SiECA and whom the project would have been a total failure without. I owe this degree to the knowledge and hard work of Alexander taking a rough idea and making a fully integrated and functioning machine. My sincerest thanks.

To the community of IKP/IEKP/ETP that have made this adventure feasible, thank you. I doubt anyone could continue to be motivated to work without the camaraderie and sharing of knowledge available within this group. Specifically, Thomas Huber, thank you for saving my thesis before I began and being a constant support throughout both academically and personally. Thank you to Dr. Michael Karus, Marie Oehler, Max Renschler and Andreas Weindl for developing the tools, SPOCK, and the analysis codes to measure SiPM arrays. Without this there would be no chance to develop a camera much less a working one. To Dr. Aswathi Balagopal V. who has probably saved me from legal trouble more times than I should admit and kept me on top of paperwork I was unaware I needed, thank you for finding all the complications I managed to incorrectly avoid. A special thanks to Dr. Daniela Mockler for also working late nights and always having an open door to discuss physics and life in general.

On the more personal side, I need to thank my parents and siblings for being supportive of my international adventure. Always knowing that there is always a home regardless of where I am currently living has provided substantial comfort for my mind. Thank you to the climbing group, dynamic as it is, and to the squash group because physical activity are good for the mind and body. Also, a glass box is excellent for physically expressing frustration against an impervious rubber ball. Thank you to Dr. Darko Verberic for constantly organizing movie nights bringing us together for a couple hours engrossed in film rather than code bugs. Finally, I would like to thank Carolyn Cohen who has always provided emotional support and motivation along with a reason to return to the US when this is done.

If I have neglected anyone on this list, my sincere apologies. It is not that I devalue your contribution to my work and well-being, merely that I am forgetful and under a bit of stress as I write this. Please bring it up next time we meet and I will somehow make it up to you.

Thank you all,  
Will Painter



---

# Bibliography

- [1] P. YU, M. Cardona, *Fundamentals of Semiconductors: Physics and Materials Properties* (Graduate Texts in Physics), Springer, 2010.
- [2] L. Strueder, H. Soltau (INVITED), [High resolution silicon detectors for photons and particles](#), *Radiation Protection Dosimetry* 61 (1-3) (1995) 39–46. doi:10.1093/oxfordjournals.rpd.a082751.  
URL <http://dx.doi.org/10.1093/oxfordjournals.rpd.a082751>
- [3] Hamamatsu, Si-APD, MPPC Handbook, 3rd Edition, 2014.
- [4] A. Nepomuk Otte, T. Nguyen, J. Stansbury, Locating the avalanche structure and the origin of breakdown generating charge carriers in silicon photomultipliers by using the bias dependent breakdown probability (2018)[arXiv:1808.00487](#).
- [5] H. P. K.K., MPPCs for precision measurement, cat. No. KAPD1052E04 Aug. 2016 DN.
- [6] H. P. K.K., TSV MPPC array Low Cross Talk type: S13361-3050NE-08, S13361-3050NS-08 S13361-3050AE-08, S13361-3050AS-08, form ksx-0046 c Edition, 2015.05 KSX-I50081-E S13361-3050xx-08.
- [7] M. Renschler, W. Painter, F. Bisconti, A. Haungs, T. Huber, M. Karus, H. Schieler, A. Weindl, Characterization of Hamamatsu 64-channel TSV SiPMs, *Nucl. Instrum. Meth. A* 888 (2018) 257–267. [arXiv:1804.00897](#), doi:10.1016/j.nima.2018.01.029.
- [8] H. P. K.K., [Photomultiplier Tubes and Assemblies for Scintillation counting and High Energy Physics](#) (2017).  
URL [https://www.hamamatsu.com/resources/pdf/etd/High\\_energy\\_PMT\\_TPMZ0003E.pdf](https://www.hamamatsu.com/resources/pdf/etd/High_energy_PMT_TPMZ0003E.pdf)
- [9] F. Bisconti, JEM-EUSO, EUSO-TA fluorescence detector, in: 25th European Cosmic Ray Symposium (ECRS 2016) Turin, Italy, September 04-09, 2016, 2017. [arXiv:1701.07091](#).
- [10] E. Iwotschkin, private communication (February 2019).
- [11] T. Huber, Silicon photomultiplier for the space-based fluorescence telescope jem-euso (2016).
- [12] J. R. Hörandel, Early Cosmic-Ray Work Published in German (2012)[AIP Conf. Proc.1516,52(2012)]. [arXiv:1212.0706](#), doi:10.1063/1.4792540.

- [13] T. Wulf, A new electrometer for static charges, *Physikalische Zeitschrift* (1909) 251.
- [14] T. Wulf, *Physikalische Zeitschrift* (1909) 253.
- [15] T. Wulf, On the origin of the gamma radiation in the atmosphere, *Physikalische Zeitschrift* (1909) 997.
- [16] T. Wulf, Observation on the radioation of high penetration power on the eiffel tower, *Physikalische Zeitschrift* (1910) 811.
- [17] V. Hess, On the observation of the penetrating radiation in seven free balloon campaigns, *Physikalische Zeitschrift* (1912) 1084.
- [18] W. Kolhöster, Measurments of the penetrating radiation in a free balloon at high altitudes, *Physikalische Zeitschrift* (1913) 1153.
- [19] H. Geiger, W. Müller, [Elektronenzählrohr zur messung schwächster aktivitäten](#), *Naturwissenschaften* (1928) 617.  
URL <https://doi.org/10.1007/BF01494093>
- [20] W. Bothe, W. Kolhöster, The nature of high-altitude radiation, *Zeitschrift für Physik* (1929) 751.
- [21] H. Bethe, Theory of the Passage of Fast Corpuscular Rays Through Matter, *Annalen Phys.* 5 (1930) 325–400, [*Annalen Phys.*397,325(1930)]. [doi:10.1002/andp.19303970303](https://doi.org/10.1002/andp.19303970303).
- [22] F. Bloch, Zur Bremsung Rasch Bewegter Teilchen beim Durchgang durch Materie, *Annalen Phys.* 408 (1933) 285–320. [doi:10.1002/andp.19334080303](https://doi.org/10.1002/andp.19334080303).
- [23] P. M. S. Blackett, G. P. S. Occhialini, Some Photographs of the Tracks of Penetrating Radiation, *Proc. Roy. Soc. Lond.* A139 (839) (1933) 699–720.
- [24] H. Bethe, W. Heitler, On the Stopping of fast particles and on the creation of positive electrons, *Proc. Roy. Soc. Lond.* A146 (1934) 83–112. [doi:10.1098/rspa.1934.0140](https://doi.org/10.1098/rspa.1934.0140).
- [25] G. Pfozter, Three-fold coincidences of the ultra rays from vertical direction in the stratosphere, *Physikalische Zeitschrift* (1936) 23.
- [26] M. BLAU, H. WAMBACHER, [Disintegration processes by cosmic rays with the simultaneous emission of several heavy particles](#), *Nature* 140 (1937) 585 EP –.  
URL <https://doi.org/10.1038/140585a0>
- [27] W. Kolhöster, Coupled high-altitude rays, *Naturwissenschaften* (1938) 576.
- [28] P. Auger, R. Maze, T. Grivet-Mayer, Grandes gerbes cosmiques atmosphériques contenant des corpuscules ultrapénétrants, *Compt. Rend. Hebd. Seances Acad. Sci.* 206 (23) (1938) 1721–1723.
- [29] P. Auger, R. Maze, Les grandes gerbes cosmiques de l’atmosphère, *Compt. Rend. Hebd. Seances Acad. Sci.* 207 (3) (1938) 228–230.
- [30] P. Auger, P. Ehrenfest, R. Maze, J. Daudin, A. F. Robley, Extensive cosmic ray showers, *Rev. Mod. Phys.* 11 (1939) 288–291. [doi:10.1103/RevModPhys.11.288](https://doi.org/10.1103/RevModPhys.11.288).
- [31] C. M. G. LATTES, G. P. S. OCCHIALINI, C. F. POWELL, [Observations on the tracks of slow mesons in photographic emulsions\\*](#), *Nature* 160 (1947) 453 EP –, article.  
URL <https://doi.org/10.1038/160453a0>

- [32] U. Becker, Alpha Magnetic Spectrometer, AMS-01: First flight, first results. Future AMS-02, AIP Conf. Proc. 516 (1) (2000) 335. doi:10.1063/1.1291488.
- [33] A. Kounine, AMS, AMS Results on the Properties of the Fluxes of Elementary Particles and Nuclei in Primary Cosmic Rays, in: The Fluorescence detector Array of Single-pixel Telescopes: Contributions to the 35th International Cosmic Ray Conference (ICRC 2017), Vol. ICRC2017, 2018, p. 1093. doi:10.22323/1.301.1093.
- [34] A. G. Mariuzzi, Pierre Auger, Ultrahigh-energy cosmic rays, 2018. arXiv:1812.06618.
- [35] A. A. Watson, The highest energy cosmic rays: the past, the present and the future, in: Ultra High Energy Cosmic Rays (UHECR 2018) Paris, France, October 8-12, 2018, 2019. arXiv:1901.06676.
- [36] M. e. Tanabashi, Particle Data Group, Review of particle physics, Phys. Rev. D 98 (2018) 030001. doi:10.1103/PhysRevD.98.030001.  
URL <https://link.aps.org/doi/10.1103/PhysRevD.98.030001>
- [37] R. Engel, D. Heck, T. Pierog, Extensive air showers and hadronic interactions at high energy, Annual Review of Nuclear and Particle Science 61 (1) (2011) 467–489. doi:10.1146/annurev.nucl.012809.104544.  
URL <https://doi.org/10.1146/annurev.nucl.012809.104544>
- [38] W. D. Apel, et al., KASCADE Grande, Kneelike structure in the spectrum of the heavy component of cosmic rays observed with KASCADE-Grande, Phys. Rev. Lett. 107 (2011) 171104. arXiv:1107.5885, doi:10.1103/PhysRevLett.107.171104.
- [39] G. Cataldi, Pierre Auger, AugerPrime: the upgrade program of the Pierre Auger Observatory., PoS EPS-HEP2017 (2017) 005. doi:10.22323/1.314.0005.
- [40] A. Haungs, H. Rebel, M. Roth, Energy spectrum and mass composition of high-energy cosmic rays, Reports on Progress in Physics 66 (7) (2003) 1145–1206. doi:10.1088/0034-4885/66/7/202.  
URL <https://doi.org/10.1088/0034-4885/66/7/202>
- [41] M. Karus, Development of a calibration stand for photosensors for extremely high-energy cosmic ray research, Ph.D. thesis, Karlsruhe Institut für Technologie (KIT), 51.03.04; LK 01 (2016). doi:10.5445/IR/1000054408.
- [42] T. K. Gaisser, A. M. Hillas, Reliability of the method of constant intensity cuts for reconstructing the average development of vertical showers, in: Proc. of 15th Int. Cosmic Ray Conf., 13–26 Aug 1977, p. 353.
- [43] P. A. Čerenkov, Visible radiation produced by electrons moving in a medium with velocities exceeding that of light, Phys. Rev. 52 (1937) 378–379. doi:10.1103/PhysRev.52.378.  
URL <https://link.aps.org/doi/10.1103/PhysRev.52.378>
- [44] M. Ave, et al., Spectrally resolved pressure dependence measurements of air fluorescence emission with airfly, Nuclear Instruments and Methods in Physics Research Section A: Accelerators, Spectrometers, Detectors and Associated Equipment 597 (1) (2008) 41 – 45, proceedings of the 5th Fluorescence Workshop. doi:https://doi.org/10.1016/j.nima.2008.08.052.  
URL <http://www.sciencedirect.com/science/article/pii/S016890020801276X>

- [45] J. Allen, et al., The Pierre Auger Observatory offline software, J. Phys. Conf. Ser. 119 (2008) 032002. doi:10.1088/1742-6596/119/3/032002.
- [46] A. M. Hillas, The Origin of Ultrahigh-Energy Cosmic Rays, Ann. Rev. Astron. Astrophys. 22 (1984) 425–444. doi:10.1146/annurev.aa.22.090184.002233.
- [47] J. W. Cronin, The Highest - energy cosmic rays, Nucl. Phys. Proc. Suppl. 138 (2005) 465–491, [465(2004)]. arXiv:astro-ph/0402487, doi:10.1016/j.nuclphysbps.2004.11.107.
- [48] G. T. Zatsepin, V. A. Kuzmin, Upper limit of the spectrum of cosmic rays, JETP Lett. 4 (1966) 78–80, [Pisma Zh. Eksp. Teor. Fiz.4,114(1966)].
- [49] Abbasi, R. U. *et al.*, High Resolution Fly’s Eye Collaboration, [First Observation of the Greisen-Zatsepin-Kuzmin Suppression](#), Phys. Rev. Lett. 100 (2008) 101101. doi:10.1103/PhysRevLett.100.101101.  
URL <http://link.aps.org/doi/10.1103/PhysRevLett.100.101101>
- [50] V. S. Berezhinsky, G. T. Zatsepin, Cosmic rays at ultrahigh-energies (neutrino?), Phys. Lett. 28B (1969) 423–424. doi:10.1016/0370-2693(69)90341-4.
- [51] S. Razzaque, P. Meszaros, E. Waxman, Detecting gamma-ray bursts with ultrahigh energy neutrinos, Int. J. Mod. Phys. A20 (2005) 3099–3101. doi:10.1142/S0217751X0502584X.
- [52] J. H. Adams, Jr., et al., JEM-EUSO, The JEM-EUSO Mission: Contributions to the ICRC 2013, 2013. arXiv:1307.7071.
- [53] A. V. Olinto, et al., POEMMA: Probe Of Extreme Multi-Messenger Astrophysics, PoS ICRC2017 (2018) 542, [35,542(2017)]. arXiv:1708.07599, doi:10.22323/1.301.0542.
- [54] J. Adams, others for the JEM-EUSO Collaboration, [An evaluation of the exposure in nadir observation of the jem-euso mission](#), Astroparticle Physics 44 (2013) 76 – 90. doi: <https://doi.org/10.1016/j.astropartphys.2013.01.008>.  
URL <http://www.sciencedirect.com/science/article/pii/S0927650513000182>
- [55] M. Casolino, et al., JEM-EUSO Colaboration, The JEM-EUSO instrument, Exper. Astron. 40 (1) (2015) 19–44. doi:10.1007/s10686-014-9418-x.
- [56] J. Eser, The euso-spb1 project and laser test beams for space-based optical cosmic ray detectors (2018).
- [57] L. Wiencke, A. Olinto, JEM-EUSO, EUSO-SPB1 Mission and Science, PoS ICRC2017 (2018) 1097. doi:10.22323/1.301.1097.
- [58] M. Cerruti, A. Zech, C. Boisson, G. Emery, S. Inoue, J. P. Lenain, Gammas and neutrinos from TXS 0506+056, in: Week of French Astrophysics : Semaine de l’Astrophysique Francaise (SF2A 2018) Bordeaux, France, July 3-6, 2018, 2018. arXiv:1810.08825.
- [59] K. J. Kelly, P. A. N. Machado, Multimessenger Astronomy and New Neutrino Physics, JCAP 1810 (10) (2018) 048. arXiv:1808.02889, doi:10.1088/1475-7516/2018/10/048.
- [60] C. Guépin, F. Sarazin, J. Krizmanic, J. Loerincs, A. Olinto, A. Piccone, Geometrical Constraints of Observing Very High Energy Earth-Skimming Neutrinos from Space (2018)arXiv:1812.07596.

- [61] A. Bertone, Caratterizzazione e installazione di filtri ottici per la SiPM camera del progetto EUSO-SPB (2016).
- [62] J. Bayer, M. E. Bertaina, F. Fenu, M. Mignone, H. Miyamoto, K. Shinozaki, A. Cummings, J. B. Eser, A. Jung, JEM-EUSO, The trigger logic of EUSO-SPB and its performance, PoS ICRC2017 (2018) 443. [doi:10.22323/1.301.0443](https://doi.org/10.22323/1.301.0443).
- [63] S. Ahmad, et al., JEM-EUSO, SPACIROC: A Front-End Readout ASIC for Spatial Cosmic Ray Observatory., in: Proceedings, 32nd International Cosmic Ray Conference (ICRC 2011): Beijing, China, August 11-18, 2011, Vol. 3, p. 56. [doi:10.7529/ICRC2011/V03/0236](https://doi.org/10.7529/ICRC2011/V03/0236).
- [64] H. P. K.K., Driver circuit for MPPC: C12332-01, cat. No. KACC1233E02 Sep. 2016 DN.
- [65] P. Eckert, H.-C. Schultz-Coulon, W. Shen, R. Stamen, A. Tadday, Characterisation Studies of Silicon Photomultipliers, Nucl. Instrum. Meth. A620 (2010) 217–226. [arXiv:1003.6071](https://arxiv.org/abs/1003.6071), [doi:10.1016/j.nima.2010.03.169](https://doi.org/10.1016/j.nima.2010.03.169).
- [66] Schott, Datenblatt BG3, weitere Erklärungen siehe Katalog 'Optical Filters 2013' (12 2014).
- [67] Epoxy Technology, EPO-TEK 301-2 Technical Data Sheet, rev. XII (4 2015).
- [68] J.-B. Cizel, Datasheet Citiroc1A, Weeroc (2 2018).
- [69] S. Ritt, *9 Channel, 5 GSPS Switched Capacitor Array DRS4* (2009).  
URL [https://www.psi.ch/drs/DocumentationEN/DRS4\\_rev09.pdf](https://www.psi.ch/drs/DocumentationEN/DRS4_rev09.pdf)
- [70] A. N. Otte, D. Garcia, T. Nguyen, D. Purushotham, Characterization of three high efficiency and blue sensitive silicon photomultipliers, Nuclear Instruments and Methods in Physics Research Section A: Accelerators, Spectrometers, Detectors and Associated Equipment 846 (2017) 106 – 125. [doi:https://doi.org/10.1016/j.nima.2016.09.053](https://doi.org/10.1016/j.nima.2016.09.053).



---

# Erklärung

Karlsruhe, den 17.05.2019

## **Erklärung der selbständigen Anfertigung meiner Dissertationsschrift**

Hiermit versichere ich, dass ich die Dissertationsschrift mit dem Titel

**Development of SiPM camera for detection and measurement of fluorescence emission  
from extensive air-showers generated by ultra high energy cosmic rays**

selbständig und ohne unerlaubte fremde Hilfe verfasst habe. Dabei habe ich keine anderen,  
als die von mir angegebenen Hilfsmittel benutzt.

---

Your Name